
Theses and Dissertations

Summer 2012

Pointwise identification for thin shell structures and verification using realistic cerebral aneurysms

Shouhua Hu
University of Iowa

Copyright 2012 Shouhua Hu

This dissertation is available at Iowa Research Online: <http://ir.uiowa.edu/etd/3313>

Recommended Citation

Hu, Shouhua. "Pointwise identification for thin shell structures and verification using realistic cerebral aneurysms." PhD (Doctor of Philosophy) thesis, University of Iowa, 2012.
<http://ir.uiowa.edu/etd/3313>.

Follow this and additional works at: <http://ir.uiowa.edu/etd>



Part of the [Mechanical Engineering Commons](#)

POINTWISE IDENTIFICATION FOR THIN SHELL STRUCTURES AND
VERIFICATION USING REALISTIC CEREBRAL ANEURYSMS

by

Shouhua Hu

An Abstract

Of a thesis submitted in partial fulfillment of the
requirements for the Doctor of Philosophy
degree in Mechanical Engineering
in the Graduate College of
The University of Iowa

July 2012

Thesis Supervisor: Associate Professor Jia Lu

ABSTRACT

Identification of material properties for elastic materials is important in mechanics, material sciences, mechanical engineering and biomedical engineering. Although the principle and techniques have been long established, the application in living biology still faces challenges. The biological materials are in general nonlinear, anisotropic, heterogeneous, and subject-specific. The difficulty is compounded sometimes by the requirement of non-destructiveness in medical applications. Recently, the pointwise identification method (PWIM) was proposed to address some of the needs of soft tissue characterization. PWIM is a non-invasive identification method, designed for thin materials; it can sharply characterize arbitrary heterogeneous property distributions.

The primary goal of this thesis is to extend the pointwise identification method, originally developed for membranes which by default is of convex shape in pressurized states, to thin structures of arbitrary geometry. This work consists of four parts. The first part investigates the insensitivity of stress solution to material parameters in thin shell structures. This is an important first step, because PWIM hinges on the static determinacy property of the equilibrium problem of membranes. Before introducing the shell element into PWIM, it is necessary to test to what extent the assumption of static determinacy remains reasonable. It is shown that saccular structure which bending stress is small compared to in-plane stress, can still be treated as a statically determined structure.

The second part focuses on developing finite element formulations of forward

and inverse shell methods for a hyperelastic material model specifically proposed for cerebral aneurysms tissues. This is a preparatory step for the core development.

The third part is the development of pointwise identification method for thin shell structures. Methods for stress solution, strain acquisition, and parameter regression will be discussed in detail. The entire process is demonstrated using an example of a geometrically realistic model of aneurysm.

The fourth part is testing the applicability on geometrically realistic cerebral aneurysms. Six models were selected in the study; the emphasis is placed on cerebral aneurysm with concave or saddle surface region for which the use of shell theory is a must. The identification results of all six human cerebral aneurysms successfully demonstrate that the shell PWIM can be applied to realistic cerebral aneurysms. Four types of heterogeneous property distributions are considered in the study. It is found that the method can accurately back out the property distributions in all cases. Fiber directions can also be accurately estimated. The robustness of the method at the presence of numerical noise is also investigated. It is shown that the shell PWIM still works when small perturbations exist in displacements.

Abstract Approved: _____

Thesis Supervisor

Title and Department

Date

POINTWISE IDENTIFICATION FOR THIN SHELL STRUCTURES AND
VERIFICATION USING REALISTIC CEREBRAL ANEURYSMS

by

Shouhua Hu

A thesis submitted in partial fulfillment of the
requirements for the Doctor of Philosophy
degree in Mechanical Engineering
in the Graduate College of
The University of Iowa

July 2012

Thesis Supervisor: Associate Professor Jia Lu

Graduate College
The University of Iowa
Iowa City, Iowa

CERTIFICATE OF APPROVAL

PH.D. THESIS

This is to certify that the Ph.D. thesis of

Shouhua Hu

has been approved by the Examining Committee for the
thesis requirement for the Doctor of Philosophy degree
in Mechanical Engineering at the July 2012 graduation.

Thesis committee: _____
Jia Lu, Thesis Supervisor

Kyung K. Choi

Ching-Long Lin

Madhavan L. Raghavan

Shaoping Xiao

ACKNOWLEDGEMENTS

First and foremost I want to express my sincere gratitude to my advisor Professor Jia Lu. It has been a great honor to be his Ph.D. student. His tremendous guidance and wise advice have been of great value for me in all the time of graduate studies.

I am especially thankful to Professor Madhavan L. Raghavan for providing not only some important data during this research but also many valuable suggestions. I also thank Professor Kyung K. Choi, Professor Ching-Long Lin, Professor Shaoping Xiao for serving in my thesis committee and giving many valuable suggestions.

I would like to acknowledge Aki Laakso in Department of Neurosurgery, Helsinki University Central Hospital, Helsinki, Finland, and Dr. Manasi Ramachandran in Professor Madhavan L. Raghavan's lab, for their data acquisition and 3D model segmentation work for the data used in this research.

I also would like to thank the former and current colleague in Professor Lu's group, especially Dr. Xuefeng Zhao, Dr. Xianlian Zhou, Dr. Jing Qian and Mr. Chao Zheng for their friendship and many generous helps.

This research is partially supported by the NIH grant #HL083475. This support is greatly appreciated.

ABSTRACT

Identification of material properties for elastic materials is important in mechanics, material sciences, mechanical engineering and biomedical engineering. Although the principle and techniques have been long established, the application in living biology still faces challenges. The biological materials are in general nonlinear, anisotropic, heterogeneous, and subject-specific. The difficulty is compounded sometimes by the requirement of non-destructiveness in medical applications. Recently, the pointwise identification method (PWIM) was proposed to address some of the needs of soft tissue characterization. PWIM is a non-invasive identification method, designed for thin materials; it can sharply characterize arbitrary heterogeneous property distributions.

The primary goal of this thesis is to extend the pointwise identification method, originally developed for membranes which by default is of convex shape in pressurized states, to thin structures of arbitrary geometry. This work consists of four parts. The first part investigates the insensitivity of stress solution to material parameters in thin shell structures. This is an important first step, because PWIM hinges on the static determinacy property of the equilibrium problem of membranes. Before introducing the shell element into PWIM, it is necessary to test to what extent the assumption of static determinacy remains reasonable. It is shown that saccular structure which bending stress is small compared to in-plane stress, can still be treated as a statically determined structure.

The second part focuses on developing finite element formulations of forward and inverse shell methods for a hyperelastic material model specifically proposed for cerebral aneurysms tissues. This is a preparatory step for the core development.

The third part is the development of pointwise identification method for thin shell structures. Methods for stress solution, strain acquisition, and parameter regression will be discussed in detail. The entire process is demonstrated using an example of a geometrically realistic model of aneurysm.

The fourth part is testing the applicability on geometrically realistic cerebral aneurysms. Six models were selected in the study; the emphasis is placed on cerebral aneurysm with concave or saddle surface region for which the use of shell theory is a must. The identification results of all six human cerebral aneurysms successfully demonstrate that the shell PWIM can be applied to realistic cerebral aneurysms. Four types of heterogeneous property distributions are considered in the study. It is found that the method can accurately back out the property distributions in all cases. Fiber directions can also be accurately estimated. The robustness of the method at the presence of numerical noise is also investigated. It is shown that the shell PWIM still works when small perturbations exist in displacements.

TABLE OF CONTENTS

LIST OF TABLES	viii
LIST OF FIGURES	ix
CHAPTER	
1 INTRODUCTION	1
1.1 Motivation	1
1.2 Literature review	2
1.2.1 Regression-based methods	2
1.2.2 Optimization-based methods	4
1.2.3 Inverse studies in cerebral aneurysms	6
1.2.4 Pointwise Identification Method	7
1.3 Objectives	9
1.4 Organization	10
2 THEORETICAL BACKGROUND	12
2.1 Membrane theory	12
2.1.1 Kinematics	12
2.1.2 Kinetics	15
2.1.3 Constitutive relations	16
2.2 Shell theory	19
2.2.1 Kinematics	19
2.2.2 Balance laws	21
2.3 Inverse elastostatic method	25
2.3.1 Inverse shell formulations	27
2.4 Pointwise identification method (PWIM)	28
2.4.1 Stress acquisition	29
2.4.2 Stain acquisition and computation	30
2.4.3 Parameter identification	30
3 SENSITIVITY OF STRESS TO MATERIAL MODEL IN INVERSE & FORWARD ANALYSIS OF THIN STRUCTURES	32
3.1 Tubular geometry - AAA	32
3.1.1 FEA models shell	33
3.1.2 Material model	33
3.1.3 Results	34

3.1.3.1	Juvenile AAA	34
3.1.3.2	Full grown AAA	42
3.1.4	Bending effects on material sensitivity	49
3.2	Saccular geometries - 26 human cerebral aneurysms	56
3.2.1	Stress results	57
3.2.2	Stress sensitivity study	58
3.3	Discussion	64
3.3.1	Stress insensitivity study	64
3.3.2	Implications of inverse analysis for AAA	73
4	IMPLEMENTATION OF A CEREBRAL ANEURYSM TISSUE MODEL IN FORWARD AND INVERSE SHELL ELEMENT	76
4.1	Holzapfel model	76
4.2	Constitutive equations	78
4.2.1	Forward stress function	78
4.2.2	Inverse stress function	80
4.3	Validation	81
4.3.1	Forward-inverse loop	81
4.3.1.1	Example: pressurized hemisphere	82
4.3.1.2	Example: bending plate	84
4.3.2	Stress solution	85
5	POINTWISE IDENTIFICATION METHOD FOR SHELL STRUC- TURES	86
5.1	Pointwise identification method for shell structure	86
5.2	Demonstration of the method using an aneurysm model	88
5.2.1	Material heterogeneity	89
5.2.2	Strain field	90
5.2.3	Stress field	93
5.2.4	Constitutive regression	95
5.2.5	Stress insensitivity of inverse stress	97
5.2.6	Distribution of the identified parameters	99
5.2.7	Forward predictability validation	101
5.3	Discussion	102
6	APPLICABILITY OF PWIM IN CEREBRAL ANEURYSMS	104
6.1	The applicability study	104
6.1.1	Method	104
6.1.2	Pointwise identification results	106
6.2	Unknown fiber direction	112
6.2.1	Identification results	112

6.2.2	Predictability of the identified parameters	115
6.3	Influence of noise in motion data	115
6.3.1	Method	121
6.3.2	Identification results	122
6.3.3	Predictability of the identified parameters	125
6.4	Discussion	127
7	CONCLUSIONS	130
7.1	Summary	130
7.2	Outlook	132
	REFERENCES	134

LIST OF TABLES

Table	
3.1	Maximum stress and mean stress of four material models. 41
3.2	Percentage differences of maximum stress and mean stress relative to reference material model using the forward and inverse methods. 42
3.3	Statistics of the percentage differences (%) by using forward and inverse method, respectively. 42
3.4	Maximum stress and mean stress of four material models. 48
3.5	Percentage differences of maximum stress and mean stress relative to reference material model using the forward and inverse methods. 48
3.6	Statistics of the percentage differences (%) by using forward and inverse method, respectively. 49
3.7	Statistics of the percentage differences (%) in the juvenile AAA by using forward and inverse method, respectively. 52
3.8	Statistics of the percentage differences (%) in the full grown AAA by using forward and inverse method, respectively. 52
4.1	Nodal coordinate in initial configuration \mathcal{R} and stress-free configuration \mathcal{R}' predicted by inverse method. 83
5.1	Convected and non-convected base vectors in three configurations. 94
5.2	Maximum, minimum and mean errors of the identified parameters in the identification region. 101
6.1	Statistics of the identification errors (%) of five cases. 112

LIST OF FIGURES

Figure	
2.1	Schematic illustration of the kinematic map. 13
2.2	Illustration of shell deformation. 20
2.3	Basic procedure of PWIM. 29
3.1	Deformed shape (mesh) vs. <i>in vivo</i> shape (shaded) using conventional forward shell method: (a) Fung's model with baseline material parameters; (b) neo-Hookean model with baseline material parameters. 35
3.2	Initial (Stress free) shape (mesh) vs. <i>in vivo</i> shape (shaded) using inverse shell method: (a) Fung's model with baseline material parameters; (b) neo-Hookean model with baseline material parameters. 36
3.3	Comparison of von Mises stress predicted using the Fung family. First row: forward method. (a) Baseline; (b) Stiffer; (c) Percentage differences. Second row: inverse method. (d) Baseline; (e) Stiffer; (f) Percentage differences. 37
3.4	Comparison of von Mises stress predicted using the neo-Hookean family. First row: forward method. (a) Baseline; (b) Stiffer; (c) Percentage differences. Second row: inverse method. (d) Baseline; (e) Stiffer; (f) Percentage differences. 38
3.5	Percentage stress differences between the baseline Fung model and the baseline neo-Hookean model by using forward and inverse method, respectively: (a) forward method; (b) inverse method. 41
3.6	Deformed shape (mesh) vs. <i>in vivo</i> shape (shaded) using forward shell method: (a) Fung's model with baseline material parameters; (b) neo-Hookean model with baseline material parameters. 43
3.7	Initial (Stress free) shape (mesh) vs. <i>in vivo</i> shape (shaded) using inverse shell method: (a) Fung's model with baseline material parameters; (b) neo-Hookean model with baseline material parameters. 44

3.8	Von Mises stress results using the Fung models. First row: forward method. (a) Baseline; (b) Stiffer; (c) Percentage difference. Second row: forward method. (d) Baseline; (e) Stiffer; (f) Percentage difference. . . .	45
3.9	Von Mises stress results using the neo-Hookean models. First row: forward method. (a) Baseline; (b) Stiffer; (c) Percentage difference. Second row: forward method. (d) Baseline; (e) Stiffer; (f) Percentage difference. . . .	46
3.10	Percentage stress differences between the baseline Fung model and the baseline neo-Hookean model by using forward and inverse method respectively: (a) forward method; (b) inverse method.	47
3.11	Bending factor distribution of the baseline Fung model: (a) juvenile AAA model; (b) full grown AAA model.	50
3.12	Percentage stress differences between of the juvenile AAA by using forward and inverse method respectively: (a) & (b) stress differences between baseline Fung with stiffer Fung material model; (c) & (d) stress differences between baseline neo-Hookean with stiffer neo-Hookean material model; (e) & (f) stress differences between baseline Fung model with baseline neo-Hookean model.	51
3.13	Percentage stress differences between of the full grown AAA by using forward and inverse method respectively: (a) & (b) stress differences between baseline Fung with stiffer Fung material model; (c) & (d) stress differences between baseline neo-Hookean with stiffer neo-Hookean material model; (e) & (f) stress differences between baseline Fung model with baseline neo-Hookean model.	53
3.14	Bending factor-von Mises stress differences in the juvenile AAA using inverse method: (a) Fung material model; (b) neo-Hookean material model.	54
3.15	Bending factor-von Mises stress differences in the Full grown AAA using inverse method: (a) Fung material model; (b) neo-Hookean material model.	55
3.16	“Edge” points locations: (a) juvenile AAA; (b) full grown AAA.	56
3.17	First principal stress distributions, part <i>I</i> . Upper row: the stress result computed by forward method; lower row: the stress result computed by inverse method.	59

3.18	First principal stress distributions, part <i>II</i> . Upper row: the stress result computed by forward method; lower row: the stress result computed by inverse method.	60
3.19	First principal stress distributions, part <i>III</i> . Upper row: the stress result computed by forward method; lower row: the stress result computed by inverse method.	61
3.20	First principal stress distributions, part <i>IV</i> . Upper row: the stress result computed by forward method; lower row: the stress result computed by inverse method.	62
3.21	First principal stress distributions, part <i>V</i> . Upper row: the stress result computed by forward method; lower row: the stress result computed by inverse method.	63
3.22	The comparison of 95% of the maximum first principal stress between forward and inverse method, respectively.	63
3.23	First principal stress differences by using forward and inverse method, respectively, part <i>I</i> . Upper row: the stress result computed by forward method; lower row: the stress result computed by inverse method. . . .	65
3.24	First principal stress differences by using forward and inverse method, respectively, part <i>II</i> . Upper row: the stress result computed by forward method; lower row: the stress result computed by inverse method. . . .	66
3.25	First principal stress differences by using forward and inverse method, respectively, part <i>III</i> . Upper row: the stress result computed by forward method; lower row: the stress result computed by inverse method. . . .	67
3.26	First principal stress differences by using forward and inverse method, respectively, part <i>IV</i> . Upper row: the stress result computed by forward method; lower row: the stress result computed by inverse method. . . .	68
3.27	First principal stress differences by using forward and inverse method, respectively, part <i>V</i> . Upper row: the stress result computed by forward method; lower row: the stress result computed by inverse method. . . .	69
3.28	Stress sensitivity in inverse and forward analysis.	69
3.29	Bending factors in 26 patient-specific cerebral aneurysms, part I.	70
3.30	Bending factors in 26 patient-specific cerebral aneurysms, part II.	71

3.31	Bending factors in 26 patient-specific cerebral aneurysms, part III. . . .	72
4.1	Schematic illustration of uniformly distributed collagen fibers (Reproduced from [42]).	77
4.2	Prediction of inverse method.	82
4.3	Prediction of inverse method.	84
4.4	Stress distribution.	85
5.1	Flowchart of the pointwise identification procedure for shell structure. . .	87
5.2	Flowchart of the numerical verification.	89
5.3	Assumed stiffness parameter distribution: (a) E_1 ; (b) E_2	90
5.4	Distribution of the first and second principal stretches at $p = 100$ mmHg pressure: (a) λ_2 ; (b) λ_1	92
5.5	Distribution of the first and second principal stresses at $p = 100$ mmHg pressure: (a) $pm_1(N/mm^2)$; (b) $pm_2(N/mm^2)$	92
5.6	Percentage difference in von Mises stress between baseline and stiffer 8-fiber Holzapfel material models.	97
5.7	Distribution of bending factor α	99
5.8	PWIM result for <i>CASE I</i>	100
5.9	Distribution of displacement differences between two sets of material parameters' analysis (%).	102
6.1	Von Mises stress (N/mm^2) and bending factors.	105
6.2	PWIM result for <i>CASE II</i> . (The maximum strain is 0.06).	107
6.3	PWIM result for <i>CASE III</i> . (The maximum strain is 0.06).	108
6.4	PWIM result for <i>CASE IV</i> . (The maximum strain is 0.09).	109
6.5	PWIM result for <i>CASE V</i> . (The maximum strain is 0.05).	110
6.6	PWIM result for <i>CASE VI</i> . (The maximum strain is 0.07).	111

6.7	Schematic illustration of uniformly distributed collagen fibers (Reproduced from [42]).	113
6.8	PWIM result for <i>CASE III</i> without knowing the first fiber direction. . .	116
6.9	PWIM result for <i>CASE V</i> without knowing the first fiber direction. . .	117
6.10	Fiber direction (\mathbf{N}_1) on Gauss points (red dots), <i>CASE III</i> . Red line: identified fiber direction; Blue line: assumed fiber direction.	118
6.11	Fiber direction (\mathbf{N}_1) on Gauss points (red dots), <i>CASE V</i> . Red line: identified fiber direction; Blue line: assumed fiber direction.	119
6.12	Percentage difference in nodal displacement, <i>CASE III</i>	120
6.13	Percentage difference in nodal displacement, <i>CASE V</i>	120
6.14	Method to evaluate the stability of PWIM.	121
6.15	Identification result for <i>CASE II</i> under 1% of perturbation.	123
6.16	Identification result for <i>CASE II</i> under 2% of perturbation.	124
6.17	Percentage difference in displacement under 1% perturbation.	125
6.18	Percentage difference in displacement under 2% perturbation.	126
6.19	Errors in strain and stress data.	126

CHAPTER 1 INTRODUCTION

1.1 Motivation

Biomechanics seeks to understand the mechanics of living systems. For biomedical applications, biomechanics helps us understand the function of organs under normal and pathological conditions as well as medical intervention procedures [15, 16]. Stress analysis is an important field in biomechanical and biomedical engineering; the field has advanced significantly in the past few decades, and new techniques such as imaged-based analyses are gradually becoming the state of art. For example, patient-specific vascular aneurysm model are used for *in vivo* wall stress analysis and rupture risk estimation [52, 77, 51, 102]. However, obtaining the material property of biological material properties remains a difficulty task.

An accurate characterization of the elastic behavior of biological soft tissues requires one to determine suitable constitutive relations and identify corresponding constitutive parameters. This is usually realized by conducting designed experiments and examining the stress-strain relations. As soon as a constitutive model is selected, the model parameters can be identified from the experimental stress-strain data. Although in principle methods of material testing are well known, the applications in soft tissue faces considerable challenges. Among other reasons, soft tissues are in general heterogeneous, anisotropic, nonlinear, and subject-specific. Heterogeneity in particular requires delineating property distributions, a capability most existing do

not have. Scholars have developed many approaches to identify the elastic properties of the materials. The existing methods may be categorized into regression-based and optimization-based methods. These methods have their own advantages and shortcomings. In the soft tissue extension or compression experiments, in order to characterize the material heterogeneity, the testing specimen has to be cut into quite small, which is difficult if not impossible to operate. In addition, the experimental specimen testing method is not suitable for characterizing the material properties in the living conditions. The optimization-based methods are non-invasive and suitable to identify the material properties of the living soft tissues. This family of methods can only characterize the homogeneous material properties in a small domain, not exactly can characterize the material heterogeneities.

1.2 Literature review

As mentioned earlier, existing methods for characterizing material properties of soft tissues may be divided into two categories: regression-based methods, and optimization-based methods. Below, we will briefly review the major contributions in each of the categories and prior scholarships in the area of cerebral aneurysm property identification.

1.2.1 Regression-based methods

The regression-base methods refer to method that characterize the material properties from strain-stress data. A pre-requisite of these methods is the availability of such data. The simplest and most straightforward method is specimen testing

[44, 45, 59, 75]. From the strain-stress data obtained by these experimental tests, researcher first select an appropriate constitutive model, and then conduct the constitutive regression to identify the parameters which best fit the strain-stress data. The earliest study using the specimen testing method to characterize the material properties of rabbit skin was conducted by Lanir and Fung [44, 45]. Afterwards, enormous studies were reported on experimental testing the tissues' material properties in different types of organs; and at the same time, many constitutive equations were proposed to describe the large deformation feature for soft tissue. For example, Hoppin et al. [35] used the triaxial loading experiments to study the material properties of lung tissue. Farshad et al. [11] investigated the material behavior of pig kidney and advised a non-linear theoretical simulation based on the two parameter Blatz model. Davies et al. [7] developed a biomechanical model which described the incompressible, homogeneous, isotropic nonlinear elastic material with an exponential stress-strain law for abdominal (spleen) tissue. The specimen testing is used broadly in characterizing the material properties in soft tissue; however the method has some limitations. First and foremost, the method is destructive. Although recently researchers developed instrumentations [30, 29, 31, 76] for testing the soft tissue *in vivo*, the procedure is still somehow destructive. Second, the specimen testing methods can only provide the average properties of the testing tissue. Usually, the material properties in the soft tissues are heterogeneous. In order to identify the heterogeneous material properties, the testing tissue must be cut into quite small pieces, which increases the difficulties of the experiments.

Another method for feature hyperelastic material characterization is the axisymmetric membrane inflation test [14, 92, 63, 86]. The inflation method was first used by Treloar [79, 80, 81] to study the hyperelastic material properties in the isotropic rubbers. Wineman et al. [89] applied the axisymmetric membrane inflation test on soft tissue and determined the strain energy density function for the specimen. Hsu et. al [28, 27, 26] developed a experimental system to perform the axisymmetric membrane inflation test on biomembranes, and then applied this experiment to investigate the nonlinear material properties on saccular aneurysms. This method inflates an axisymmetric membrane structure into several deformed configurations. The stain data can be measured experimentally. Base on the membrane assumption and axisymmetric geometry, the stress distribution along the meridian can be calculated by the analytical formula. With the strain-stress data, the material properties can be identified through constitutive regression. The axisymmetric membrane inflation methods, though being able to delineate stress-strain relation directly from experimental data and providing pointwise material properties' distributions along the meridian, are limited to axisymmetric geometry, not applicable to systems of other geometries.

1.2.2 Optimization-based methods

Optimization-based methods (also called inverse finite element method) are broadly used in characterizing the material properties of living organs because of its non-destructive feature [37, 34, 2]. In optimization-based methods, material param-

eter identification is often carried out by iterating between stress analysis (using e.g. finite element analysis) and optimization techniques to estimate the model parameters. The model parameters are typically optimized altogether by minimizing the difference between experimental and simulated data of displacement or force, etc. Kyriacou et al. coined the term “inverse finite element method” , which is an optimization method using finite element method to solve boundary value problems. They [43] presented the numerical and experimental results and showed the inverse finite element method was very useful by the rubber membranes. Kauer et al. [36] presented a soft tissue characterization method which was validated through experiments on synthetic materials and was applied on human uteri. Liu et al. [46] used inverse finite element modeling method to determine the material parameters of breast tissue from indentation experiments. Kim et al. [38] characterized the material properties of intra-abdominal organs using *in vivo* animal experimental data and inverse FE parameter estimation algorithm. Erdemir et al. [9] used a numerical-experimental approach to characterize material properties of heel-pad. Samur et al. [62] used ANSYS finite element package to estimate the optimum values of viscoelastic and nonlinear hyperelastic material properties of pig liver.

These methods couple stress-strain data acquisition and optimization, so they are limited by the size of the optimization problem, namely the number of parameters in the model. When the number is large, the optimization solution is not robust due to the presence of local minima. In addition, the coupled iteration between finite element analysis and optimization makes it difficult to locate the root of the

identification error.

1.2.3 Inverse studies in cerebral aneurysms

In the study of material properties in cerebral aneurysms, in order to best fit the experimental data, different kinds of material models were proposed to described the nonlinear, anisotropic, collagen fibers feature in soft tissues [64, 21, 74, 78]. For example, Canham et al. [5] constructed a mathematical model base on autopsy specimens in the laboratory to study the mechanics of saccular aneurysms; and later in [6] presented that the cerebral aneurysm wall contained many, very thin sub-layers. Holzapfel and Kroon [40, 42] proposed a new constitutive model to described the multi-layered collagenous structures in cerebral aneurysms.

Seshaiyer and Humphery et al. are the only group who did experimental work on harvested human tissues. They first developed the “inverse finite element method” to characterize the material properties in rubber membranes. This non-invasive optimization-based methods are broadly used in characterizing the material properties in cerebral aneurysms. This kind of method came with shortcomings, especially in characterizing the heterogeneous material properties. As a remedy to the global optimization, in [65, 66], they developed a sub-domain inverse finite element method where the optimization problem is formulated regionally not globally. In [65], Seshaiyer et al. determined the mechanical properties of human intracranial saccular aneurysm and estimate the material parameters in a Fung-type material model. The material heterogeneity they defined only contained 2-3 sets of different

material parameters. Because of the optimization based approach, this method can not identify the constitutive response directly from strain-stress data.

Holzapfel and Kroon [41] described an inverse finite element procedure of determining properties and used a numerical simulation on saccular cerebral aneurysm (sphere geometry) to verify their method. The nonlinear constitutive model contains four heterogeneous material parameters (two elastic stiffness of the collagen fabric in two principal direction, one angle parameter defined the fiber orientation, and one constant parameter described the fiber nonlinearity). This is the first investigation to predict the distribution of anisotropic material properties in cerebral aneurysms. However, this approach is also a optimization-based method.

Balocco et al. [3, 4] investigated the feasibility of characterizing the regional mechanical properties of cerebral aneurysm *in vivo*. This is a comprehensive study despite that the material model is simple (isotropic material). They generated MR images from FEM, and used image segmentation to derive the moving mesh in the wall motions. They concluded that the current image resolution is insufficient for inverse characterization of cerebral aneurysm tissue properties, even for simple heterogeneous distribution.

1.2.4 Pointwise Identification Method

Recently, the pointwise identification method (PWIM) has been proposed [47, 96, 98, 97]. This is a regression-based method. However, unlike the specimen test which essentially works on a material point, the method works simultaneously on

many material points in parallel, and thus can sharply identify the distribution of heterogeneous properties.

PWIM is a generalization of the membrane inflation test. Traditional inflation test is for axisymmetric structures; for such structures the stress in the wall can be obtained analytically using the Laplace formula. In contrast, PWIM applies to membrane structure without any geometric symmetry. The method is certainly a step forward toward application in realistic thin tissue structures. This method exploits the static determinant property in membrane structure to obtain the stress data through inverse method [48, 49]. In PWIM, instead of using an analytical solution, the stress is computed numerically using the membrane inverse method [49], a subclass of the finite element inverse elastostatic method (FEIEMs) [19, 90, 91, 49]. The inverse approach can effectively predict the wall stress using the assumed material models. The PWIM is non-destructive, and can identify the heterogeneous material because of its pointwise feature. It decouples stress-strain data acquisition and constitutive regression, thus can identify the material properties in arbitrary distribution.

The pointwise identification method, although very promising, has a limitation related to the membrane assumption. The inverse membrane simulation in [49] assumed that the thin wall structure is a thin convex or saddle membrane that does not sustain bending and transverse shear. This assumption is inadequate for thin structures with concave geometries. The membrane assumption precludes the application to a large family of realistic structures.

1.3 Objectives

The objective of this study is to extend PWIM to membrane structures that have concave or saddle regions and to investigate the applicability of the method in such structures. The study can be divided into four tasks.

The first task is to investigate the insensitivity of wall stress to the material model in thin shell structures. This is an important first step, because the PWIM hinges on the static determinacy property of the equilibrium problem of thin structure. By thinness, the material is locally in a 2D stress state and therefore may be determined from static equilibrium alone. If substantial bending moment and transverse shear are required to achieve equilibrium, static determinacy is lost and the method may not apply. However, in between the membrane structure and thick shells there should be a family of thin shells which should be regarded approximately statically determined. This happens when the bending moment and transverse shear are much smaller compare to the in-plane stress. The question then is that, to what extend the property of static determinacy remains a reasonable approximation, and how do we quantify it. In this work, we first look at tubular versus saccular structures using examples of abdominal aortic aneurysms (AAAs) and cerebral aneurysms. We conduct sensitivity analysis numerically by comparing the stress solutions from different material models. To quantify the influence of bending, the bending stresses are also compared with the stress differences. Through the comparison of bending stress and stress insensitivity between tubular and saccular structures, we will find a geometry which can keep lower bending stress and better stress insensitivity character.

The second task is to establish the shell structure pointwise identification method. Algorithmic details of the three components of the method, namely stress analysis, strain analysis, and parameter regression, will be presented in detail. This task also include the implementation of a hyperelastic material body for cerebral aneurysm tissues in a forward and an inverse shell element. The 8-fiber Holzapfel material model is used to described the cerebral aneurysm wall tissue. The material model will be later used in cerebral aneurysm analysis.

The third task is to evaluate the shell PWIM numerically on cerebral aneurysm models of concave of saddle surfaces. We will use numerically generated inflation data to drive the inverse analysis to back out the assumed heterogeneous properties in the aneurysm wall. A group of image derived cerebral aneurysm models will be used in this study. The surface geometry of which represents typical surface features of realistic aneurysm. Through this study, we hope to gain a better understanding of the method and come up with recommendations on the applicability of the method.

The fourth task is to investigate the robustness of the method at the presence of noise. In real application, the deformed configuration will be constructed from medical imagines, in which error is inevitable. In this study, the geometric errors will be introduced numerically and the performance of PWIM will be studied.

1.4 Organization

The thesis proposal is organized as follows. In Chapter 2, the theoretical background of PWIM is introduced. The formulation for geometrically exact stress

resultant shell is also described.

In Chapter 3, the stress insensitivity is investigated by using two AAAs models, and 27 cerebral aneurysm models of realistic geometries. Sensitivity of stress solution in both forward and inverse analyses are reported.

In Chapter 4, the 8-fiber Holzapfel material model is implemented into the forward and inverse shell elements. The elements are verified using an forward-inverse loop in which the forward deformation is fed to the inverse analysis to see if the inverse solution can exactly revert the deformation. In addition, the inverse formulation is tested using a problem in which the exact asymptotic stress field is known.

The shell PWIM is discussed in Chapter 5. The method is presented in detail. This chapter also presents the validation of the shell PWIM using numerical experiments on a realistic cerebral aneurysm model with heterogeneous material properties. The predictive capability of identified parameters is tested using a forward analysis at a different load.

Chapter 6 evaluates the applicability of shell PWIM. In this chapter, five typical cerebral aneurysms are selected and conducted the shell PWIM. The identification accuracy is demonstrated by comparing the relative error between the assumed and identified material parameters. The robustness of shell PWIM is investigated in this chapter. The shell PWIM is applied on a cerebral aneurysm when the deformed configurations are perturbed by random noise. The identified parameters' accuracy and predicability will be examined.

Conclusions and the outlook are contained in Chapter 7.

CHAPTER 2 THEORETICAL BACKGROUND

Identifying the elastic properties in a soft tissue structure has long been a very challenging problem. Especially the identification which requires to be performed in the service conditions of living tissues and organs, i.e. *in vivo*, or identifying the heterogeneous material, presents more challenges. The pointwise identification method (PWIM) was proposed to identify the elastic properties in the nonlinear heterogeneous membrane. Fundamentally, this method hinges on the unique feature of membrane equilibrium problems, that is, the wall stress depends on geometry and load, not wall material property [49]. In theory, for a sac-like structure under internal pressure, if the deformed shape is known, the wall stress can be determined from the deformed geometry and load. This feature is critical for material characterization because one can obtain stress data without invoking the material property in question. In PWIM, the stress are computed using the inverse elastostatic method which takes the deformed configuration as the input. Having stress and strain, the local properties are determined directly from the pointwise strain-stress data [47, 96]. In this chapter, the main features of the theoretical background of PWIM are reviewed.

2.1 Membrane theory

2.1.1 Kinematics

A membrane is a thin continuum in which one of the dimensions is significantly smaller than the other two. There are many ways to present the membrane equations,

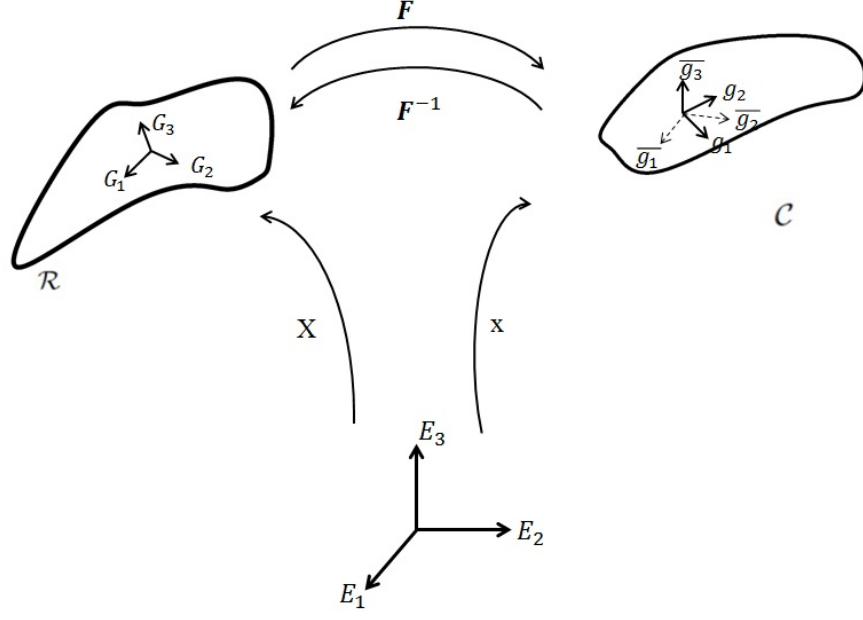


Figure 2.1: Schematic illustration of the kinematic map.

we use tensorially covariant forms based on convected coordinates. Let $\mathbf{X} = \mathbf{X}(\xi^1, \xi^2)$ and $\mathbf{x} = \mathbf{x}(\xi^1, \xi^2)$ be the positions of a material point in the initial ($\mathcal{R} \in \mathbb{R}^2$) and deformed ($\mathcal{C} \in \mathbb{R}^2$) configurations in Figure 2.1. The surface is parameterized by surface convected coordinates ξ^α ($\alpha = 1, 2$). If we define $\mathbf{G}_\alpha = \frac{\partial \mathbf{X}}{\partial \xi^\alpha}$ and $\mathbf{g}_\alpha = \frac{\partial \mathbf{x}}{\partial \xi^\alpha}$ as the basis vector in the reference and current configuration, respectively, it is obviously that

$$d\mathbf{X} = \mathbf{G}_\alpha d\xi^\alpha, \quad d\mathbf{x} = \mathbf{g}_\alpha d\xi^\alpha. \quad (2.1)$$

Repeated indices means the summation convention.

The deformation gradient \mathbf{F} is defined as $\mathbf{F} = \frac{\partial \mathbf{x}}{\partial \mathbf{X}}$. In the convected coordinate system, the deformation gradient can be written as

$$d\mathbf{x} = \mathbf{F}d\mathbf{X} \quad \Leftrightarrow \quad \mathbf{g}_\alpha d\xi^\alpha = \mathbf{F}\mathbf{G}_\alpha d\xi^\alpha. \quad (2.2)$$

Here we focus on the in-plane part of the deformation gradient and thus $d\mathbf{x}$ and $d\mathbf{X}$ are vectors tangent to the membrane surface. We denote the contravariant surface base vector as \mathbf{G}^α for referential configuration. According to the definition of the dual surface basis vectors, $\mathbf{G}^\alpha \cdot \mathbf{G}_\beta = \delta_\beta^\alpha$, (δ_β^α is the Kronecker delta), \mathbf{G}^α can be computed as follow

$$\mathbf{G}^\alpha = G^{\alpha\beta} \mathbf{G}_\beta, \quad (2.3)$$

where $G^{\alpha\beta}$ can be computed through the inverse of the matrices $[G_{\alpha\beta}]$, $[G^{\alpha\beta}] = [G_{\alpha\beta}]^{-1}$. The components of metric tensor $G_{\alpha\beta}$ are defined as

$$G_{\alpha\beta} = \mathbf{G}_\alpha \cdot \mathbf{G}_\beta. \quad (2.4)$$

Likewise for the current configuration, the dual basis vector is $\mathbf{g}^\alpha = g^{\alpha\beta} \mathbf{g}_\beta$, where $g_{\alpha\beta} = \mathbf{g}_\alpha \cdot \mathbf{g}_\beta$.

The in-plane part of the deformation gradient, still denoted as \mathbf{F} , can be written with the convected basis

$$\mathbf{F} = \mathbf{g}_\alpha \otimes \mathbf{G}^\alpha, \quad (2.5)$$

and the inverse deformation gradient and the transpose of \mathbf{F} which will be used in the future are defined by

$$\mathbf{F}^{-1} = \mathbf{G}_\alpha \otimes \mathbf{g}^\alpha, \quad \mathbf{F}^T = \mathbf{G}^\alpha \otimes \mathbf{g}_\alpha. \quad (2.6)$$

The Green-Lagrangian strain tensor is

$$\mathbf{E} = \frac{1}{2}(\mathbf{F}^T \mathbf{F} - \mathbf{I}), \quad (2.7)$$

\mathbf{I} here is the identify tensor. Like previous transformation of \mathbf{F} , the Green-Lagrangian strain tensor can be also written in the convected basis

$$\mathbf{E} = \frac{1}{2}((\mathbf{G}^\alpha \otimes \mathbf{g}_\alpha)(\mathbf{g}_\alpha \otimes \mathbf{G}^\alpha) - \mathbf{I}) = \frac{1}{2}(g_{\alpha\beta}\mathbf{G}^\alpha \otimes \mathbf{G}^\beta - \mathbf{I}). \quad (2.8)$$

For the identify tensor \mathbf{I} , it can be written as $\mathbf{I} = G_{\alpha\beta}\mathbf{G}^\alpha \otimes \mathbf{G}^\beta$, the reason is as follow

$$G_{\alpha\beta}\mathbf{G}^\alpha \otimes \mathbf{G}^\beta = (\mathbf{G}_\alpha \cdot \mathbf{G}_\beta)\mathbf{G}^\alpha \otimes \mathbf{G}^\beta = (\mathbf{G}^\alpha \otimes \mathbf{G}_\alpha)\mathbf{G}_\beta \otimes \mathbf{G}^\beta = \mathbf{I}. \quad (2.9)$$

The Green-Lagrangian strain tensor can be computed with the metric tensor

$$\mathbf{E} = \frac{1}{2}(g_{\alpha\beta} - G_{\alpha\beta})\mathbf{G}^\alpha \otimes \mathbf{G}^\beta. \quad (2.10)$$

The Cauchy-Green deformation tensor is

$$\mathbf{C} = \mathbf{F}^T \mathbf{F} = g_{\alpha\beta}\mathbf{G}^\alpha \otimes \mathbf{G}^\beta. \quad (2.11)$$

2.1.2 Kinetics

The static equilibrium of the membrane is governed by the balance equation [20, 53]

$$\frac{1}{\sqrt{g}}(\sqrt{g}t^{\alpha\beta}\mathbf{g}_\alpha)_{,\beta} + \mathbf{b} = 0, \quad (2.12)$$

where $g = \det(g_{\alpha\beta})$, $t^{\alpha\beta}$ is the component of the Cauchy stress resultant tensor \mathbf{t} , written as $\mathbf{t} = t^{\alpha\beta}\mathbf{g}_\alpha \otimes \mathbf{g}_\beta$, \mathbf{b} is the external force per unit current area [49].

The relation between Cauchy stress $\boldsymbol{\sigma}$ and Cauchy stress resultant \mathbf{t} can be described as $\mathbf{t} = \int_{-\frac{h}{2}}^{\frac{h}{2}} \boldsymbol{\sigma} dh \approx h\boldsymbol{\sigma}$ and in components $t^{\alpha\beta} \approx h\sigma^{\alpha\beta}$, where h is the thickness. In this work, for the convenient in the inverse calculation, $t^{\alpha\beta}$ here is the components of stress resultant tensor in the deformed configuration basis. Note

that as the tension (resultant) tensor, \mathbf{t} can be written in any configurations basis, i.e. $\mathbf{t} = T^{\alpha\beta} \mathbf{G}_\alpha \otimes \mathbf{G}_\beta$, where $T^{\alpha\beta}$ is the resultant components in the reference configuration basis.

2.1.3 Constitutive relations

Constitutive equations describe material response to applied mechanical or other types of loads. We first define \mathbf{S} as the second Piola-Kirchhoff stress. The relation between Cauchy stress tensor $\boldsymbol{\sigma}$ and second Piola-Kirchhoff stress tensor \mathbf{S} is written as follow

$$\boldsymbol{\sigma} = J^{-1} \mathbf{F} \mathbf{S} \mathbf{F}^T, \quad (2.13)$$

where $J = \det \mathbf{F} = \sqrt{\frac{g}{G}}$ is the surface Jacobian, g and G are the determinants of the matrices $[g_{\alpha\beta}]$ and $[G_{\alpha\beta}]$, respectively. The second Piola-Kirchhoff stress plays a pivoting role in the energetic development and constitutive relations.

If we define \mathbf{T}_s as the second Piola-Kirchhoff stress resultant, the transformation for stress resultant reads

$$\mathbf{T}_s = \mathbf{F}^{-1} (J \mathbf{t}) \mathbf{F}^{-T}, \quad J = \det \mathbf{F}. \quad (2.14)$$

Introducing $\mathbf{t} = t^{\alpha\beta} \mathbf{g}_\alpha \otimes \mathbf{g}_\beta$ and Eq. (2.6) in Eq. (2.14), \mathbf{T}_s can be written in the convected basis

$$\mathbf{T}_s = \mathbf{G}_\delta \otimes \mathbf{g}^\delta (J t^{\alpha\beta} \mathbf{g}_\alpha \otimes \mathbf{g}_\beta) \mathbf{g}^\gamma \otimes \mathbf{G}_\gamma = J t^{\alpha\beta} \mathbf{G}_\alpha \otimes \mathbf{G}_\beta. \quad (2.15)$$

The constitutive equation of a hyperplastic membrane is specified by a surface strain energy function ψ . The second Piola-Kirchhoff stress tensor \mathbf{T}_s usually can be

computed through strain energy relation

$$\mathbf{T}_s = \frac{\partial \psi}{\partial \mathbf{E}}. \quad (2.16)$$

In the convected basis, \mathbf{T}_s can be understood as the function of the $g_{\alpha\beta}$. We further use chain rule and get

$$\mathbf{T}_s = 2 \frac{\partial \psi}{\partial g_{\alpha\beta}} \mathbf{G}_\alpha \otimes \mathbf{G}_\beta. \quad (2.17)$$

If we write tensor \mathbf{T}_s in the referential configuration's basis $\mathbf{T}_s = T_s^{\alpha\beta} \mathbf{G}_\alpha \otimes \mathbf{G}_\beta$, we can get

$$T_s^{\alpha\beta} = 2 \frac{\partial \psi}{\partial g_{\alpha\beta}}. \quad (2.18)$$

Comparing Eq. (2.17) with Eq. (2.15), for component, it's obviously that

$$J t^{\alpha\beta} = 2 \frac{\partial \psi}{\partial g_{\alpha\beta}} = T_s^{\alpha\beta}. \quad (2.19)$$

Note that $t^{\alpha\beta}$ here is the components of Cauchy stress resultant \mathbf{t} in the convected basis of deformed configuration, and $T_s^{\alpha\beta}$ is the components of second Piola-Kirchhoff stress resultant tensor \mathbf{T}_s in the convected basis of the referential configuration. This expression is very useful in the inverse calculation. We will expand the discussion in the inverse shell theory.

Here we use a hyperelastic material model proposed by Holzapfel et al. [25, 24, 23] as an example to explain how to derive the stress with convected basis. Holzapfel's models assume that the material consists of anisotropic matrix reinforced by two families of fibers. Orthotropic means the two families of fibers are perpendicular to each other. Also, if one family of fibers presents, the material reduces to transversely

isotropic. We recall the Cauchy-Green deformation tensor $\mathbf{C} = \mathbf{F}^T \mathbf{F} = 2\mathbf{E} + \mathbf{I}$. From the alternation in last section, it's easy to get $\mathbf{T}_s = 2 \frac{\partial \psi}{\partial \mathbf{C}}$.

Let \mathbf{N}_1 and \mathbf{N}_2 be the two families of fibers' directions. The energy function in this material model depends on the following invariants of tensor \mathbf{C}

$$I_1 = tr \mathbf{C}, \quad I_2 = det \mathbf{C}, \quad (2.20)$$

as the isotropic part, and

$$I_4 = \mathbf{N}_1 \cdot \mathbf{C} \mathbf{N}_1, \quad I_6 = \mathbf{N}_2 \cdot \mathbf{C} \mathbf{N}_2 \quad (2.21)$$

as the anisotropic part. Substituting $\mathbf{C} = g_{\alpha\beta} \mathbf{G}^\alpha \otimes \mathbf{G}^\beta$ into Eq. (2.20), we express the invariants in tonsorially invariant forms:

$$I_1 = g_{\alpha\beta} G^{\alpha\beta}, \quad I_2 = \frac{g}{G}. \quad (2.22)$$

In Eq. (2.21), I_4 and I_6 are the square stretches of along the fiber directions \mathbf{N}_1 and \mathbf{N}_2 , respectively. In the reference configuration, \mathbf{N}_1 and \mathbf{N}_2 can be written as $\mathbf{N}_1 = N_1^\alpha \mathbf{G}_\alpha$ and $\mathbf{N}_2 = N_2^\alpha \mathbf{G}_\alpha$ respectively. Therefore I_4 and I_6 can be written as

$$I_4 = \frac{N_1^\alpha g_{\alpha\beta} N_1^\beta}{N_1^\delta G_{\delta\gamma} N_1^\gamma}, \quad I_6 = \frac{N_2^\alpha g_{\alpha\beta} N_2^\beta}{N_2^\delta G_{\delta\gamma} N_2^\gamma}. \quad (2.23)$$

Holzapfel suggested a reduced energy form that depends on I_1 , I_2 , I_4 and I_6 only. The energy function assumes the form

$$\psi = \psi_{iso}(I_1, I_2) + \psi_{anis}(I_4, I_6). \quad (2.24)$$

The components of \mathbf{T}_s follows as

$$\begin{aligned} T_s^{\alpha\beta} = & 2 \frac{\partial \psi_{iso}}{\partial I_1} G^{\alpha\beta} + 2 I_2 \frac{\partial \psi_{iso}}{\partial I_2} g^{\alpha\beta} + 2 (N_1^\delta G_{\delta\gamma} N_1^\gamma)^{-1} I_4 \frac{\partial \psi_{anis}}{\partial I_4} N_1^\alpha N_1^\beta + \\ & 2 (N_2^\delta G_{\delta\gamma} N_2^\gamma)^{-1} I_6 \frac{\partial \psi_{anis}}{\partial I_6} N_2^\alpha N_2^\beta, \end{aligned} \quad (2.25)$$

where $\alpha, \beta, \delta, \gamma = 1, 2$, and repeating index implies summation.

2.2 Shell theory

In this section, we review the basic theory of stress resultant shell. A shell is a curved surface-like continuum which is significantly thin in comparison to its span. Kinematically, a shell is described by a deformable mid-surface, and the rotation of the normal of the middle surface. The shell theory we used is the geometrically exact stress resultant shell elements originally developed by Simo's group [69, 70, 71, 72, 73, 68], which are based on the direct shell theory [10]. The inverse formulations of the stress resultant shell was developed by Zhou and Lu in [101].

2.2.1 Kinematics

In the direct shell theory, the shell kinematics is described by a pair of deformation fields, $(\boldsymbol{\phi}, \mathbf{d})$, where $\boldsymbol{\phi}$ presents the position of the mid-surface, and \mathbf{d} , the director field, describes the surface normal. If we use $\mathcal{R} \subset \mathbb{R}^3$ to indicate the reference configuration, as showed in Figure 2.2, \mathcal{R} can be described as

$$\mathcal{R} := \{\mathbf{X} \in \mathbb{R}^3 | \mathbf{X} = \boldsymbol{\Phi} + \xi \mathbf{D}, \xi \in \left[-\frac{h}{2}, \frac{h}{2}\right]\}, \quad (2.26)$$

where h is the thickness of the shell. Likewise the deformed configuration \mathcal{C} can be written as

$$\mathcal{C} := \{\mathbf{x} \in \mathbb{R}^3 | \mathbf{x} = \boldsymbol{\phi} + \xi \mathbf{d}, \xi \in \left[-\frac{h}{2}, \frac{h}{2}\right]\}. \quad (2.27)$$

If we use (ξ^1, ξ^2) to represent the surface coordinate, as illustrated in Figure 2.2, \mathbf{x}

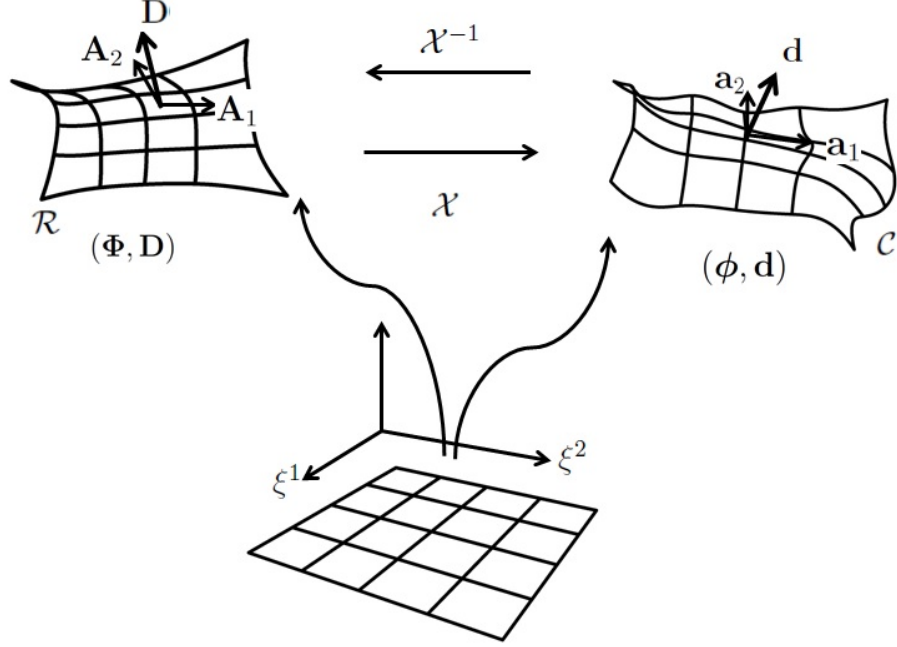


Figure 2.2: Illustration of shell deformation.

can be written as

$$\mathbf{x} = \boldsymbol{\phi}(\xi^1, \xi^2) + \xi \mathbf{d}(\xi^1, \xi^2). \quad (2.28)$$

(ξ^1, ξ^2) form a convected coordinate system. \mathbf{X} is

$$\mathbf{X} = \boldsymbol{\Phi}(\xi^1, \xi^2) + \xi \mathbf{D}(\xi^1, \xi^2). \quad (2.29)$$

The convected basis vectors in the current configuration $\mathbf{g}_I = \frac{\partial \mathbf{x}}{\partial \xi^I}$, $(I = 1, 2, 3)$

can be written as:

$$\mathbf{g}_\alpha = \boldsymbol{\phi}_{,\alpha} + \xi \mathbf{d}_{,\alpha}, \quad \mathbf{g}_3 = \mathbf{d}. \quad (2.30)$$

While in the reference configuration,

$$\mathbf{G}_\alpha = \boldsymbol{\Phi}_{,\alpha} + \xi \mathbf{D}_{,\alpha}, \quad \mathbf{G}_3 = \mathbf{D}. \quad (2.31)$$

The Latin indices range from 1 to 3 and the Greek indices range from 1 to 2. The subscript comma followed by an index denotes the derivative with respect to the corresponding coordinate.

On the mid-surface where $\xi = 0$, if we use \mathbf{a}_α to denote the basis vectors, we get

$$\mathbf{a}_\alpha = \boldsymbol{\phi}_{,\alpha}, \quad \mathbf{a}_3 = \mathbf{d}. \quad (2.32)$$

In the reference configuration,

$$\mathbf{A}_\alpha = \boldsymbol{\Phi}_{,\alpha}, \quad \mathbf{A}_3 = \mathbf{D}. \quad (2.33)$$

Note that the surface basis vectors \mathbf{a}_α and \mathbf{A}_α here can be understood as the basis vectors \mathbf{g}_α and \mathbf{G}_α discussed in membrane theory in section § 2.1. As described in the membrane theory, the in plane deformation gradient can be written as

$$\mathbf{F} = \mathbf{a}_\alpha \otimes \mathbf{A}^\alpha. \quad (2.34)$$

The Cauchy-Green deformation tensor is

$$\mathbf{C} = \mathbf{F}^T \mathbf{F} = a_{\alpha\beta} \mathbf{A}^\alpha \otimes \mathbf{A}^\beta. \quad (2.35)$$

2.2.2 Balance laws

To present the equilibrium equation of the shell, we first define the surface Jacobian $\sqrt{a} = \|\mathbf{a}_1 \times \mathbf{a}_2\|$. We define $\tilde{\mathbf{m}}^\alpha$ the director stress

$$\tilde{\mathbf{m}}^\alpha := \frac{1}{\sqrt{a}} \int_{-\frac{h}{2}}^{\frac{h}{2}} \xi \boldsymbol{\sigma} \mathbf{g}^\alpha j d\xi, \quad (2.36)$$

$\boldsymbol{\sigma}$ is the Cauchy stress, we can get the stress resultant \mathbf{t}^α and stress couple \mathbf{m}^α as

$$\begin{aligned}\mathbf{t}^\alpha &:= \frac{1}{\sqrt{a}} \int_{-\frac{h}{2}}^{\frac{h}{2}} \boldsymbol{\sigma} \mathbf{g}^\alpha j d\xi, \\ \mathbf{m}^\alpha &:= \mathbf{d} \times \frac{1}{\sqrt{a}} \int_{-\frac{h}{2}}^{\frac{h}{2}} \xi \boldsymbol{\sigma} \mathbf{g}^\alpha j d\xi.\end{aligned}\tag{2.37}$$

Here \mathbf{g}^α is the dual basis of \mathbf{g}_α . j is the Jacobian of configuration mapping. From [69], we can get that $j = [\mathbf{g}_1 \times \mathbf{g}_2] \cdot \mathbf{g}_3$.

The momentum equations for the shell take the form

$$\begin{aligned}\frac{1}{\sqrt{a}}(\sqrt{a}\mathbf{t}^\alpha)_{,\alpha} + \bar{\mathbf{t}} &= \mathbf{0}, \\ \frac{1}{\sqrt{a}}(\sqrt{a}\mathbf{m}^\alpha)_{,\alpha} + \boldsymbol{\phi}_{,\alpha} \times \mathbf{t}^\alpha + \bar{\mathbf{m}} &= \mathbf{0}.\end{aligned}\tag{2.38}$$

$\bar{\mathbf{t}}$ and $\bar{\mathbf{m}}$ are the resultants of the external force and couple, respectively.

Calculations are carried in the convected coordinate system. The stress and stress couple resultants in the convected surface for current configuration can be written as follows:

$$\begin{aligned}\tilde{\mathbf{t}} &:= \tilde{t}^{\alpha\beta} \mathbf{a}_\alpha \otimes \mathbf{a}_\beta, \\ \tilde{\mathbf{q}} &:= \tilde{q}^\alpha \mathbf{a}_\alpha, \\ \tilde{\mathbf{m}} &:= \tilde{m}^{\alpha\beta} \mathbf{a}_\alpha \otimes \mathbf{a}_\beta,\end{aligned}\tag{2.39}$$

where $\tilde{\mathbf{t}}$ and $\tilde{\mathbf{q}}$ are the effective membrane and shear stress resultants. The components $\tilde{t}^{\alpha\beta}$ and \tilde{q}^α are defined by

$$\tilde{t}^{\alpha\beta} = t^{\alpha\beta} - \lambda_\mu^\alpha \tilde{m}^{\beta\mu}, \quad \tilde{q}^\alpha = q^\alpha - \lambda_\mu^3 \tilde{m}^{\alpha\mu},\tag{2.40}$$

where λ_μ^α and λ_μ^3 are coefficients in $\mathbf{d}_{,\alpha} = \lambda_\mu^\alpha \mathbf{a}_\mu + \lambda_\mu^3 \mathbf{d}$ [69].

Note that $\tilde{t}^{\alpha\beta}$, $\tilde{m}^{\alpha\beta}$ and \tilde{q}^α are the components of the effective Cauchy stress, stress couple resultants and transverse shear resultants. To make it clear, we write

out the full tensors

$$\begin{aligned}
\tilde{\mathbf{t}} &= \tilde{t}_{\alpha\beta} \mathbf{a}_\alpha \otimes \mathbf{a}^\beta = \tilde{T}_{\alpha\beta} \mathbf{A}_\alpha \otimes \mathbf{A}^\beta, \\
\tilde{\mathbf{m}} &= \tilde{m}_{\alpha\beta} \mathbf{a}_\alpha \otimes \mathbf{a}^\beta = \tilde{M}_{\alpha\beta} \mathbf{A}_\alpha \otimes \mathbf{A}^\beta, \\
\tilde{\mathbf{q}} &= \tilde{q}_\alpha \mathbf{a}_\alpha = \tilde{Q}_\alpha \mathbf{A}^\alpha.
\end{aligned} \tag{2.41}$$

To establish the weak form from Eq. (2.38), we first introduce the deformation measures that defined the local deformation of the shell

$$\begin{aligned}
a_{\alpha\beta} &:= \mathbf{a}_\alpha \cdot \mathbf{a}_\beta, & A_{\alpha\beta} &:= \mathbf{A}_\alpha \cdot \mathbf{A}_\beta, \\
\kappa_{\alpha\beta} &:= \mathbf{a}_\alpha \cdot \mathbf{d}_{,\beta}, & K_{\alpha\beta} &:= \mathbf{A}_\alpha \cdot \mathbf{D}_{,\beta}, \\
\gamma_\alpha &:= \mathbf{a}_\alpha \cdot \mathbf{d}, & \Gamma_\alpha &:= \mathbf{A}_\alpha \cdot \mathbf{D}.
\end{aligned} \tag{2.42}$$

In the membrane theory, we have already shown that the membrane Green-Lagrangian strain can be computed by

$$\boldsymbol{\varepsilon} := \varepsilon_{\alpha\beta} \mathbf{A}^\alpha \otimes \mathbf{A}^\beta = \frac{1}{2} (a_{\alpha\beta} - A_{\alpha\beta}) \mathbf{A}^\alpha \otimes \mathbf{A}^\beta. \tag{2.43}$$

The curvatures and transverse shear strain defined relative to the convected coordinate can be written as

$$\begin{aligned}
\boldsymbol{\rho} &:= \rho_{\alpha\beta} \mathbf{A}^\alpha \otimes \mathbf{A}^\beta = (\kappa_{\alpha\beta} - K_{\alpha\beta}) \mathbf{A}^\alpha \otimes \mathbf{A}^\beta, \\
\boldsymbol{\delta} &:= \delta_\alpha \mathbf{A}^\alpha = (\gamma_\alpha - \Gamma_\alpha) \mathbf{A}^\alpha.
\end{aligned} \tag{2.44}$$

The stress resultant can be computed through constitutive relations which relate them to the deformation measures introduced in Eq. (2.42). We use ψ represents energy in shell structure, and \mathbf{T}_s , to represent these second Piola-Kirchhoff stress resultant tensors. The components of $(\mathbf{T}_s, \mathbf{M}_s, \mathbf{Q}_s)$ in referential convected basis can

be computed through constitutive equations:

$$\begin{aligned}\tilde{T}_s^{\alpha\beta} &= \frac{\partial\psi}{\partial\varepsilon_{\alpha\beta}} = 2\frac{\partial\psi}{\partial a_{\alpha\beta}} = J\tilde{t}^{\alpha\beta}, \\ \widetilde{M}_s^{\alpha\beta} &= \frac{\partial\psi}{\partial\rho_{\alpha\beta}} = J\tilde{m}^{\alpha\beta}, \\ \tilde{Q}_s^\alpha &= \frac{\partial\psi}{\partial\delta_\alpha} = J\tilde{q}^\alpha.\end{aligned}\tag{2.45}$$

$J = \sqrt{\frac{a}{A}}$, where $a = \det(a_{\alpha\beta})$ and $A = \det(A_{\alpha\beta})$, so J is the area stretch.

We can further get the weak form of the equilibrium equations Eq. (2.38)

$$\int_{\mathcal{A}_{\mathcal{R}}} [\tilde{T}_s^{\alpha\beta} \delta\varepsilon_{\alpha\beta} + \tilde{M}_s^{\alpha\beta} \delta\rho_{\alpha\beta} + \tilde{Q}_s^\alpha \delta\delta_\alpha] d\mu - G_{ext}(\delta\boldsymbol{\psi}) = 0, \tag{2.46}$$

where $\mathcal{A}_{\mathcal{R}}$ is the referential surface area, $d\mu = \|\mathbf{A}_1 \times \mathbf{A}_2\| d\xi^1 d\xi^2$ is the area element, and $G_{ext}(\delta\boldsymbol{\psi})$ is the virtual work done by external force and moment [69].

Corresponding to the 2nd Piola-Kirchhoff stress resultant tensor Eq. (2.15), in the mid-surface (2D problem), the referential resultant tensor can be written as

$$\tilde{\mathbf{T}}_s = J\tilde{t}^{\alpha\beta} \mathbf{A}_\alpha \otimes \mathbf{A}_\beta, . \tag{2.47}$$

Similarly, the referential stress couple and transverse shear stress resultant can be written as

$$\widetilde{\mathbf{M}}_s = J\tilde{m}^{\alpha\beta} \mathbf{A}_\alpha \otimes \mathbf{A}_\beta, \quad \tilde{\mathbf{Q}}_s = J\tilde{q}^\alpha \mathbf{A}_\alpha. \tag{2.48}$$

If we use $(\delta\boldsymbol{\phi}, \delta\mathbf{d})$ represents the admissible variations on the current configuration, the variations of the strain components in Eq. (2.42) follow as

$$\begin{aligned}\delta a_{\alpha\beta} &= \delta\boldsymbol{\phi}_{,\alpha} \cdot \boldsymbol{\phi}_{,\beta} + \boldsymbol{\phi}_{,\alpha} \cdot \delta\boldsymbol{\phi}_{,\beta}, \\ \delta\kappa_{\alpha\beta} &= \delta\boldsymbol{\phi}_{,\alpha} \cdot \mathbf{d}_{,\beta} + \boldsymbol{\phi}_{,\alpha} \cdot \delta\mathbf{d}_{,\beta}, \\ \delta\gamma_\alpha &= \delta\boldsymbol{\phi}_{,\alpha} \cdot \mathbf{d} + \boldsymbol{\phi}_{,\alpha} \cdot \delta\mathbf{d}.\end{aligned}\tag{2.49}$$

The weak form can also be written as

$$\int_{\mathcal{A}_R} J \left[\frac{1}{2} \tilde{t}^{\alpha\beta} \delta a_{\alpha\beta} + \tilde{m}^{\alpha\beta} \delta \kappa_{\alpha\beta} + \tilde{q}^\alpha \delta \gamma_\alpha \right] d\mu - G_{ext}(\delta \boldsymbol{\psi}) = 0. \quad (2.50)$$

The derivation from Eq. (2.38) to Eq. (2.50) is described in [69].

2.3 Inverse elastostatic method

Inverse elastostatic stress analysis is a method for solving the equilibrium problem of an elastic material body. It takes the deformed geometry and the corresponding load as input and pursues the stress-free configuration. The inverse elastostatics method belongs to the family of inverse methods that seek the initial data of boundary value problems. There are a number of ways to formulate inverse problem for elastic systems; the one that is followed in this and preceding work in our group originated from the work by Govindjee et al. [18, 19, 39]. Govindjee's idea hinges on the fact that the stress in an elastic body depends on the local relative deformation from the reference to the current configuration. If one of these configurations is given, the other can be found from equilibrium assuming that the applied load and material constitutive equations are known. Govindjee also introduced a finite element formulation which differs minimally from the forward code. The difference lies in the use of constitutive relations and the solution paradigm. In the forward approach, the constitutive equation is given in terms of the strain measures in the forward motion. In contrast, the constitutive equation in the inverse approach is represented in terms of the strain measures of the inverse motion. In the inverse formulation, the initial stress-free configuration is to be solved. Thus, in a Newton type iterative procedure,

the linearization of the weak form goes along an opposite direction of that in the forward case. While the increments of unknowns are updates to the current (deformed) configuration in the forward formulation, the increments of unknowns in the inverse formulation are the updates of the reference configuration [100]. A reparameterization of the stress functions in terms of inverse strain measures, as well as the linearization of the stress functions with respect to the referential increments, furnishes the backbone of the inverse finite element formulation.

For some membrane structures, the inverse approach has a unique advantage such that it can accurately predict the wall stress without knowing the realistic material property. This is because such a structure by itself is statically determined, or at least approximately so. By formulating equilibrium equation directly on the given deformed configuration, the material independence natural of the problem can be maximally exploited. The forward analysis, on the other hand, does not have this advantage because the deformed shape depends on the material property. The membrane inverse elastostatic method is the backbone of PWIM. We use the inverse method to predict the stress distributions at deformed configurations, thus forming the pointwise stress-strain data basis necessary for describing the local property of the material.

Although the inverse method possesses this remarkable advantage, the inverse membrane model has several limitations. Membranes cannot sustain a compressive stress or undergo motions that revert the surface curvature. As such, the inverse membrane method cannot be used on the flat or concave regions. This is the major

issue that the present work aims to address.

In the next section we will introduce the inverse shell theory which can eliminate the geometry limitation.

2.3.1 Inverse shell formulations

In the inverse shell theory, the weak form also takes the Eq. (2.50).

$$\int_{\mathcal{A}_{\mathcal{R}}} J \left[\frac{1}{2} \tilde{t}^{\alpha\beta} \delta a_{\alpha\beta} + \tilde{m}^{\alpha\beta} \delta \kappa_{\alpha\beta} + \tilde{q}^{\alpha} \delta \gamma_{\alpha} \right] d\mu - G_{ext}(\delta \boldsymbol{\psi}) = 0. \quad (2.51)$$

In the inverse shell analysis, the input data are the current (deformed) configuration of the middle surface, the current director field, the loads applied on the current configuration, and boundary conditions. The inverse problem can be stated as: given a deformed configuration \mathcal{C} , and corresponding external loads and boundary conditions on \mathcal{C} , find the initial configuration \mathcal{R} so that the equilibrium equation is satisfied.

Since the current configuration is given, it makes sense to write the weak form in terms of the current configuration

$$\int_{\mathcal{A}_{\mathcal{C}}} \left[\frac{1}{2} \tilde{t}^{\alpha\beta} \delta a_{\alpha\beta} + \tilde{m}^{\alpha\beta} \delta \kappa_{\alpha\beta} + \tilde{q}^{\alpha} \delta \gamma_{\alpha} \right] d\mu - G_{ext}(\delta \boldsymbol{\psi}) = 0, \quad (2.52)$$

where $\mathcal{A}_{\mathcal{C}}$ is the current surface area, $d\mu = \|\mathbf{a}_1 \times \mathbf{a}_2\| d\xi^1 d\xi^2$ is the current area element, and $G_{ext}(\delta \boldsymbol{\psi})$ is the virtual work done by external force and moment [102].

Opposite to the forward analysis, the kinetic variables $(\tilde{t}^{\alpha\beta}, \tilde{m}^{\alpha\beta}, \tilde{q}^{\alpha})$ are regarded as the functions of the referential strain measures $(A_{\alpha\beta}, K_{\alpha\beta}, \Gamma_{\alpha})$. Here we use the membrane stress strain relation as an example to illustrate this set up. It could

be described as $d\mathbf{t} = \mathbf{D}_t d\mathbf{A}$, \mathbf{D}_t represents the material tensor. If we write \mathbf{D}_t in the components $\mathbf{D}_t = D_t^{\alpha\beta\delta\gamma} \mathbf{a}_\alpha \otimes \mathbf{a}_\beta \otimes \mathbf{A}_\delta \otimes \mathbf{A}_\gamma$, we can have

$$\begin{aligned} D_t^{\alpha\beta\delta\gamma} &= 2 \frac{\partial \tilde{\mathbf{t}}^{\alpha\beta}}{\partial A_{\delta\gamma}} = 2 \frac{\partial (J^{-1} \tilde{T}_s^{\alpha\beta})}{\partial A_{\delta\gamma}} = 4 \frac{\partial (J^{-1} \frac{\partial w}{\partial a_{\alpha\beta}})}{\partial A_{\delta\gamma}} \\ &= 4 [J^{-1} \frac{\partial^2 w}{\partial a_{\alpha\beta} \partial A_{\delta\gamma}} + \frac{1}{2} T_s^{\alpha\beta} \frac{J^{-1}}{\partial A_{\delta\gamma}}] = 4 J^{-1} \frac{\partial^2 w}{\partial a_{\alpha\beta} \partial A_{\delta\gamma}} + J^{-1} T_s^{\alpha\beta} A^{\delta\gamma}, \end{aligned} \quad (2.53)$$

in which, $\frac{\partial J^{-1}}{\partial A_{\delta\gamma}} = \frac{\partial (\frac{\det A_{\delta\gamma}}{\det a_{\delta\gamma}})}{\partial A_{\delta\gamma}} = J^{-1} A^{\delta\gamma}$.

Similarly, the material tensor for bending moment and transverse shear can be computed. The exclusive inverse shell formulations can be found in [101], the details are omitted here.

2.4 Pointwise identification method (PWIM)

The basic procedure of PWIM is showed in Figure (2.3). The essential characteristic of this method is that stress and strain data are acquired separately and obtained simultaneously at infinitely many points. Strain distributions are derived from surface deformation. The stresses are computed with the inverse membrane method in each configuration. At each Gauss point, we can get the multiple strain-stress data, by which we can examine the elastic behavior of the material. Fitting the pointwise stress-strain data at a point to an appropriate constitutive equation gives the material properties at that point.

There are three major steps in PWIM: stress acquisition, strain acquisition, and elastic parameter regression.

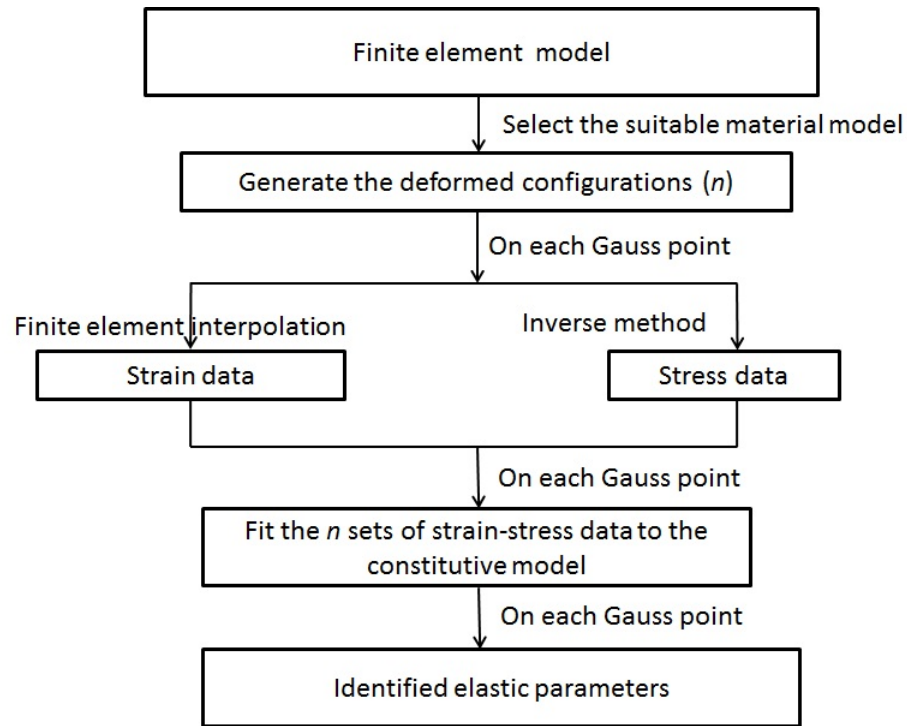


Figure 2.3: Basic procedure of PWIM.

2.4.1 Stress acquisition

The stress in the corresponding deformed configuration can be computed using the inverse method. The underlying promise is that, the structure of interest is at least approximately statically determined, and thus, in the inverse paradigm one can compute the stress using assumed material properties with the expectation that the stress so computed is a good approximation of the true stress in the structure.

2.4.2 Stain acquisition and computation

In general, strains are derived from the deformation field of the surface. If we assume that the surface is parameterized as a finite element mesh, then we have

$$\mathbf{X} = \sum_{I=1}^{Nel} N_I(\xi^1, \xi^2) \mathbf{X}^I, \quad \mathbf{x} = \sum_{I=1}^{Nel} N_I(\xi^1, \xi^2) \mathbf{x}^I, \quad (2.54)$$

where the superscript I means the nodal number, Nel is the total number of nodes in each element, and $N_I(\xi^1, \xi^2)$ represents the shape function. We use natural coordinates (ξ^1, ξ^2) to present the (element-wise) convected surface coordinates. The convected base vector in the deformed (\mathbf{a}_α) and reference (\mathbf{A}_α) configuration can be calculated, respectively, as

$$\mathbf{a}_\alpha = \frac{\partial \mathbf{x}}{\partial \xi^\alpha} = \sum_{I=1}^{Nel} \frac{\partial N_I}{\partial \xi^\alpha} \mathbf{x}^I, \quad \mathbf{A}_\alpha = \frac{\partial \mathbf{X}}{\partial \xi^\alpha} = \sum_{I=1}^{Nel} \frac{\partial N_I}{\partial \xi^\alpha} \mathbf{X}^I. \quad (2.55)$$

So the components of the covariant metric tensor of the deformed and undeformed configuration can be calculated using

$$\begin{aligned} a_{\alpha\beta} &= \mathbf{a}_\alpha \cdot \mathbf{a}_\beta = \sum_{I=1}^{Nel} \sum_{J=1}^{Nel} \frac{\partial N_I}{\partial \xi^\alpha} \frac{\partial N_J}{\partial \xi^\beta} \mathbf{x}^I \mathbf{x}^J, \\ G_{\alpha\beta} &= \mathbf{A}_\alpha \cdot \mathbf{A}_\beta = \sum_{I=1}^{Nel} \sum_{J=1}^{Nel} \frac{\partial N_I}{\partial \xi^\alpha} \frac{\partial N_J}{\partial \xi^\beta} \mathbf{X}^I \mathbf{X}^J. \end{aligned} \quad (2.56)$$

The dual basis vectors are computed using the formula shown in Eq. (2.3). Therefore, we can express the membrane strain invariants in tensorially invariant as shown in the example in Eq. (2.22) and Eq. (2.23).

2.4.3 Parameter identification

Imagine that the stress-strain fields in a number of deformed configuration are obtained so that at every Gauss points we have a stress-strain database. We would

like to fit the stress-strain data to a constitutive equation. Using the convected components $a_{\alpha\beta}$ obtained from strain acquisition, with an appropriate constitutive model, we can calculate the resultant \mathbf{t} as a function of metric tensor and elastic parameters (assumed). We can formulate a regression problem minimizing the computed stress resultant (“experimental stress resultant”) ${}^{(i)}\widehat{\mathbf{t}}$ and the modeled stress resultant ${}^{(i)}\mathbf{t}$. Then, a regression algorithm is applied to identify the elastic parameters. We use SNOPT, a nonlinear regression program [17], to perform parameter regression. SNOPT requires the user to provide an objective function, which represents the discrepancy between the numerically modeled and experimentally measured material responses. There are many ways to construct the objective function, i.e., the stress components, stress invariants, and principal stresses [99]. In the PWIM in [47, 96], the weighted objective function is set to be

$$\Phi = \sum_{i=1}^N \left\| {}^{(i)}\mathbf{t} - {}^{(i)}\widehat{\mathbf{t}} \right\|_w^2 = \sum_{i=1}^N [\mathbf{w}({}^{(i)}\mathbf{t} - {}^{(i)}\widehat{\mathbf{t}})] \cdot ({}^{(i)}\mathbf{t} - {}^{(i)}\widehat{\mathbf{t}}). \quad (2.57)$$

where \mathbf{w} is the diagonal matrix of weights $\mathbf{w} = \begin{bmatrix} w_1 & 0 & 0 \\ 0 & w_2 & 0 \\ 0 & 0 & w_3 \end{bmatrix}$. Φ here is a function of elastic parameters only.

CHAPTER 3

SENSITIVITY OF STRESS TO MATERIAL MODEL IN INVERSE & FORWARD ANALYSIS OF THIN STRUCTURES

This chapter investigates the sensitivity of stress solutions to material models in the inverse and forward stress analysis in the context shell structures. We assume that the bending stress also will be affected by the geometry in shell structure and less bending will lead a better material insensitivity property. We investigate how the geometries affect the stress insensitivity here. The geometry contains several aspects, like thickness and topology (surface geometry). In this chapter, we mainly evaluate the effects of topology on inverse stress by using three realistic aneurysm structures. In this work two patient-specific AAAs, twenty six human cerebral aneurysms are used to investigate the effects of topology on the inverse stress insensitivity. In this study, the AAAs represent the tubular geometrical models and cerebral aneurysms are saccular geometrical examples.

3.1 Tubular geometry - AAA

Abdominal aortic aneurysms (AAAs) represent permanent localized expansions of the aorta that form between the renal arteries and the iliac bifurcation. AAA is a common vascular problem with fatal implications and has been an focal point of interest for biomedical studies [67].

In this work, we use two patient-specific AAA models, a juvenile AAA and a full grown AAA. The two patient-specific AAAs represent the tubular and mixed

tubular-saccular geometry, respectively. These two models are expected to have different magnitude of bending stress in their response. We assume that with more bending stress, the stress insensitivity maybe compromised. In the second part of this work, we compared the effects of bending stresses on the stress insensitivity.

3.1.1 FEA models shell

The juvenile AAA and full grown AAA are both patient-specific models. The imaged morphology of the AAA is assumed to be taken as deformed configuration under 100 mmHg pressure. Because the fluid shear stress is much smaller than the wall stress caused by the pressure, in this work, for all the cases, we exclude the fluid shear stress. For each AAA, the thickness is taken to be 1.9 mm uniformly. For the boundary condition, the edges of the vasculature are fixed.

3.1.2 Material model

To numerically access the influence of material parameters, we carry out the inverse analysis for two families of material models (Fung model and neo-Hookean model). Within each material model, the elasticity parameters are varied to yield for sub-models. For comparison, we also conduct the corresponding forward analysis. The stress results are compared within each family and cross families as well. The baseline model for the first family is the anisotropic Fung model used in [102]. The Fung model's energy function assumes the form

$$\begin{aligned}\psi_m &= c(e^Q - 1), \\ Q &= d_1 E_{11}^2 + d_2 E_{22}^2 + 2d_3 E_{11} E_{22} + d_4 E_{12}^2.\end{aligned}\tag{3.1}$$

In this equation, c, d_1, d_2, d_3, d_4 are material parameters and are set as $c = 0.16N/mm$, $d_1 = 14.89$, $d_2 = 15.20$, $d_3 = 7.57$, $d_4 = 4.96$. The sub-model in this family is generated by magnifying the stiffness parameter c by 10 times. To contrast with the neo-Hookean model, we set the Fung model here as anisotropic.

The second family is modeled by the neo-Hookean material, which is an isotropic hyperelastic material. The model is specified by the strain-energy function

$$W = \alpha(I_1 - 2\log J - 2) + \beta(I_1 - 2)^2, \quad (3.2)$$

where W is the strain-energy density, $I_1 = \text{tr}(\mathbf{F}^T \mathbf{F})$, $J = \det \mathbf{F}$, and α, β are material constants.

We set the material with the population mean material parameters $\alpha = 0.174N/mm^2$, $\beta = 0.188N/mm^2$ [52, 50]. The sub-model in this family is generated by magnifying the stiffness parameter α by 10 times.

3.1.3 Results

3.1.3.1 Juvenile AAA

Deformed configuration calculated using the forward method with the baseline Fung material model is compared to the one obtained with the baseline neo-Hookean material. Figure 3.1 shows the differences of deformed configurations computed with the two baseline material models. The initial configuration predicted using the inverse method with the baseline Fung material model is compared to the one obtained with the baseline neo-Hookean material in Figure 3.2. We can find that the initial configurations predicted by the inverse method are distinctly different for two material

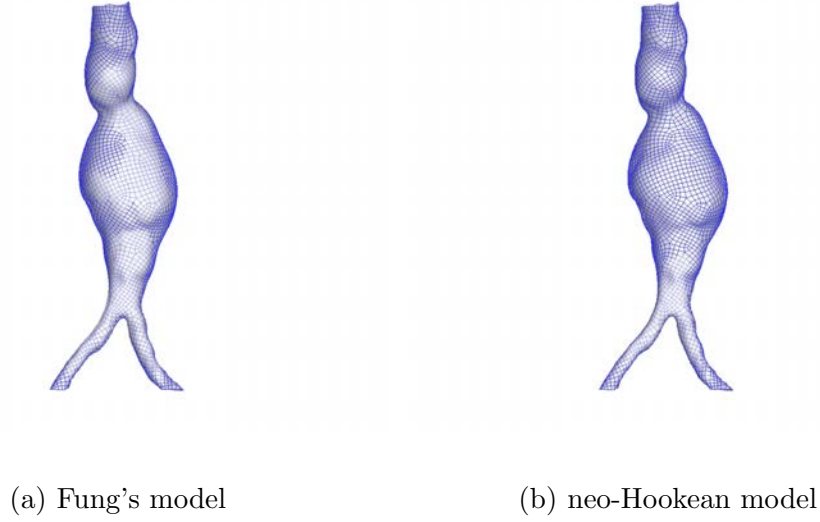


Figure 3.1: Deformed shape (mesh) vs. *in vivo* shape (shaded) using conventional forward shell method: (a) Fung's model with baseline material parameters; (b) neo-Hookean model with baseline material parameters.

models.

The Von Mises stress results of Fung model using the forward and inverse method respectively in Figure 3.3. From the stress distributions (in Figure 3.3(a) and Figure 3.3(b)) are slightly different between two Fung models by using forward method, while in the inverse method, the stresses (in Figure 3.3(d) and Figure 3.3(e)) present similar distributaries. Corresponding with Figure 3.3 comparison, in Figure 3.4, which presents the Von Mises stress results of neo-Hookean model using the forward and inverse method respectively, the stresses computed with inverse method also present close distribution. Stress is plotted in the deformed configuration; but the meaning of deformed configuration differs in forward and inverse analysis: in

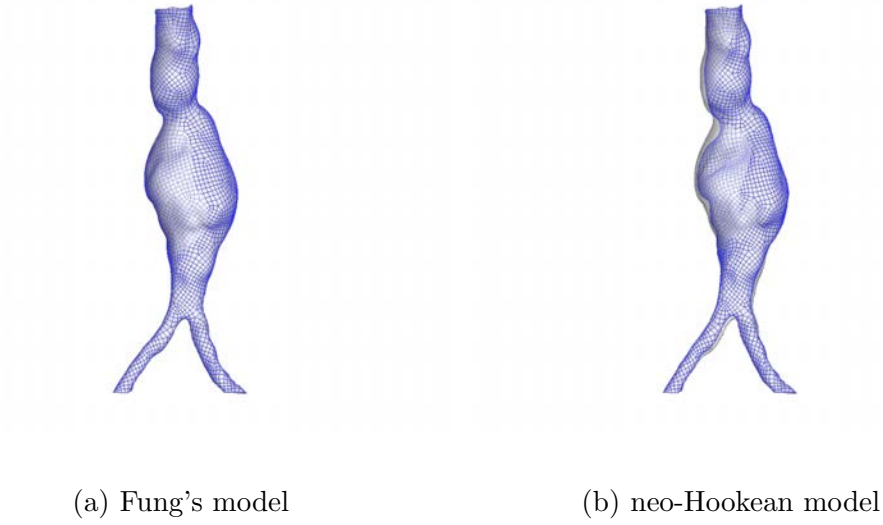


Figure 3.2: Initial (Stress free) shape (mesh) vs. *in vivo* shape (shaded) using inverse shell method: (a) Fung's model with baseline material parameters; (b) neo-Hookean model with baseline material parameters.

forward method, we used the deformed shape; it is the configuration obtained from the analysis upon applying the pressure to the imaged geometry while in the inverse analysis it is the imaged *in vivo* geometry. The unit of stress is N/mm^2 . From Figure 3.3 and Figure 3.4, we can find that the maximum stresses are all around $0.12N/mm^2$ by using inverse method with four material models, while the forward method provided different stress distribution by using four material models.

Figure 3.3(c) shows the percentage stress differences between Fung model with baseline and elevated stiffness parameters (defined as $differ = \frac{|\sigma_{baseline} - \sigma_{stiffer}|}{|\sigma_{baseline}|} \times 100\%$), using forward method. Contrast to Figure 3.3(c), Figure 3.3(f) is the percentage stress differences between the baseline and the stiffer Fung material model

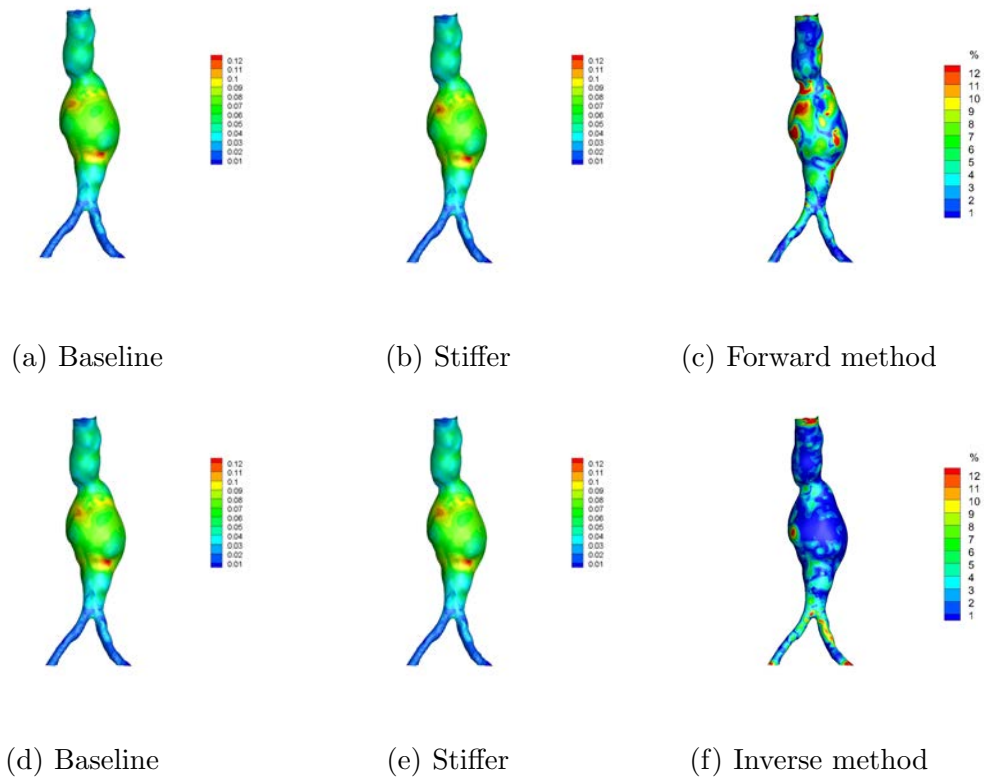


Figure 3.3: Comparison of von Mises stress predicted using the Fung family. First row: forward method. (a) Baseline; (b) Stiffer; (c) Percentage differences. Second row: inverse method. (d) Baseline; (e) Stiffer; (f) Percentage differences.

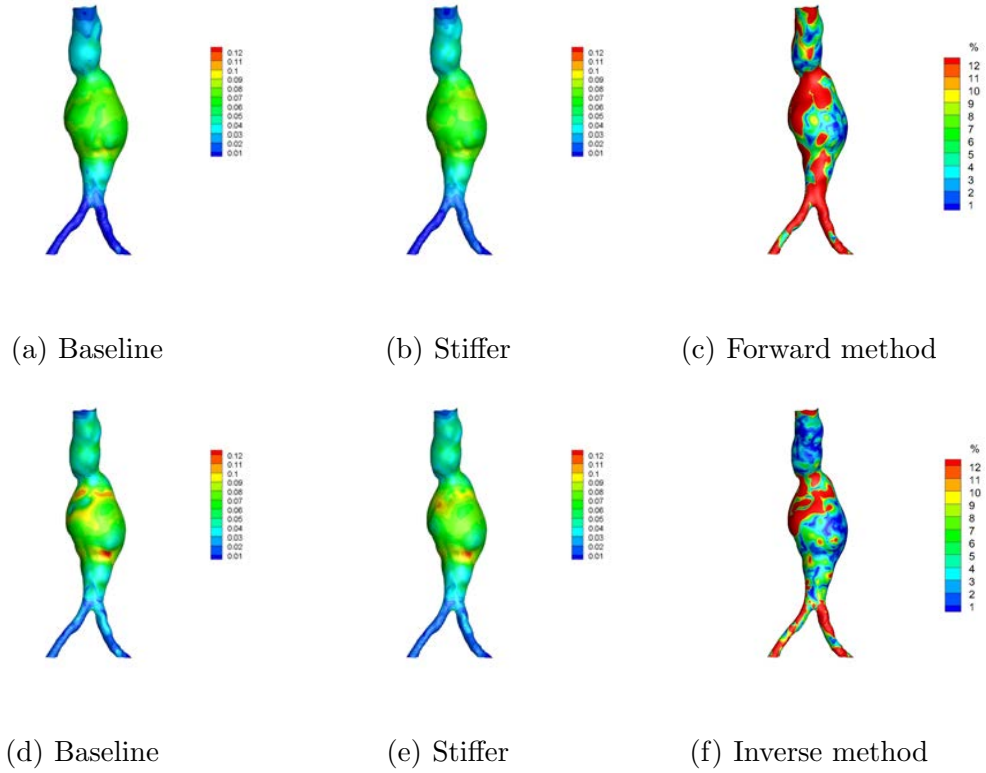


Figure 3.4: Comparison of von Mises stress predicted using the neo-Hookean family.

First row: forward method. (a) Baseline; (b) Stiffer; (c) Percentage differences.

Second row: inverse method. (d) Baseline; (e) Stiffer; (f) Percentage differences.

in inverse analysis. Figure 3.4(c) presents the percentage stress differences between the baseline neo-Hookean model and the stiffer neo-Hookean material model in forward method, and Figure 3.4(f) shows the percentage stress differences between the baseline and the stiffer neo-Hookean material model in inverse analysis. From the comparison between Figure 3.3(c) and Figure 3.3(f), (or Figure 3.4(c) and Figure 3.4(f)), it is obvious that, the stress differences computed through inverse method are much smaller than through forward method. This means that the inverse method can provide more reliable stress results.

Figure 3.3(d) and Figure 3.3(e) show the results for Fung's material model with baseline parameters and elevated stiffness parameters respectively. Figure 3.4(d) and Figure 3.4(d) show the results for neo-Hookean material model with baseline parameters and elevated stiffness parameters respectively. In Figure 3.3 and Figure 3.4, we can find that the maximum stresses computed by two different families of material models are close, around $0.12N/mm^2$. Figure 3.3(f) presents the percentage stress differences between the baseline and the stiffer neo-Hookean material model in inverse analysis. Figure 3.4(f) presents the percentage stress differences between the baseline and the stiffer neo-Hookean material model in inverse analysis.

From the comparison between Figure 3.3(c) and Figure 3.3(f), (or Figure 3.4(c) and Figure 3.4(f)), it is obvious that, the stress differences computed through inverse method are much smaller than through forward method. This means that the inverse method can provide more reliable stress results. Figure 3.5 presents the percentage stress differences between the baseline Fung model and the baseline neo-Hookean

model by using inverse methods, respectively. This comparison further testifies that the inverse stress solutions are much more insensitive to material model.

We also compared the maximum stresses of four material models by using both the forward and inverse methods (Table 3.1). To avoid the peak stress caused by stress concentration, the 95% of the max von Mises stress is used in this comparison. The mean stresses obtained from the forward and inverse methods are also presented in the same table. From Table 3.1, we can find that the maximum stress predicted by the inverse method is closer than the ones calculated using the forward method, even with different material models. We use the baseline Fung’s model as reference model, and percentage difference of 95% maximum stress and mean stress between the other three material model to Fung’s model (defined as $\frac{|\sigma - \sigma_{ref}|}{\sigma_{ref}} \times 100\%$) is shown in Table 3.2. Table 3.2 shows that, although with different material models, the inverse method can provide reliable maximum stress results.

Table 3.3 shows the von Mises stress differences. From the statistic comparisons, one can find that the stresses calculated by using the inverse method are more insensitive to material models. In all the tables, we use “Fung” to present Fung material model, and “Neoh” to present the neo-Hookean material model.

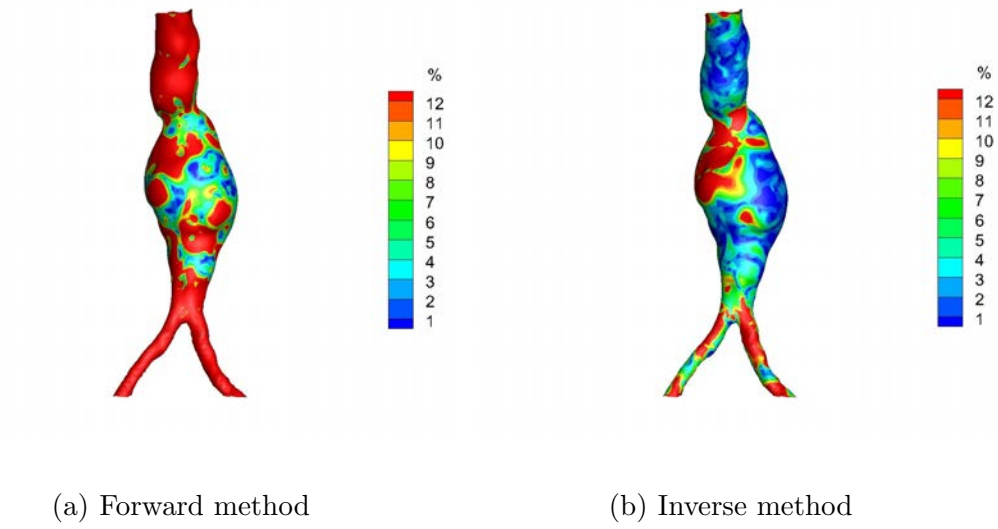


Figure 3.5: Percentage stress differences between the baseline Fung model and the baseline neo-Hookean model by using forward and inverse method, respectively: (a) forward method; (b) inverse method.

Table 3.1: Maximum stress and mean stress of four material models.

Material parameters	95% Max stress		Mean stress	
	Forward	Inverse	Forward	Inverse
Fung baseline	0.11740066	0.12108116	0.05233019	0.05208197
Fung stiffer	0.12103883	0.11877020	0.05218226	0.0520730
Neoh baseline	0.09685514	0.12854718	0.04681716	0.05258555
Neoh stiffer	0.08519402	0.11596767	0.04848080	0.05189541

Table 3.2: Percentage differences of maximum stress and mean stress relative to reference material model using the forward and inverse methods.

Material models	Differences of 95% max stress (%)		Differences of mean stress (%)	
	Forward	Inverse	Forward	Inverse
Fung baseline	-	-	-	-
Fung stiffer	3.099	1.909	0.283	0.017
Neoh baseline	17.500	6.166	10.535	0.967
Neoh stiffer	27.433	4.223	7.356	0.358

Table 3.3: Statistics of the percentage differences (%) by using forward and inverse method, respectively.

Material parameters	Minimum		Maximum		Mean	
	Forward	Inverse	Forward	Inverse	Forward	Inverse
Fung: baseline Vs. stiffer	0.013	0.0002	17.679	4.853	1.870	0.763
Neoh: baseline Vs.stiffer	0.539	0.028	20.673	16.868	10.746	7.363
Baseline: Fung Vs. Neoh	0.843	0.025	87.164	17.953	38.422	6.331

3.1.3.2 Full grown AAA

Deformed configuration calculated using the forward method with the baseline Fung material model is compared to the one obtained with the baseline neo-Hookean material. Figure 3.6 shows the differences in deformed configuration between the two material models.

The initial configuration predicted with the baseline Fung material model is compared to the one obtained with the baseline neo-Hookean material. Figure 3.7

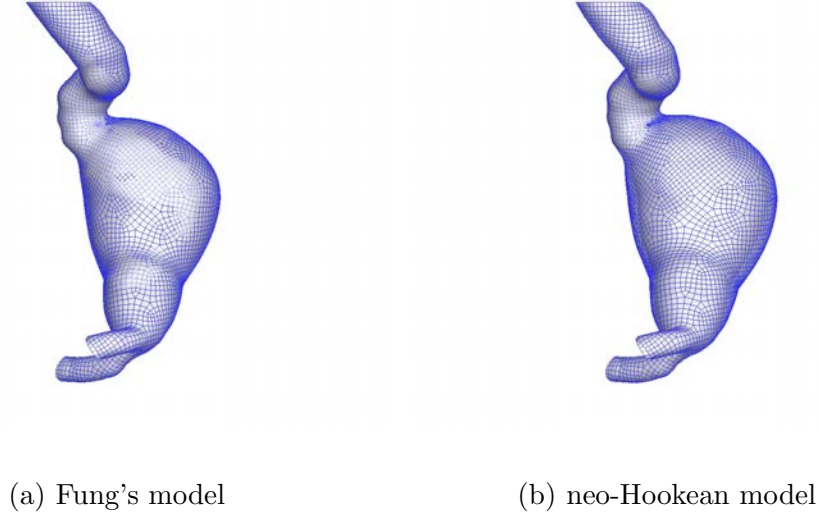


Figure 3.6: Deformed shape (mesh) vs. *in vivo* shape (shaded) using forward shell method: (a) Fung's model with baseline material parameters; (b) neo-Hookean model with baseline material parameters.

presents the comparison in deformed configuration with two material models using the inverse method.

Figure 3.8 and Figure 3.9 present the Von Mises stress results using Fung model and neo-Hookean, respectively. Figure 3.8(a) and 3.8(b) show the forward results for the Fung material model with baseline parameters and elevated stiffness parameters, respectively. Figure 3.8(d) and 3.8(e) show the inverse results for the Fung material model with baseline parameters and elevated stiffness parameters, respectively. Figure 3.9(a) and 3.9(b) show the forward results for the neo-Hookean material model with baseline parameters and elevated stiffness parameters, respectively. Figure 3.9(d) and 3.9(e) show the inverse results for the neo-Hookean material

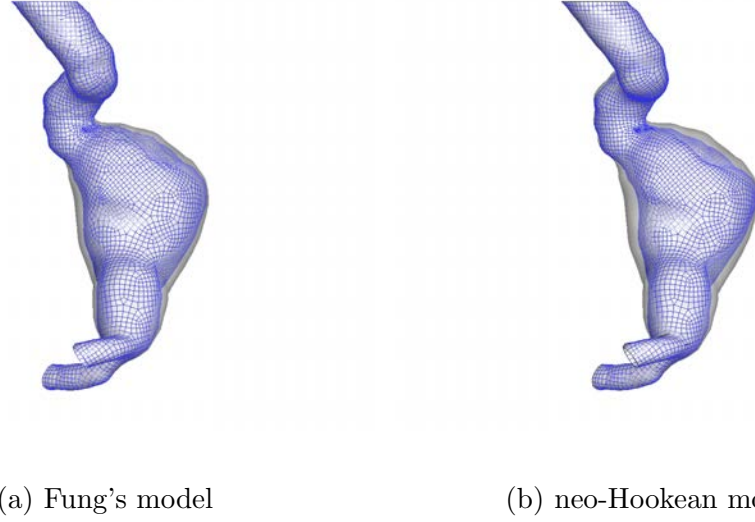


Figure 3.7: Initial (Stress free) shape (mesh) vs. *in vivo* shape (shaded) using inverse shell method: (a) Fung's model with baseline material parameters; (b) neo-Hookean model with baseline material parameters.

model with baseline parameters and elevated stiffness parameters, respectively. Figure 3.8(c) presents the percentage stress differences between Fung model with baseline and elevated stiffness parameters using forward method, and Figure 3.8(f) is the percentage stress differences between the baseline and the stiffer Fung material model in inverse analysis. Figure 3.9(c) presents the percentage stress differences between the baseline neo-Hookean model and the stiffer neo-Hookean material model in forward method, and Figure 3.9(f) presents the percentage stress differences between the baseline and the stiffer neo-Hookean material model in inverse analysis. In Figure 3.8(c) and Figure 3.8(f), the differences by using Fung material model in most regions are around 9% and 4% for forward method and inverse method, respectively. In Figure

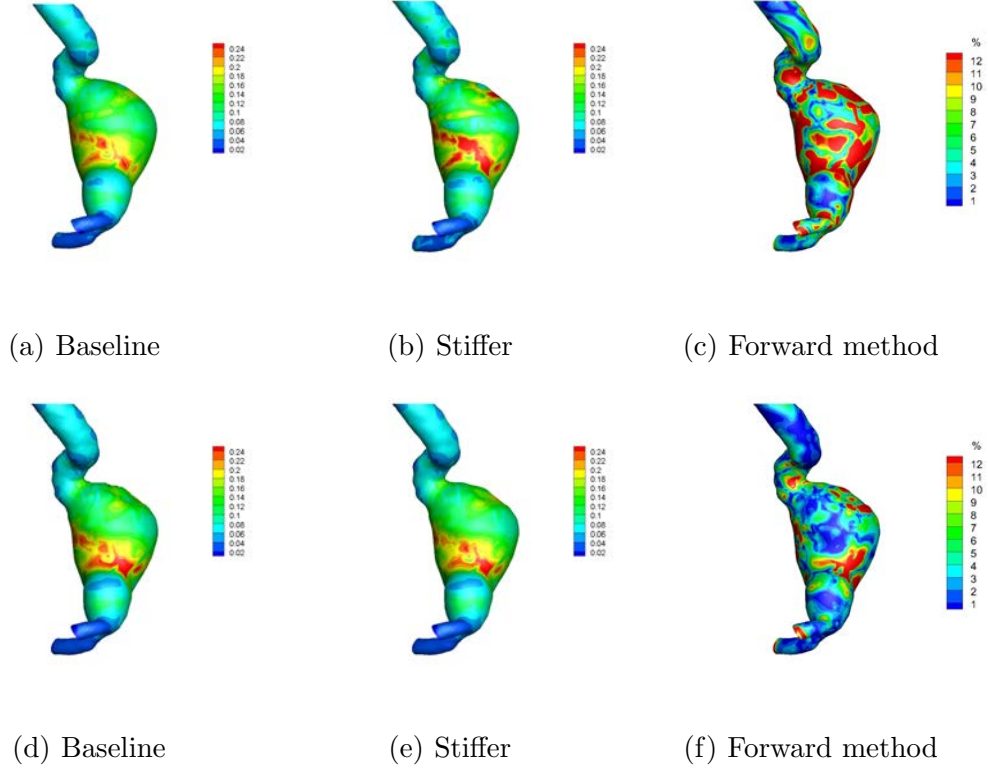


Figure 3.8: Von Mises stress results using the Fung models. First row: forward method. (a) Baseline; (b) Stiffer; (c) Percentage difference. Second row: forward method. (d) Baseline; (e) Stiffer; (f) Percentage difference.

3.9(c) and Figure 3.9(f)), for the neo-Hookean material model, it is more obvious that the stress differences computed through inverse method are much smaller than through forward method.

The percentage stress differences between the baseline Fung model and the baseline neo-Hookean model by using the forward and inverse methods respectively in Figure 3.10. We can find that even across the material model, the stress differences are quite small using the inverse shell method.

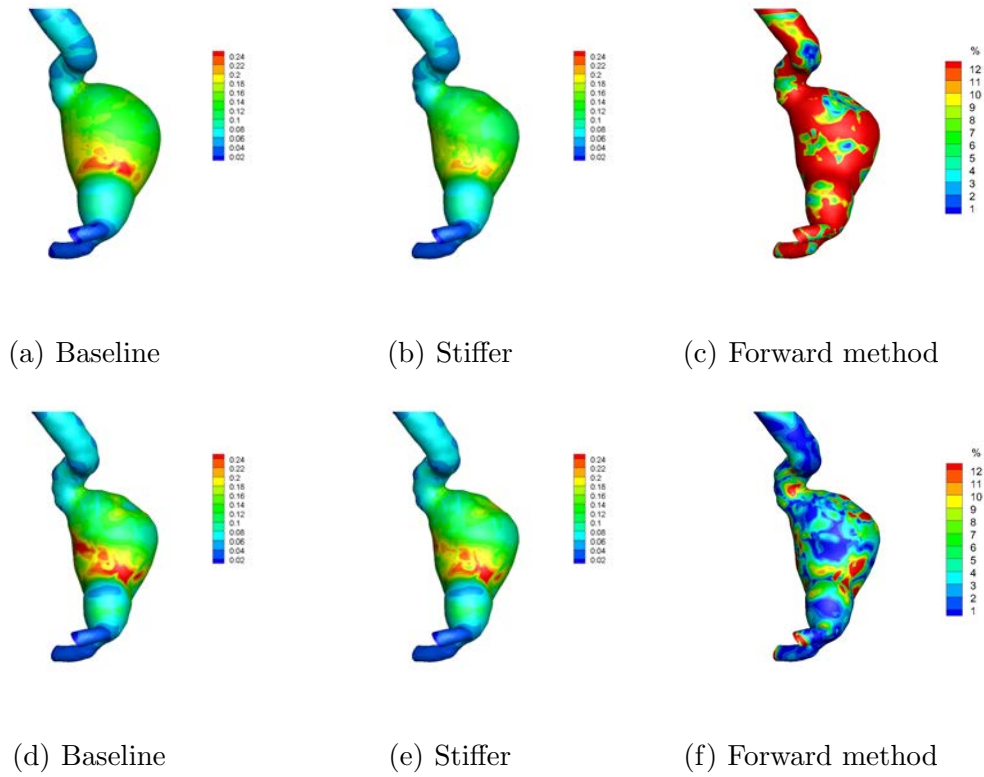


Figure 3.9: Von Mises stress results using the neo-Hookean models. First row: forward method. (a) Baseline; (b) Stiffer; (c) Percentage difference. Second row: forward method. (d) Baseline; (e) Stiffer; (f) Percentage difference.

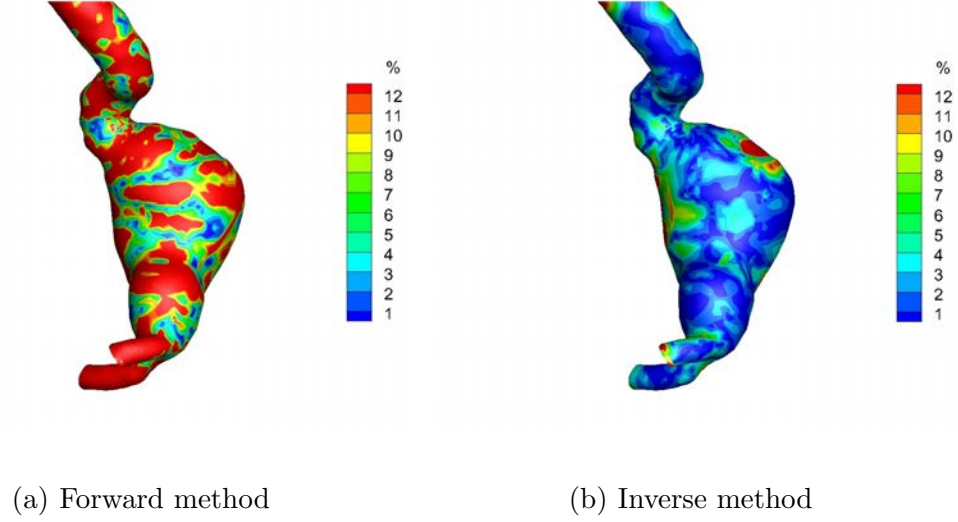


Figure 3.10: Percentage stress differences between the baseline Fung model and the baseline neo-Hookean model by using forward and inverse method respectively: (a) forward method; (b) inverse method.

In addition, we also compared the maximum stresses of four material models by using both the forward and inverse methods (Table 3.4). To avoid the peak stress caused by stress concentration, we used the 95% of the max von Mises stress. We also compared the mean stresses obtained from the forward and inverse methods in the same table. From Table 3.4, we can find that the maximum stresses predicted by the inverse method are closer than the ones calculated using the forward method, even with different material models. We use the baseline Fung's model as reference model, and percentage difference of 95% maximum stress and mean stress between the other three material model to Fung's model (defined as $\frac{|\sigma - \sigma_{ref}|}{\sigma_{ref}} \times 100\%$) is shown in Table 3.5.

Table 3.4: Maximum stress and mean stress of four material models.

Material models	95% Max stress		Mean stress	
	Forward	Inverse	Forward	Inverse
Fung baseline	0.237622550	0.28871165	0.10292982	0.10297089
Fung stiffer	0.30959170	0.27297300	0.10866620	0.10237333
Neoh baseline	0.249719850	0.28544460	0.10553018	0.10369119
Neoh stiffer	0.215419150	0.27019140	0.09775672	0.10202119

Table 3.5: Percentage differences of maximum stress and mean stress relative to reference material model using the forward and inverse methods.

Material models	Differences of 95% max stress (%)		Differences of mean stress (%)	
	Forward	Inverse	Forward	Inverse
Fung baseline	-	-	-	-
Fung stiffer	30.287	5.451	5.573	0.580
Neoh baseline	5.091	1.131	2.526	0.670
Neoh stiffer	9.344	6.414	5.026	0.922

Table 3.6 shows the von Mises stress differences. Similar with the results in the juvenile AAA model, the stresses computed by inverse method are more material insensitive.

Table 3.6: Statistics of the percentage differences (%) by using forward and inverse method, respectively.

Material parameters	Minimum		Maximum		Mean	
	Forward	Inverse	Forward	Inverse	Forward	Inverse
Fung: baseline Vs. stiffer	0.931	0.004	35.467	17.682	10.807	3.834
Neoh: baseline Vs.stiffer	1.021	0.076	35.495	14.265	9.208	5.996
Baseline: Fung Vs. Neoh	1.573	0.031	69.544	15.164	15.102	3.519

3.1.4 Bending effects on material sensitivity

In last section, we compare the stress differences. The von Mises stresses discussed in the last section are the membrane stress. In this part, we will investigate the affection of bending components on stress insensitivity. To evaluate the extent to which the bending components affect the stress insensitivity to material, we set a bending stress factor of $\alpha = \frac{\text{bendingstress}}{\text{membranestress} \times \text{shellthickness}}$. Figure 3.11(a) and Figure 3.11(b) show the distribution of α of juvenile and full grown AAA, respectively. Both of them are computed through inverse baseline Fung material model. The bending factors also have the same order of magnitude with other neo-Hookean material model for the juvenile and the full grown AAA, respectively.

In the Figure 3.11, it is shown that the bending stress in some regions are relative big compare to the membrane stress, for both AAA models. Some regions, the bending stress are even bigger than the in-plane stress. So in this case when the bending can not be omitted, we study the von-Mises stress taking the bending stress component into consideration. Here the we use $(\sigma'_{xx}, \sigma'_{yy}, \sigma'_{xy})$ to represent the

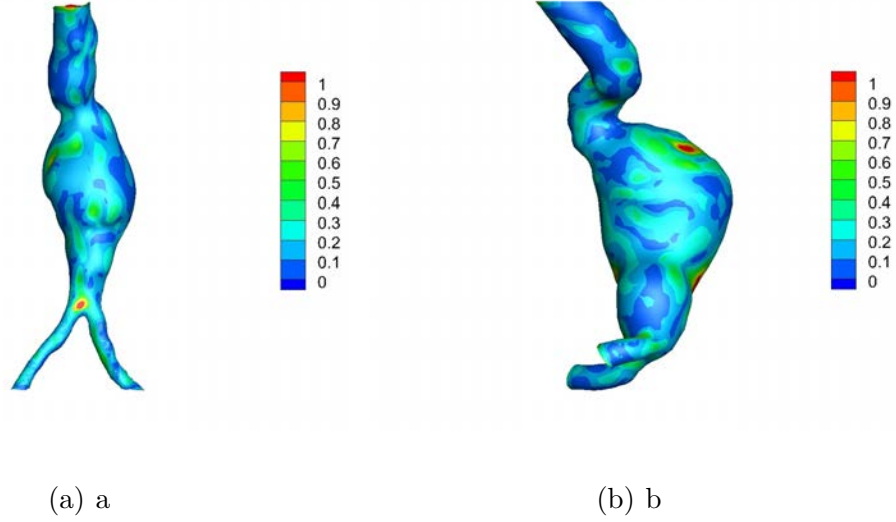


Figure 3.11: Bending factor distribution of the baseline Fung model: (a) juvenile AAA model; (b) full grown AAA model.

laminar stress computed from the following equations

$$\sigma'_{xx} = \sigma_{xx} + \frac{M_{yy}}{I}t, \quad \sigma'_{yy} = \sigma_{yy} + \frac{M_{xx}}{I}t, \quad \sigma'_{xy} = \sigma_{xy} + \frac{M_{xy}}{I}t, \quad t \in \left[-\frac{h}{2}, \frac{h}{2}\right], \quad I = \frac{h^3}{12}. \quad (3.3)$$

These are the equations for stress distribution in linear shell theory. For nonlinear material the stress no longer varies linearly across the thickness; however, the linear distributing provides a reasonable approximation. Here we take upper surface ($t = \frac{h}{2}$) where the bending maximally effects the in-plane stress. The new von Mises stress differences in terms of the upper surface stress is compared in Figure 3.12 and Figure 3.13 for juvenile AAA and full grown AAA, respectively. In Table 3.7 and Table 3.8, the mean differences are also presented. Like the membrane stress results, the inverse method remains less sensitive to material models.

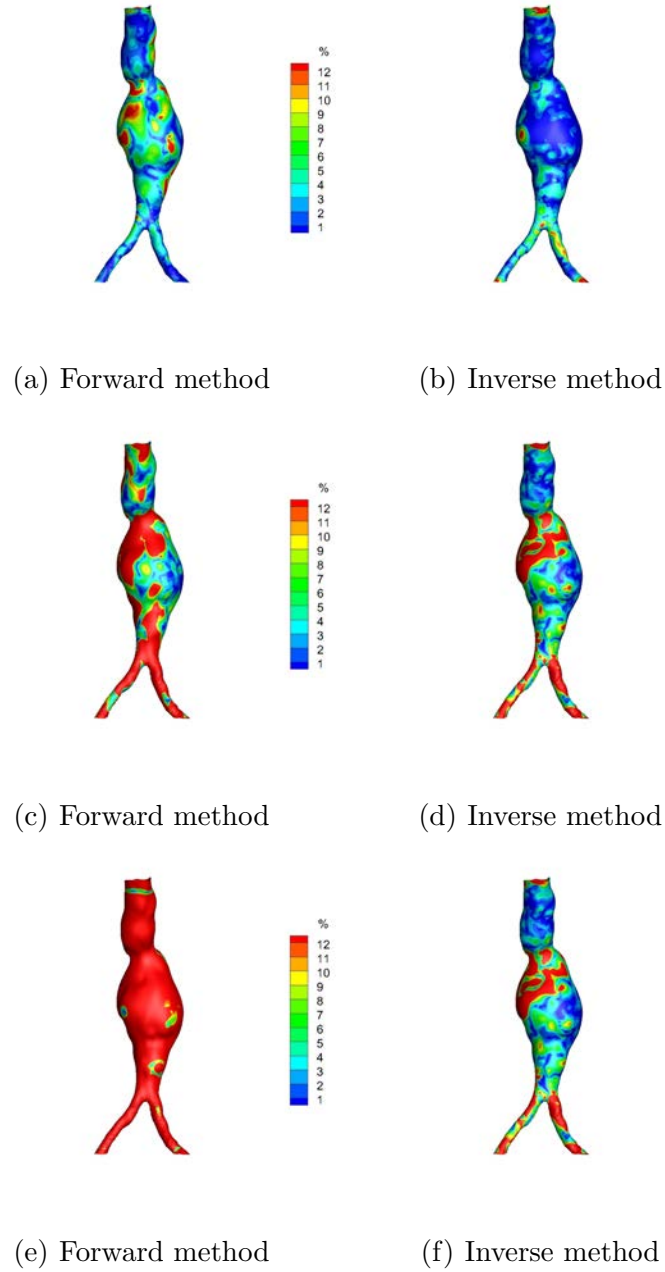


Figure 3.12: Percentage stress differences between of the juvenile AAA by using forward and inverse method respectively: (a) & (b) stress differences between baseline Fung with stiffer Fung material model; (c) & (d) stress differences between baseline neo-Hookean with stiffer neo-Hookean material model; (e) & (f) stress differences between baseline Fung model with baseline neo-Hookean model.

Table 3.7: Statistics of the percentage differences (%) in the juvenile AAA by using forward and inverse method, respectively.

Material parameters	Minimum		Maximum		Mean	
	Forward	Inverse	Forward	Inverse	Forward	Inverse
Fung: baseline Vs. stiffer	0.13	0.001	23.821	12.265	3.453	2.146
Neoh: baseline Vs.stiffer	1.529	0.089	39.552	17.598	13.422	7.119
Baseline: Fung Vs. Neoh	5.635	0.071	90.662	18.522	32.457	5.814

Table 3.8: Statistics of the percentage differences (%) in the full grown AAA by using forward and inverse method, respectively.

Material parameters	Minimum		Maximum		Mean	
	Forward	Inverse	Forward	Inverse	Forward	Inverse
Fung: baseline Vs. stiffer	1.553	0.006	35.162	15.516	9.215	3.463
Neoh: baseline Vs.stiffer	3.772	0.003	50.773	13.795	17.847	4.570
Baseline: Fung Vs. Neoh	2.695	0.002	89.115	12.259	23.136	3.942

From all the comparison figures, we can conclude that the inverse stress predictions are indeed much less sensitive to material properties. Comparing the bending factor distribution and stress differences, it is clear they are co-related; regions of higher bending factor have bigger stress differences. This is understandable, because in the shell theory, the equilibrium equations take the form in Eq. (2.38). These stress components cannot be determined by the balance equations alone, which is different from the membrane case. There are six unknown stress components, which include

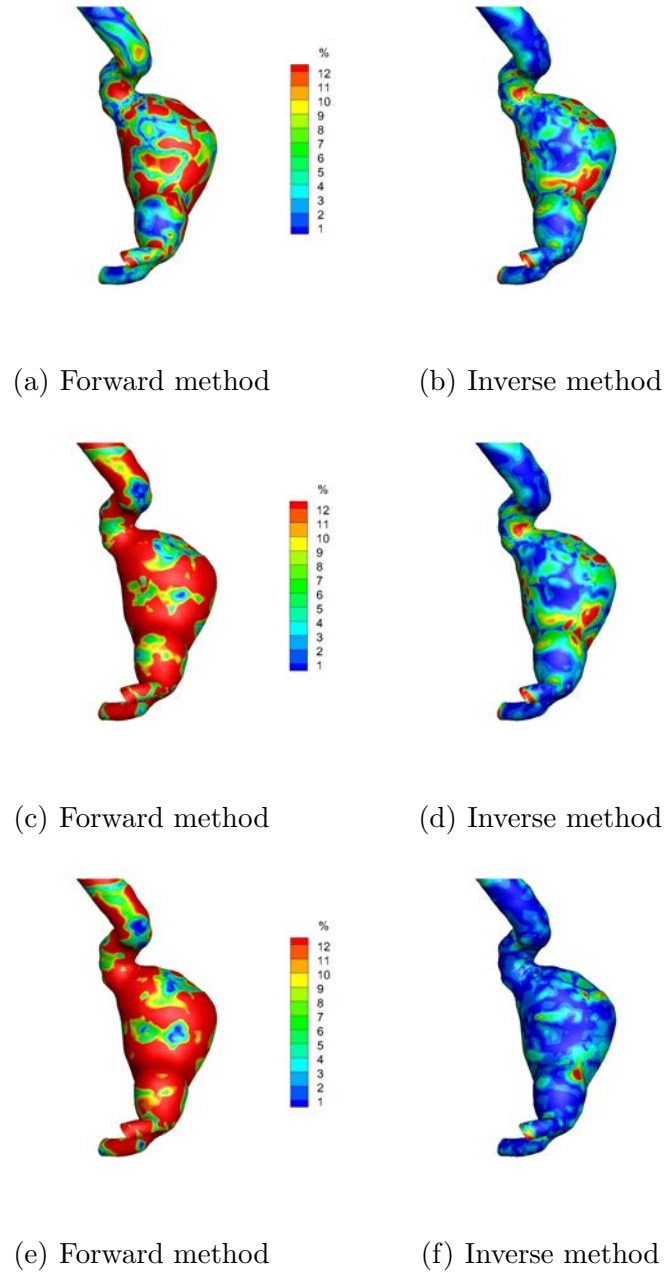


Figure 3.13: Percentage stress differences between of the full grown AAA by using forward and inverse method respectively: (a) & (b) stress differences between baseline Fung with stiffer Fung material model; (c) & (d) stress differences between baseline neo-Hookean with stiffer neo-Hookean material model; (e) & (f) stress differences between baseline Fung model with baseline neo-Hookean model.

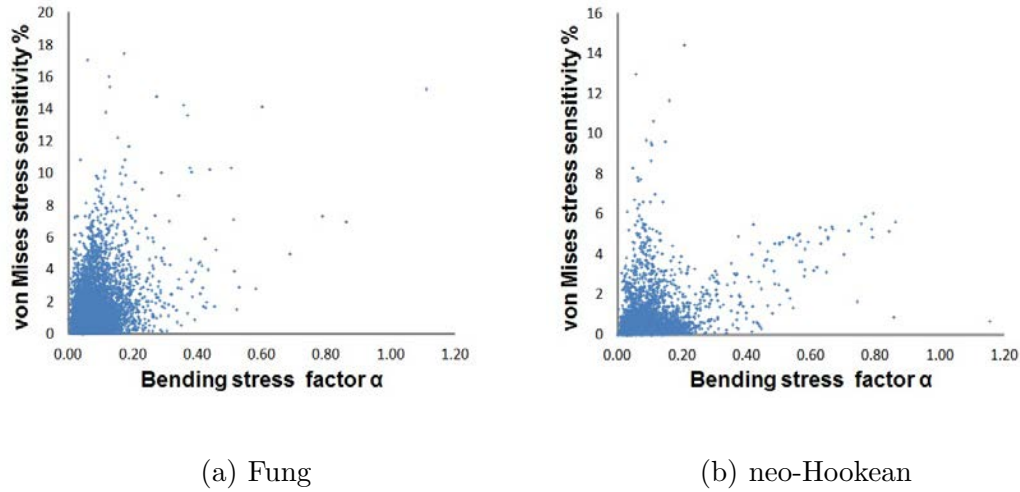


Figure 3.14: Bending factor-von Mises stress differences in the juvenile AAA using inverse method: (a) Fung material model; (b) neo-Hookean material model.

four components from the membrane resultant tensor and two components from the shear resultant; while the first equation only covers three components. So these six stress unknowns cannot be solved by the three balance equations alone; we need to introduce the material model and boundary conditions. In the both AAAs, there are spots that have higher stresses differences across material models. In these areas, the bending and transverse shear are not small compared to the membrane stresses.

To further study the bending effects on stress insensitivity, the percentage difference at every Gauss point in von Mises stress is plotted against the bending factors at the same point. Figure 3.14(a) presents results for the juvenile AAA using the inverse Fung material model. Figure 3.14(b) presents the same using the inverse neo-Hookean material model. Figure 3.15(a) and Figure 3.14(b) present the results in the grown up AAA bending using inverse fung model and inverse neo-Hookean

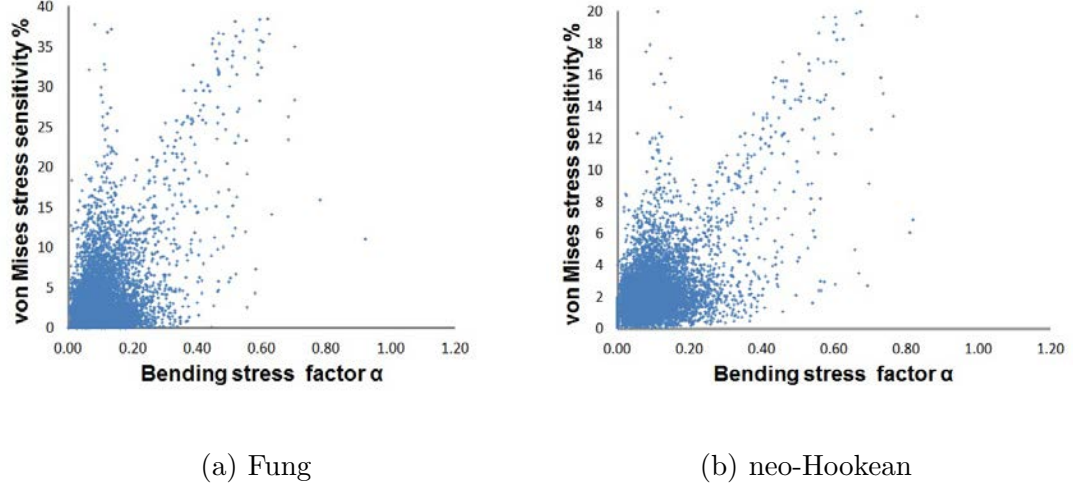


Figure 3.15: Bending factor-von Mises stress differences in the Full grown AAA using inverse method: (a) Fung material model; (b) neo-Hookean material model.

model, respectively. Except Figure 3.14(a), from the other three plots, we can find that in most points, with the increasing of bending components, the stress differences between the baseline and stiffer material models also have an increasing trend.

A comparison between deformed shapes in Figure 3.2 with Figure 3.14, and Figure 3.7 with Figure 3.15, provides some further insight on the bending effects on stress material insensitivity. Except Figure 3.14(a), the other three comparison plots have something in common: the stress sensitivity increases with the bending stress factor, which means that the bending stress affects the material insensitivity of the inverse method. There are some points with small bending stress factor and high stress sensitivity. From predicted stress-free geometries in Figure 3.2 and 3.7, we can find that, with the exception of Figure 3.2(a), the models also have a large concave regions in the predicted stress-free geometry. We locate these “edges” points in the

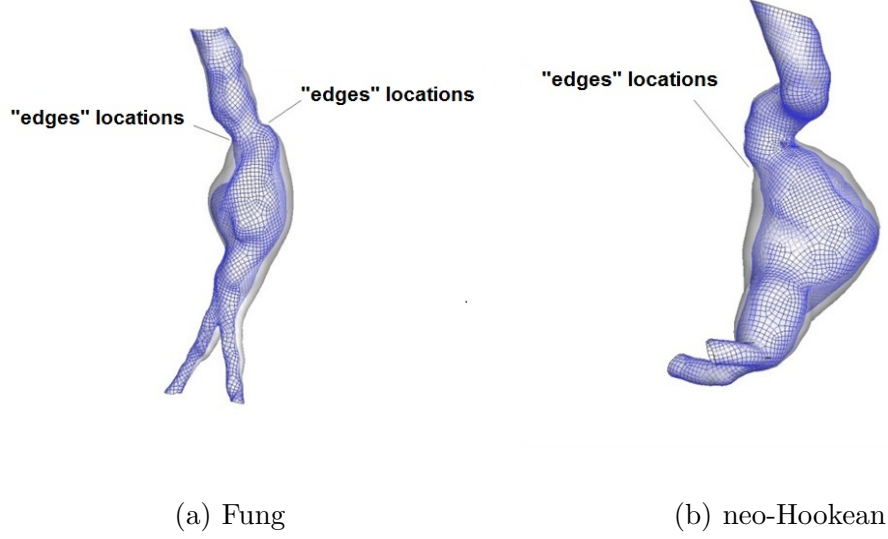


Figure 3.16: “Edge” points locations: (a) juvenile AAA; (b) full grown AAA.

AAA models, which all located on the edge of the large concave part for both the juvenile AAA and full grown AAA. We mark them in Figure 3.16. These “edges” do not have so large bending moments as in concave regions, but their stresses are still affected by the concavities.

The full grown AAA model shows more profound stress insensitivity to material properties. This is likely because the large bulge resembles a shallow sac, despite the overall tubular topology. In the next section, we will further explore the influence of overall topology.

3.2 Saccular geometries - 26 human cerebral aneurysms

For a further comparison of forward and inverse method, we used 26 patient-specific cerebral aneurysms. Initial FE geometries of the cerebral aneurysms were

segmented from Computer Tomography Angiography (CTA) images by Dr. Manasi Ramachandran, in the Biomedical Engineering Department, University of Iowa. Computed Tomography Angiographic (CTA) images of 26 saccular, patient-specific IAs were obtained during routine clinical care at University Central Hospital, Helsinki, Finland. The study was approved by the local ethics committee and the patients or their relative gave informed consent. The data analysis portion of Human subjects research in this project is approved under the University of Iowa Institutional Review Board, project #200706742. The FE geometries are further remeshed into quadrilateral element in Gambit (commercial CFD analysis software by Fluent Inc.).

The difference between the population study and the single aneurysm study in previous Section is that, we only evaluate the stress sensitivity in one material model, the Fung model. The energy function for this Fung model is written as

$$\psi_m = c(e^Q - 1), \quad (3.4)$$

$$Q = d_1 E_{11}^2 + d_2 E_{22}^2 + 2d_3 E_{11} E_{22} + d_4 E_{12}^2.$$

The material parameters c, d_1, d_2, d_3, d_4 are set as $c = 0.28 N/mm$, $d_1 = 17.58$, $d_2 = 12.19$, $d_3 = 7.57$, $d_4 = 4.96$. The wall thickness of cerebral aneurysms are all set to be uniformly $0.2mm$. We assume the cerebral aneurysms are fixed at the boundary edges and under 120 mmHg pressure.

3.2.1 Stress results

The stress results will be presented for all 26 patient-specific cerebral aneurysms. Figures (3.17)-Figures (3.21) show the first principal stress results by using forward and inverse method, respectively. In these figures, the upper rows represent the stress

result computed by forward method and the lower rows are results by using inverse method.

From these figures, we can find that in some cases, the maximum principal stress value is higher by using forward method; while in some cases, the comparisons are on the contrary. Because the maximum stress is an important factor to predict the rupture, it is necessary to compare maximum stress between forward and inverse method. To avoid the peak stress caused by stress concentration, the 95% of the maximum first principal stress is used in this comparison. Figures (3.22) further indicate that it is the geometry which affects the maximum stress value.

3.2.2 Stress sensitivity study

A sensitivity study is performed by directly comparing the stress solutions obtained from two sets of material constants. We set the reference model with material parameters introduced previously. A comparative material model is generated by magnifying the stiffness parameter c by 100 times. The first principal stress difference is defined as $\frac{|p'_1 - p_1|}{|p_1|} \times 100\%$, p_1 is the first principal stress computed from the reference material model and p'_1 the first principal stress computed by comparative material model. Figures (3.23)- Figures (3.27) show the distribution of principal stress differences of all cerebral aneurysms. The statistic comparison of stress differences for whole 26 cerebral aneurysms is showed in Figures (3.28). To avoid the peak stress differences caused by boundary effects or stress concentration, we use the 95% maximum stress differences to conduct the comparison. We find that the inverse method

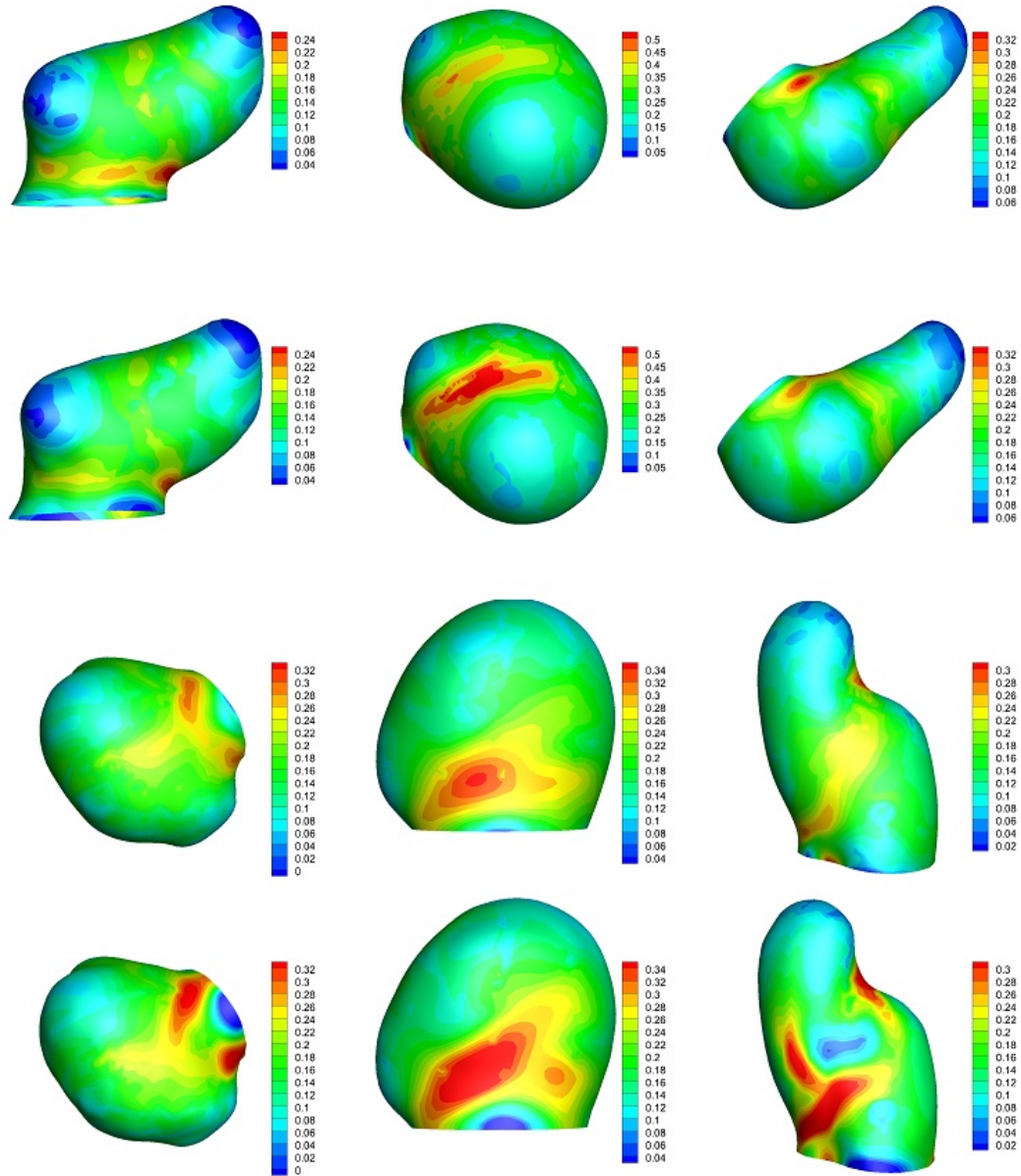


Figure 3.17: First principal stress distributions, part *I*. Upper row: the stress result computed by forward method; lower row: the stress result computed by inverse method.

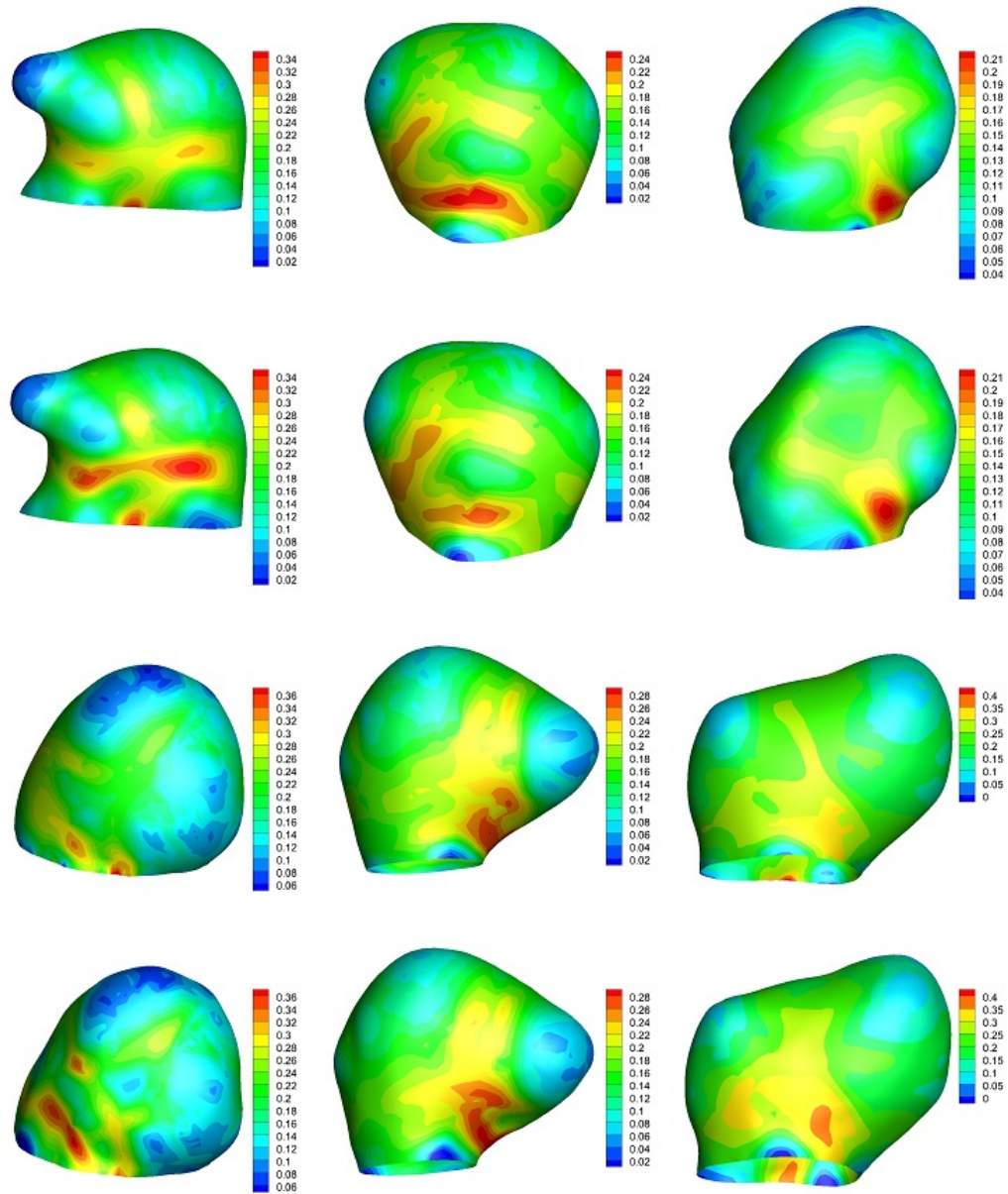


Figure 3.18: First principal stress distributions, part *II*. Upper row: the stress result computed by forward method; lower row: the stress result computed by inverse method.

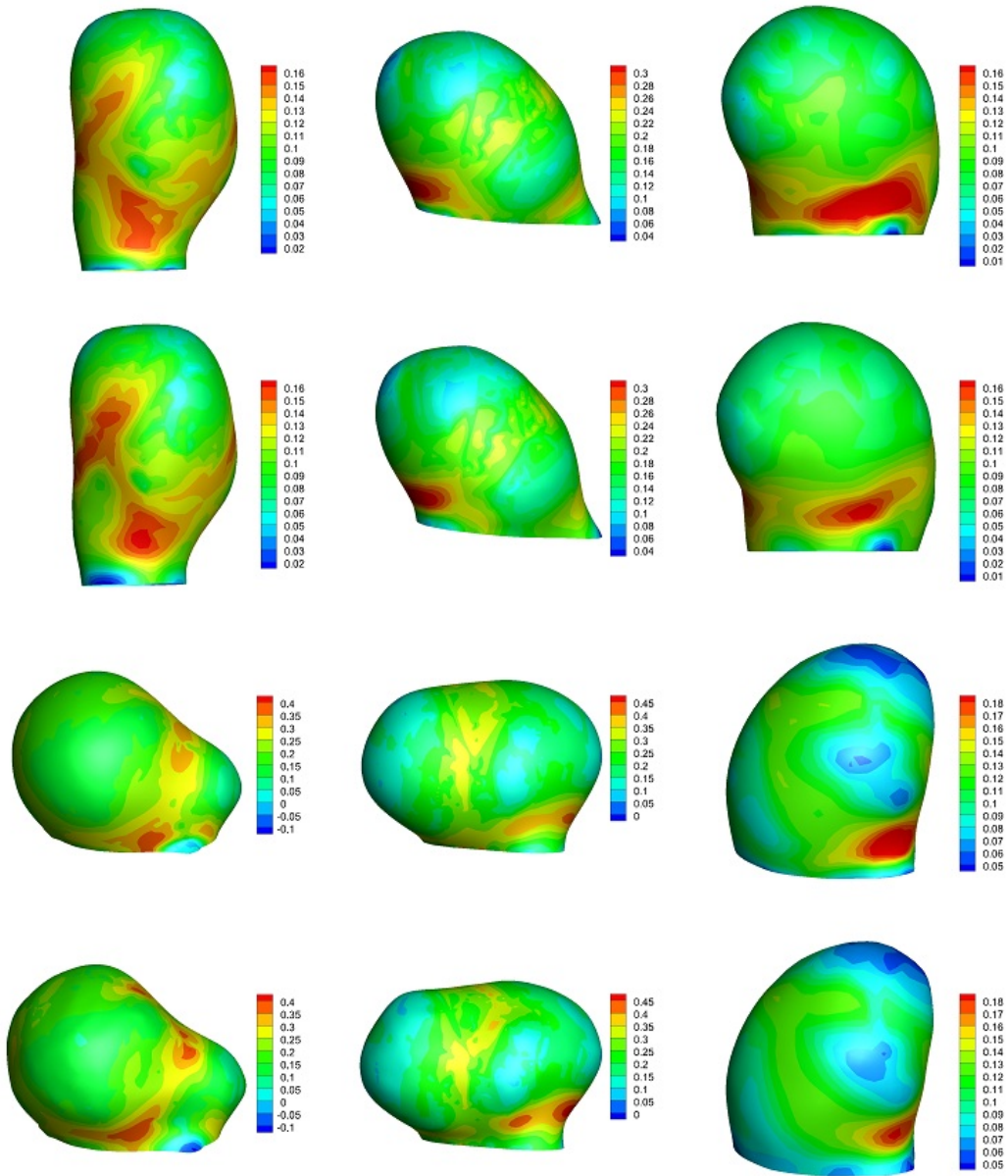


Figure 3.19: First principal stress distributions, part *III*. Upper row: the stress result computed by forward method; lower row: the stress result computed by inverse method.

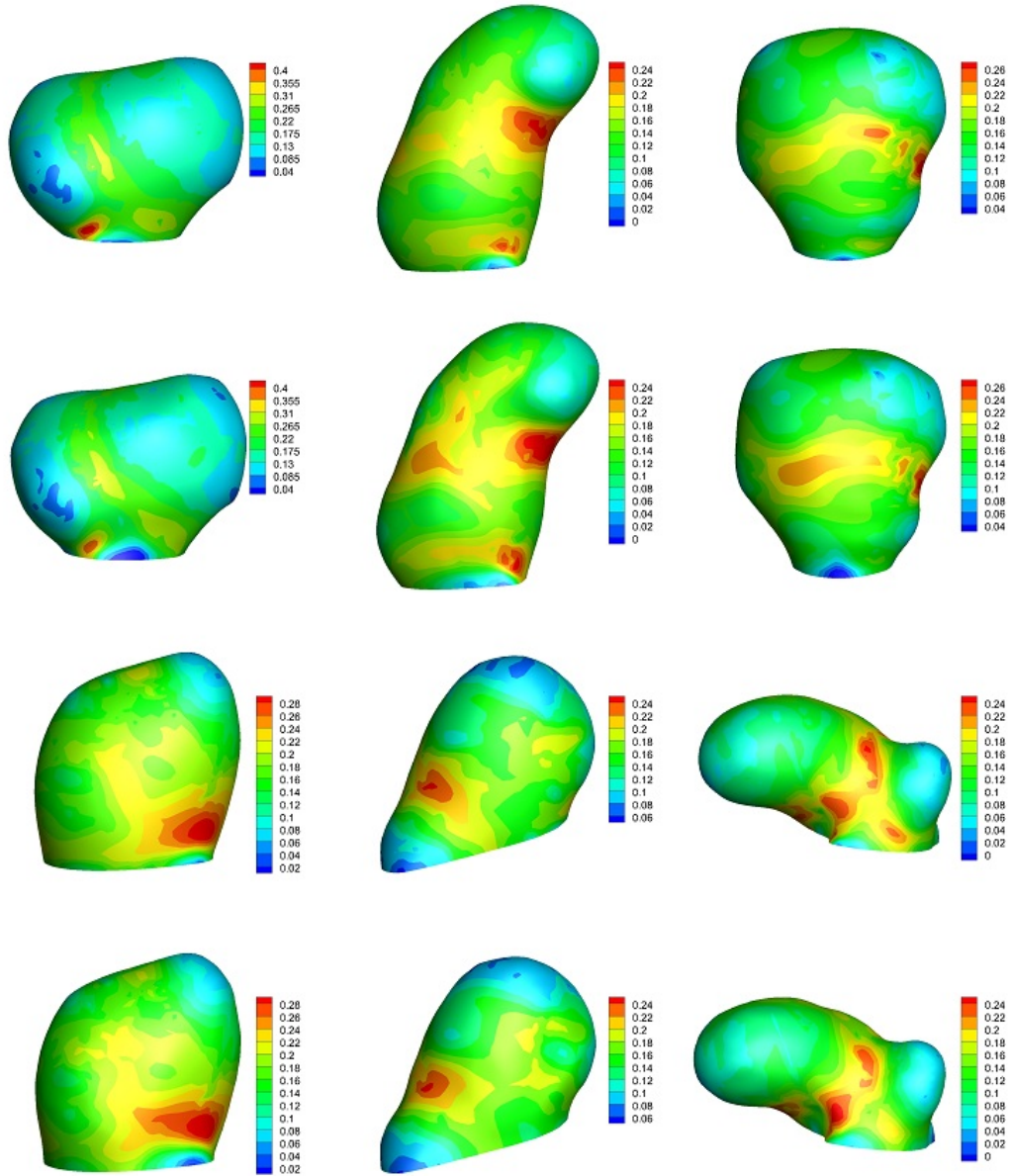


Figure 3.20: First principal stress distributions, part *IV*. Upper row: the stress result computed by forward method; lower row: the stress result computed by inverse method.

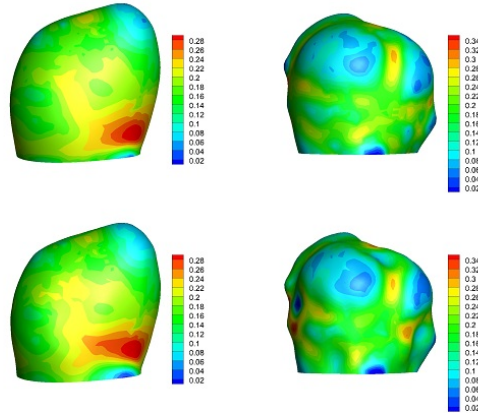


Figure 3.21: First principal stress distributions, part *V*. Upper row: the stress result computed by forward method; lower row: the stress result computed by inverse method.

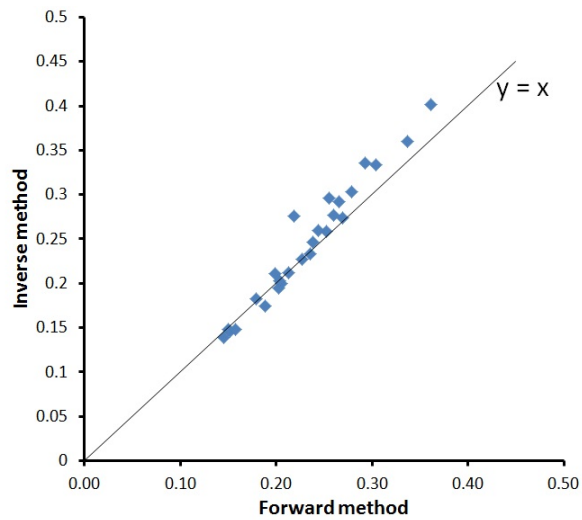


Figure 3.22: The comparison of 95% of the maximum first principal stress between forward and inverse method, respectively.

can provide far less sensitive stress result; the maximum stress differences of inverse method are below 10% for call cases.

In this section, we also compute the bending factor for 26 human cerebral aneurysms. Figures 3.29-Figures 3.29 present the distributions of bending factor by using Fung material model in inverse analysis. From these figures, we can find that in most models, the bending factors in most regions are less than 0.03, even in the regions with large concavity, the bending factors are still around 0.1. In this case, we can conclude that in the saccular aneurysm, the bending stress is much smaller than the membrane stress, and ensure the feasibility of shell PWIM.

3.3 Discussion

3.3.1 Stress insensitivity study

Two AAA models (tubular geometries) are used to compare the stress distribution by using the forward method and the inverse method. With the comparison of two families of material models (four sets of material models), it is shown that the stress distributions calculated by the inverse method are more insensitive to the material model or parameters. The bending stress are also investigated, comparing the stress differences between material models. The results show that the stress differences may be affected with bending stresses increment.

We use 26 realistic human cerebral aneurysms as saccular geometrical examples to investigate the stress differences between forward and inverse method. We first show that the major factor to affect the maximum stress is geometry, not the analysis

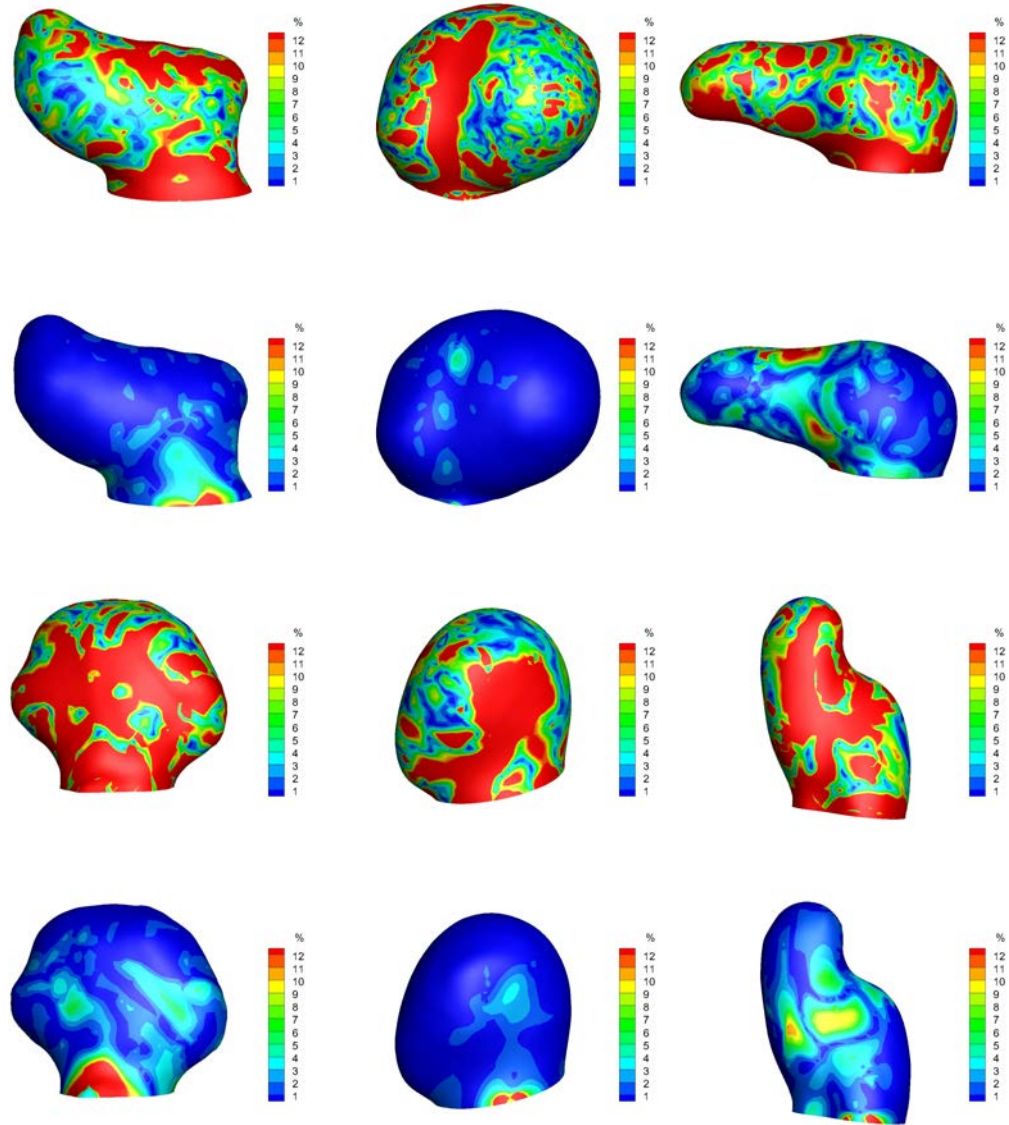


Figure 3.23: First principal stress differences by using forward and inverse method, respectively, part *I*. Upper row: the stress result computed by forward method; lower row: the stress result computed by inverse method.

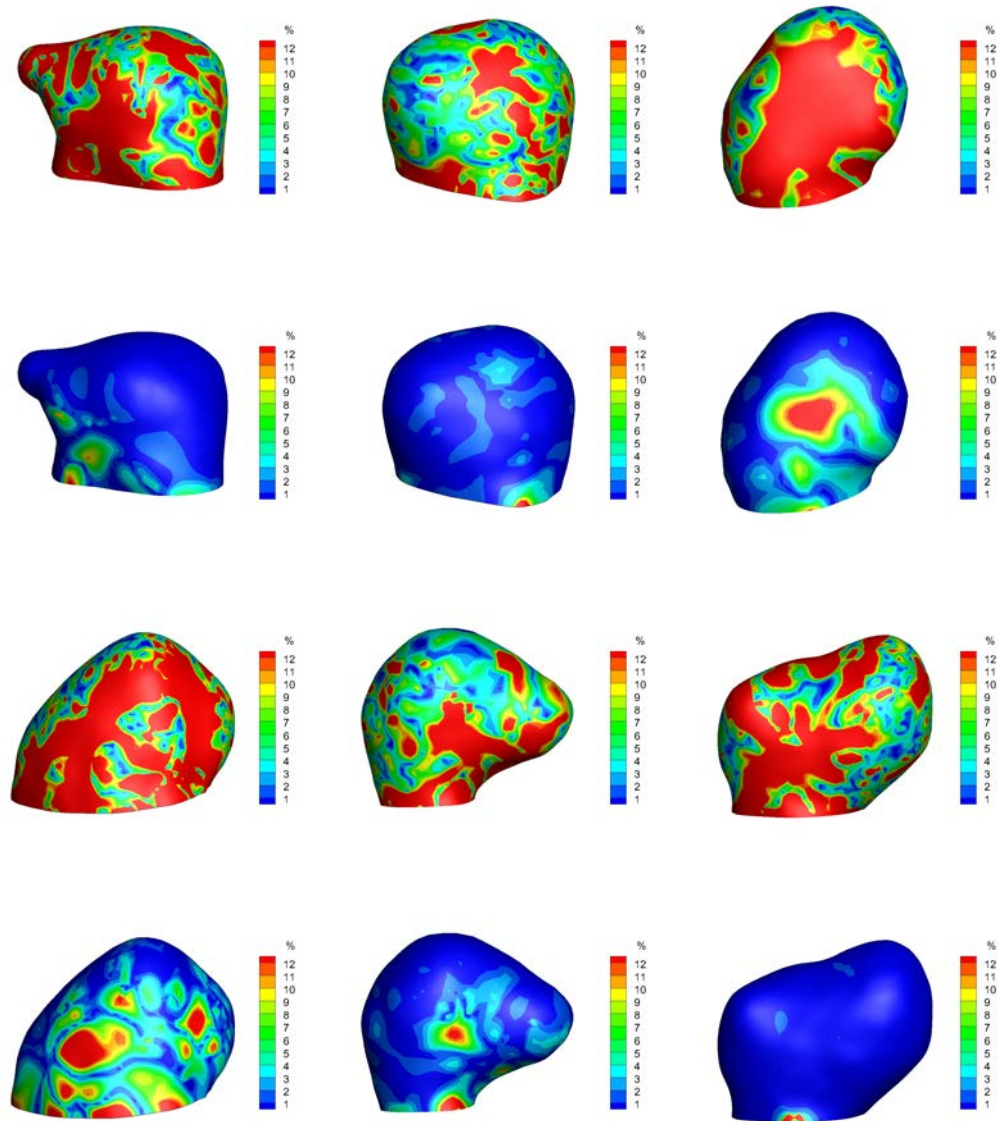


Figure 3.24: First principal stress differences by using forward and inverse method, respectively, part *II*. Upper row: the stress result computed by forward method; lower row: the stress result computed by inverse method.

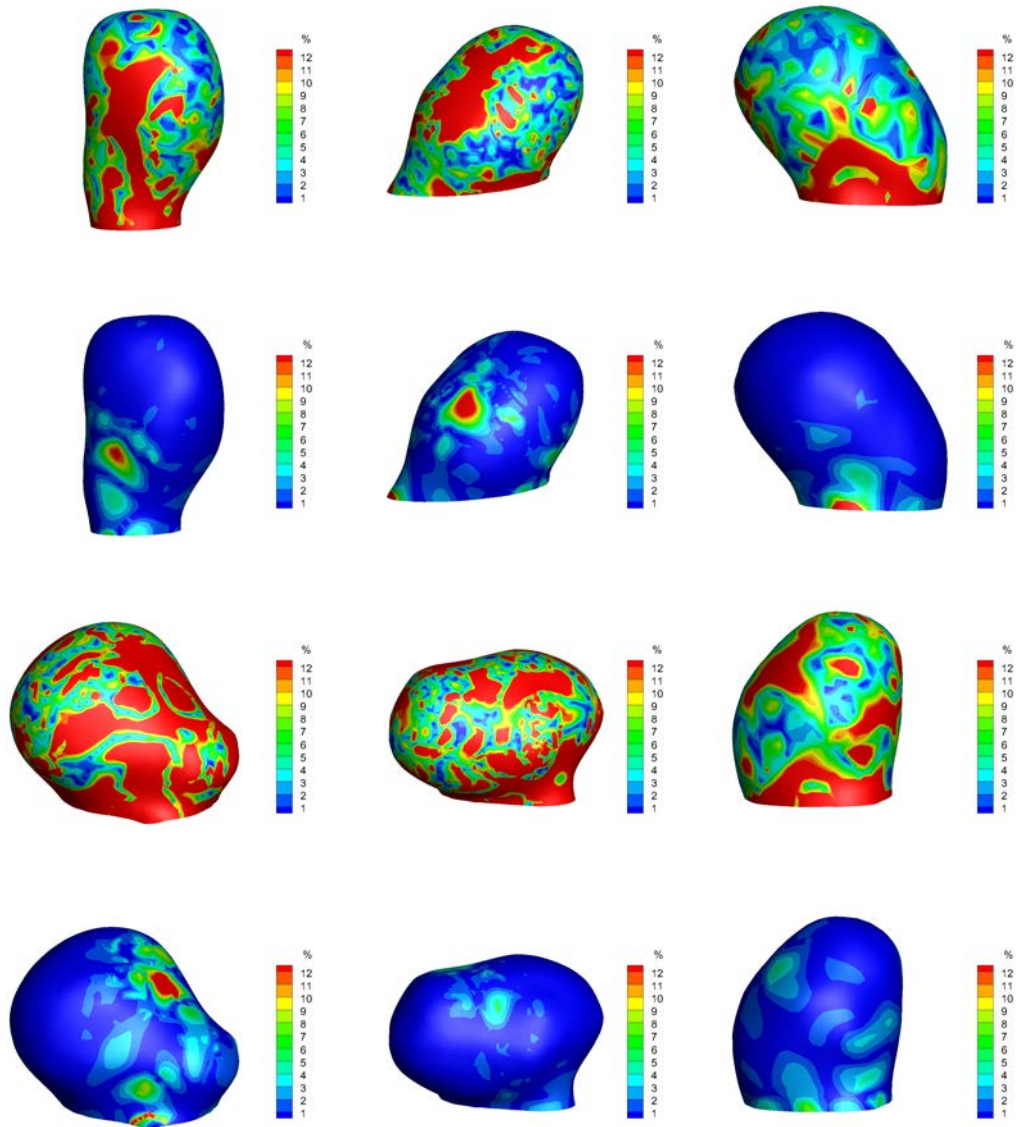


Figure 3.25: First principal stress differences by using forward and inverse method, respectively, part *III*. Upper row: the stress result computed by forward method; lower row: the stress result computed by inverse method.

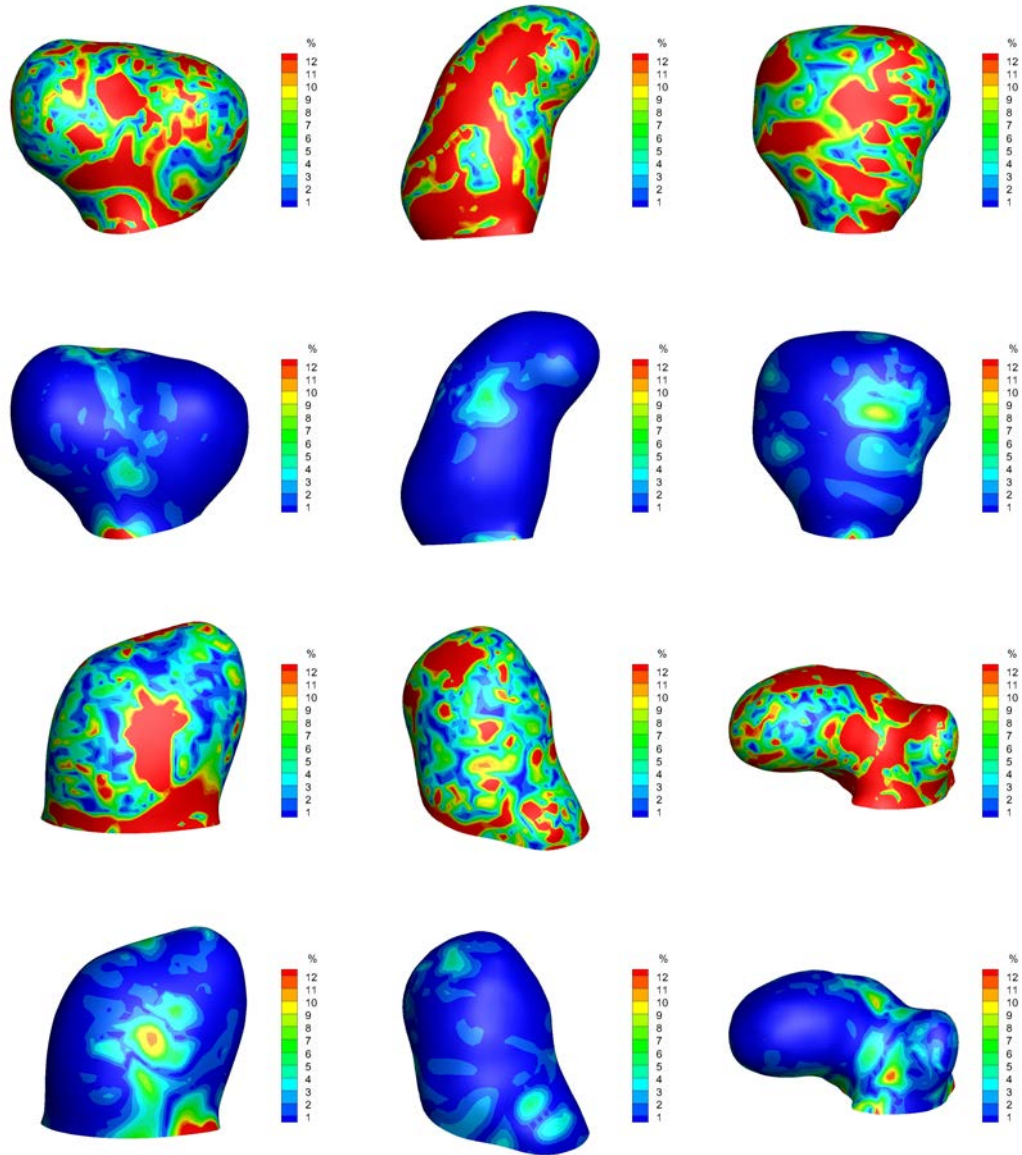


Figure 3.26: First principal stress differences by using forward and inverse method, respectively, part *IV*. Upper row: the stress result computed by forward method; lower row: the stress result computed by inverse method.

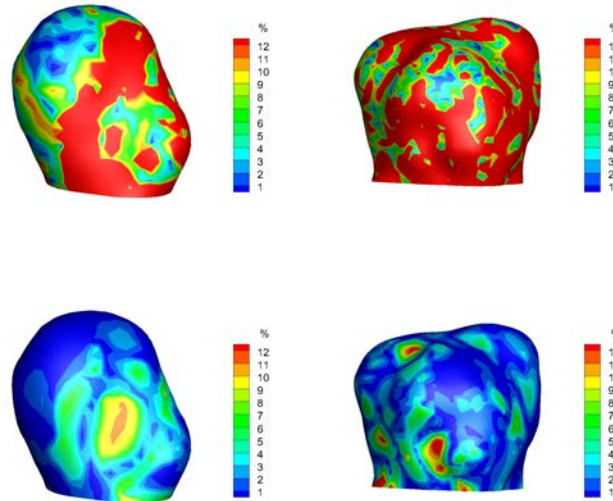


Figure 3.27: First principal stress differences by using forward and inverse method, respectively, part V. Upper row: the stress result computed by forward method; lower row: the stress result computed by inverse method.

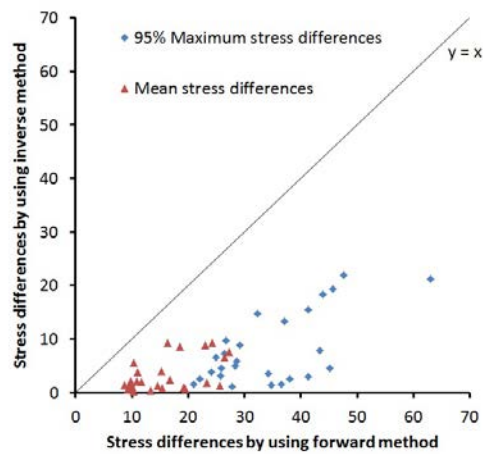


Figure 3.28: Stress sensitivity in inverse and forward analysis.

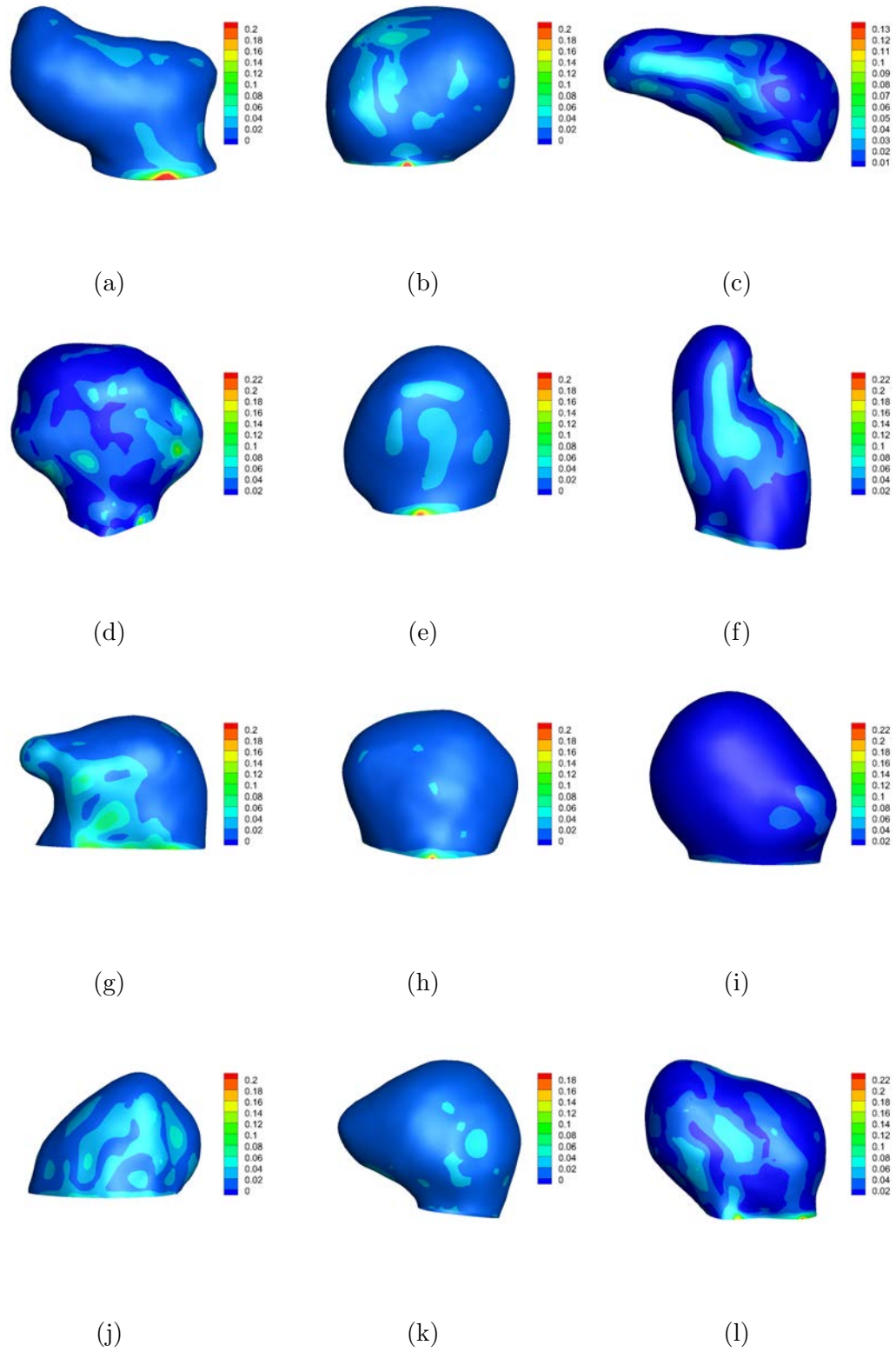


Figure 3.29: Bending factors in 26 patient-specific cerebral aneurysms, part I.

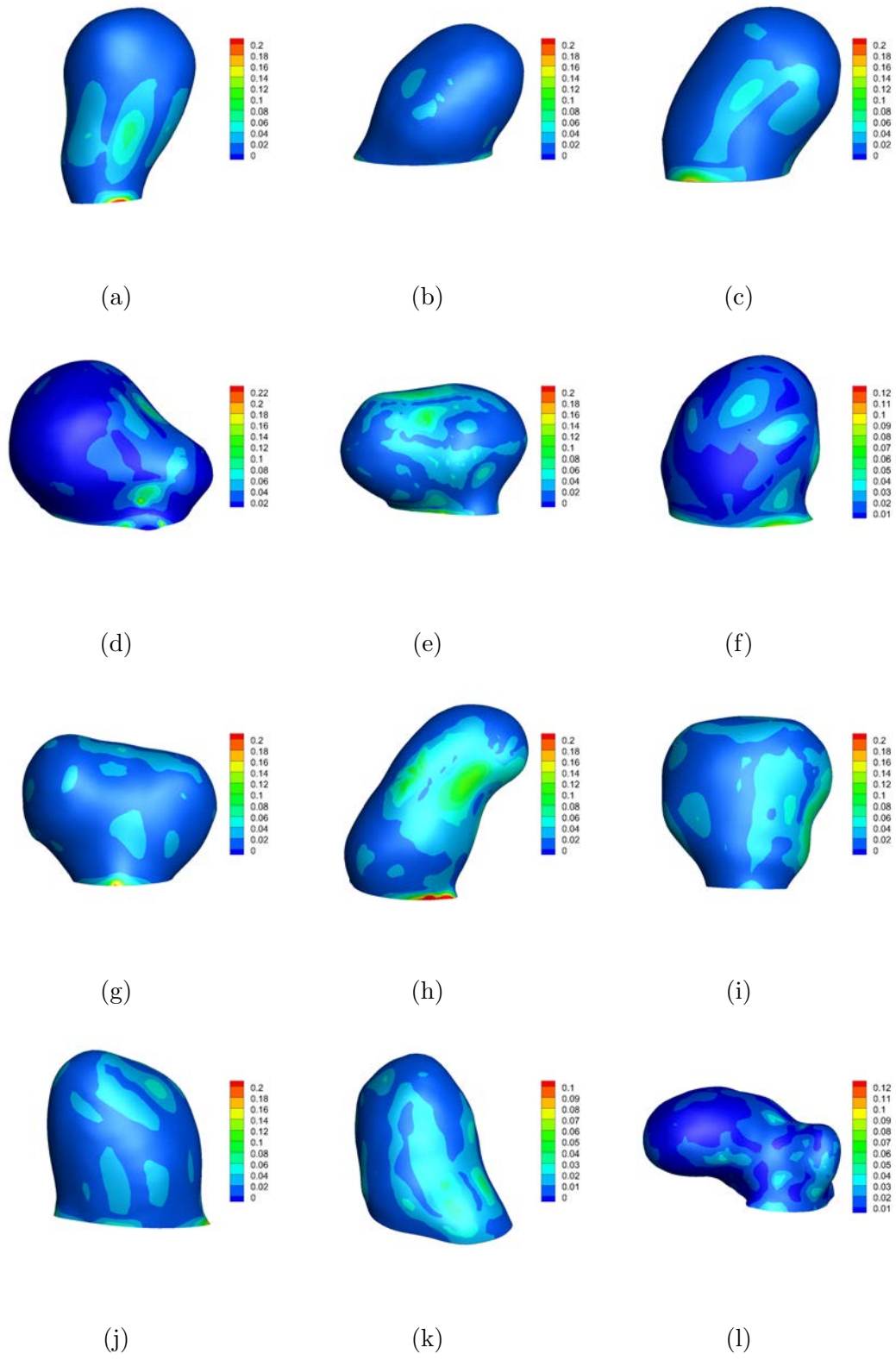


Figure 3.30: Bending factors in 26 patient-specific cerebral aneurysms, part II.

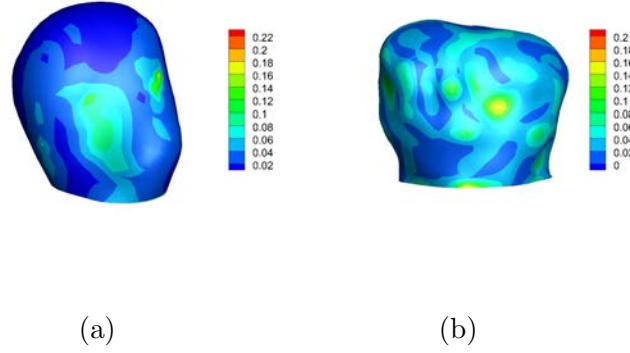


Figure 3.31: Bending factors in 26 patient-specific cerebral aneurysms, part III.

method. In the stress sensitivity study, we also show that the inverse method can provide close stress predictions even though the material parameters vary in a large range.

The stress in cerebral aneurysms (saccular geometries) are more insensitive to material models. In another word, the cerebral aneurysms turn to be more likely statically determined. This can be explained from two angles. The first one, is the relative thickness in two aneurysms are different; the relative thickness in AAA (*thickness/diameter* is around 1/15) is greater than cerebral aneurysms (*thickness/diameter* is around 1/35). The bending stress is in proportion to wall thickness; a thicker wall entails a higher bending stress which pushes the structure further away from being statically determined. The second reason is open versus closed geometry; AAA has more openings and thus the wall stress is more prone to the influence of boundary conditions. Collectively, the influence of geometry may be evaluated using the bending factor. Shell PWIM is expected to apply to cases

when the bending factor is small. It appears that cerebral aneurysms (large ones) are suitable for shell PWIM.

3.3.2 Implications of inverse analysis for AAA

Although the purpose of our study is not AAA stress analysis, the finding of stress sensitivity has an important implication for AAA analysis. AAA is the cause of death in 1.3% of men over 65 years of age in industrial countries, mostly due to rupture [61]. Current clinical practices evaluate the likelihood of rupture only on the basis of the maximum transverse bulge diameter [87]. Although this criterion is widely used, it has been reported that small AAAs can rupture while large ones do not [84]. From a biomechanical standpoint, rupture occurs when the wall stress exceeds the local strength of the tissue. Therefore, mechanical stress could be more relevant indicator for rupture assessment.

Considering the importance of stress evaluation, an important task of biomechanical analysis is to predict the wall stress in AAA. Researchers have been using the finite element method to calculate the stress distribution in AAAs [13, 12, 56, 85, 58]. In previous studies [13, 56], researchers showed that the shape affected the wall stress distribution within the realistic AAAs. Recently, many studies reported that using simplified linearly elastic material properties or inappropriate tissue material model can lead to erroneous stress distribution [82, 88]. Doyle et al. examined the effect of modeling on the resulting wall stress distributions of a realistic AAA. Using both linear and non-linear material properties, they showed that the peak wall stress was

reduced when more realistic parameters were utilized [8]. Nicosia et al. demonstrated that the utilization of an isotropic constitutive relation for the ascending aorta is insufficient in providing the wall stress distribution [54]. Vande Geest et al. [85] applied an anisotropic constitutive relation to patient-specific AAA simulation; the results suggest that the peak wall stress is significantly increased compared to those from isotropic material models. While this effect may be patient-specific, for some simulations the isotropic relation resulted in a higher peak stress. Recently Rodriguez's group [58, 57] investigated that the material anisotropy on the magnitude and distribution of the AAA's peak stress and showed that the anisotropy in the material behavior of aneurysmal tissue would scale up the maximum principal stress acting on the patient specific AAAs.

Studies cited above point to modeling factors that may affect the stress prediction in AAA analysis. There is an important issue that these studies overlooked: inverse versus forward method of analysis. The current study clearly indicate that the inverse method give a more reliable stress prediction in the sense that the solution is much less sensitive to the use of material model. This is important for practical applications because it is impossible to accurately obtain the heterogeneous and anisotropic properties of AAA tissues. From the forward analysis, we can see that the material models affect the wall stress distribution and peak stress value up to 30% of difference. Accurate material descriptions are needed for predicting the initial geometry as well as stresses in a different pressure; however, as long the stress in the given deformed state is concerned, the inverse method appears to give a more reliable

prediction.

CHAPTER 4

IMPLEMENTATION OF A CEREBRAL ANEURYSM TISSUE MODEL IN FORWARD AND INVERSE SHELL ELEMENT

Kroon and Holzapfel [41, 42] developed a hyperelastic material model specifically to describe collagenous structures in the cerebral aneurysm tissues [33, 32, 65]. The model describes the tissue as a 8-ply laminate of collagen sheets with uni-directionally aligned fibers within each laminate. This 8-ply laminate structure is characterized as that the collagen fibers are uni-directionally aligned within each laminate. Holzapfel's model was used in the development of membrane PWIM [98]. In this work, this material is implemented into forward and inverse shell element to facilitate the development of shell PWIM.

4.1 Holzapfel model

In the Holzapfel material model in this work, the each fiber angle with respect to a local in-plane coordinate axis can be computed with this equation

$$\phi_I = \frac{I-1}{8}\pi, \quad I = 1, 2, \dots, 8. \quad (4.1)$$

In this case, the principal collagen fiber directions, $\eta_1 - \eta_2$ in Figure 4.1, are defined by rotation angle θ with respect to the reference coordinate system $\eta'_1 - \eta'_2$. Because the collagen fibers are uniformly distributed, the two principal fiber directions $\eta_1 - \eta_2$ (or $\eta'_1 - \eta'_2$) are locally orthogonal.

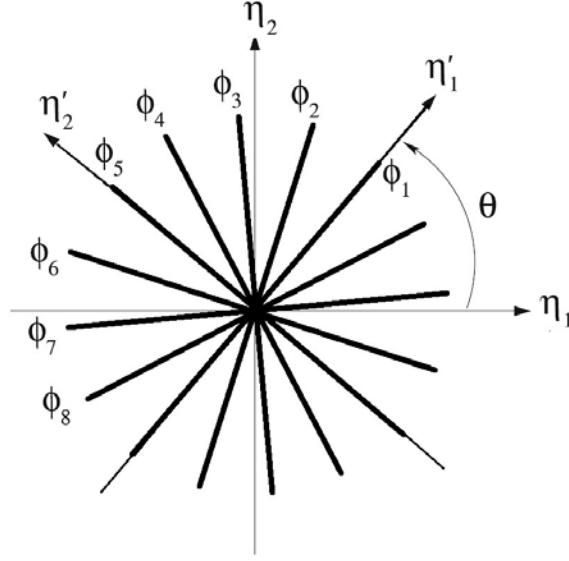


Figure 4.1: Schematic illustration of uniformly distributed collagen fibers (Reproduced from [42]).

The model is specified by the energy function [42]

$$\psi_m = \sum_{I=1}^8 \frac{k_I}{8a} (\exp[a(\lambda_I^2 - 1)^2] - 1), \quad (4.2)$$

$$\lambda_I^2 = \mathbf{C} \cdot \mathbf{N}_I \otimes \mathbf{N}_I, \quad (I = 1, 2, \dots, 8).$$

In this equation \mathbf{N}_I is the I -th fiber direction vector, k_I is the I -th fiber stiffness, λ_I denotes the stretch along the I -th collagen fiber. a is a dimensionless material constant, the exponent a is the amount of nonlinearity of the collagen fibers, and a is assumed to be the same value through the thickness for all collagen fibers. \mathbf{C} is the in-plane right Cauchy-Green tensor. So in the energy density function, k_I and a are the material parameters.

It can be derived that $E_1 = \sum_{I=1}^8 k_I \cos^4 \phi_I$ and $E_2 = \sum_{I=1}^8 k_I \sin^4 \phi_I$ [42] are

the material's principal symmetry direction's stiffness parameters. With reference Figure 4.1, k_1 and k_5 are the fiber stiffness along the first principal direction η_1 and second principal direction η_2 , respectively. The relation between k_1 and k_5 and other fiber stiffness is assumed to be [98]

$$\begin{aligned} k_I &= \frac{5-I}{4}k_1 + \frac{I-1}{4}k_5, \quad I = 2, 3, 4; \\ k_I &= \frac{9-I}{4}k_5 + \frac{I-5}{4}k_1, \quad I = 6, 7, 8. \end{aligned} \quad (4.3)$$

From Eq.(4.3), we can establish the relation between E_1, E_2 and k_1, k_5 . Through the principal stiffness parameters E_1, E_2 , the 8-fiber stiffness can be computed by

$$\begin{bmatrix} k_1 \\ k_5 \end{bmatrix} = \begin{bmatrix} \frac{1}{6}(7-3\sqrt{2}) & \frac{1}{6}(-5+3\sqrt{2}) \\ \frac{1}{6}(-5+3\sqrt{2}) & \frac{1}{6}(7-3\sqrt{2}) \end{bmatrix} \begin{bmatrix} E_1 \\ E_2 \end{bmatrix}. \quad (4.4)$$

4.2 Constitutive equations

In the direct shell theory, the energy function ψ consists three components

$$\psi = \psi_m + \psi_b + \psi_s. \quad (4.5)$$

ψ_m , ψ_b , and ψ_s represent the membrane energy, bending energy, and transverse shear energy, respectively; they depend on surface deformation tensor ($\boldsymbol{\varepsilon}$), curvature tensor ($\boldsymbol{\rho}$) and shear strain($\boldsymbol{\delta}$), respectively. We defined

$$\begin{aligned} \boldsymbol{\varepsilon} &:= \varepsilon_{\alpha\beta} \mathbf{A}^\alpha \otimes \mathbf{A}^\beta = \frac{1}{2}(a_{\alpha\beta} - A_{\alpha\beta}) \mathbf{A}^\alpha \otimes \mathbf{A}^\beta, \\ \boldsymbol{\rho} &:= \rho_{\alpha\beta} \mathbf{A}^\alpha \otimes \mathbf{A}^\beta = (\kappa_{\alpha\beta} - K_{\alpha\beta}) \mathbf{A}^\alpha \otimes \mathbf{A}^\beta, \\ \boldsymbol{\delta} &:= \delta_\alpha = (\gamma_\alpha - \Gamma_\alpha) \mathbf{A}^\alpha. \end{aligned} \quad (4.6)$$

4.2.1 Forward stress function

We introduce the constitutive relations for the 8-fiber Holzapfel material model used in the forward method. As discussed, the surface energy density for the 8-fiber

Holzappel material model is assumed to take the form

$$\psi_m = \sum_{I=1}^8 \frac{k_I}{8a} (\exp[a(\lambda_I^2 - 1)^2] - 1), \quad (4.7)$$

$$\lambda_I^2 = \mathbf{C} \cdot \mathbf{N}_I \otimes \mathbf{N}_I, \quad (I = 1, 2, \dots, 8),$$

where k_I and a are material parameters. The energy form gives rise to the following tension function

$$\tilde{T}_s^{\alpha\beta} = \sum_{I=1}^8 \frac{k_I}{2} (\exp[a(\lambda_I^2 - 1)^2] - 1)(\lambda_I^2 - 1)(N_I^p A_{pq} N_I^q)^{-1} N_I^\alpha N_I^\beta. \quad (4.8)$$

The material tangent tensor is derived by equation

$$D_{mm}^{\alpha\beta\delta\gamma} = 2 \frac{\partial \tilde{T}_s^{\alpha\beta}}{\partial a_{\delta\gamma}}. \quad (4.9)$$

We can further get

$$D_t^{\alpha\beta\delta\gamma} = D_{mm}^{\alpha\beta\delta\gamma} = \sum_{I=1}^8 k_I [2a(\lambda_I^2 - 1)^2 + 1] (N_I^p A_{pq} N_I^q)^{-2} N_I^\alpha N_I^\beta N_I^\delta N_I^\gamma. \quad (4.10)$$

Following the construction of bending energy function presented in [101], the bending energy is assumed to take the form

$$\psi_b = \frac{h^2}{24} H^{\alpha\beta\delta\gamma} \rho_{\alpha\beta} \rho_{\delta\gamma}, \quad (4.11)$$

where $\mathbb{H} = H^{\alpha\beta\delta\gamma} \mathbf{A}_\alpha \otimes \mathbf{A}_\beta \otimes \mathbf{A}_\delta \otimes \mathbf{A}_\gamma$ is the elasticity tensor at the ground state, that is, $\boldsymbol{\varepsilon} = \mathbf{0}$. So we can get $H^{\alpha\beta\delta\gamma}$ from the following formula

$$H^{\alpha\beta\delta\gamma} := D_{mm}^{\alpha\beta\delta\gamma}|_{\lambda_I=1} = 4 \frac{\partial^2 \psi_m}{\partial a_{\alpha\beta} \partial a_{\delta\gamma}}|_{\varepsilon_{\alpha\beta}=0}. \quad (4.12)$$

So the ground state elasticity tensor of the membrane energy function of 8-fiber Holzappel model can be obtain as

$$H^{\alpha\beta\delta\gamma} = \sum_{I=1}^8 k_I N_I^\alpha N_I^\beta N_I^\delta N_I^\gamma. \quad (4.13)$$

The transverse shear strain energy ψ_s takes the form

$$\psi_s = \frac{1}{2}G\delta_\alpha A^{\alpha\beta}\delta_\beta, \quad (4.14)$$

where G is the shear moduli and set as $G = \frac{E_1+E_2}{2}$. The shear resultant is

$$\tilde{Q}_s^\alpha = \frac{\partial\psi_s}{\partial\delta_\alpha} = GA^{\alpha\beta}\delta_\beta. \quad (4.15)$$

So the material tensor for shear can be computed as

$$D_s^{\alpha\beta} = \frac{\partial\tilde{Q}_s^\alpha}{\partial\delta_\beta} = GA^{\alpha\beta}. \quad (4.16)$$

4.2.2 Inverse stress function

The surface energy density for the 8-fiber Holzapfel material model still takes the form in Eq. (4.7). The energy form gives rise to the following tension function

$$\tilde{t}^{\alpha\beta} = J^{-1} \sum_{I=1}^8 \frac{k_I}{2} (\exp[a(\lambda_I^2 - 1)^2] - 1)(\lambda_I^2 - 1)(n_I^p A_{pq} n_I^q)^{-1} n_I^\alpha n_I^\beta, \quad (4.17)$$

where $J^{-1} = 1/\det\mathbf{F}$.

Different from the forward method, in inverse calculation, the material tangent tensor for membrane part is derived by equation

$$D_t^{\alpha\beta\delta\gamma} = 2 \frac{\partial\tilde{t}^{\alpha\beta}}{\partial A_{\delta\gamma}}. \quad (4.18)$$

Eq. (2.53) can also written as $D_t^{\alpha\beta\delta\gamma} = 2J^{-1} \frac{\partial(\tilde{T}_s^{\alpha\beta})}{\partial A_{\delta\gamma}} + J^{-1} T_s^{\alpha\beta} A^{\delta\gamma}$. Set $D_{mm}^{\alpha\beta\delta\gamma} = 2 \frac{\partial(\tilde{T}_s^{\alpha\beta})}{\partial A_{\delta\gamma}}$, which can be computed by

$$D_{mm}^{\alpha\beta\delta\gamma} = - \sum_{I=1}^8 k_I \exp(\lambda_I^2 - 1)^2 [2a(\lambda_I^2 - 1)^2 + \lambda_I^2] (n_I^p A_{pq} n_I^q)^{-2} n_I^\alpha n_I^\beta n_I^\delta n_I^\gamma. \quad (4.19)$$

From the bending energy in last section, we can written the bending moment as

$$\tilde{M}^{\alpha\beta} = \frac{h^2}{12} H^{\alpha\beta\delta\gamma} \rho_{\delta\gamma}. \quad (4.20)$$

The material tensor for bending in [101] is written as

$$D_{bb}^{\alpha\beta\delta\gamma} = \frac{\partial \tilde{M}^{\alpha\beta}}{\partial K_{\delta\gamma}} = -\frac{h^2}{12} H^{\alpha\beta\delta\gamma}. \quad (4.21)$$

The material tensor for shear in [101] can be computed as

$$D_{ss}^{\alpha\beta} = \frac{\partial \tilde{Q}_s^\alpha}{\partial \Gamma_\beta} = -GA^{\alpha\beta}. \quad (4.22)$$

4.3 Validation

This material model is implemented into existing forward and inverse shell elements.

4.3.1 Forward-inverse loop

The element formulation is first validated using a forward-inverse loop. First, we assume an initial configuration \mathcal{R} , and apply the loads and boundary condition, to obtain the deformed configuration \mathcal{C} in the forward manner. Subsequently, the deformed configuration \mathcal{C} is used as input, through the inverse method, to compute the stress-free configuration \mathcal{R}' .

The material parameters are set as

$$E_1 = 0.92N/mm, \quad E_2 = 0.72N/mm, \quad a = 20. \quad (4.23)$$

In this study, the first principal fiber direction in the reference configuration

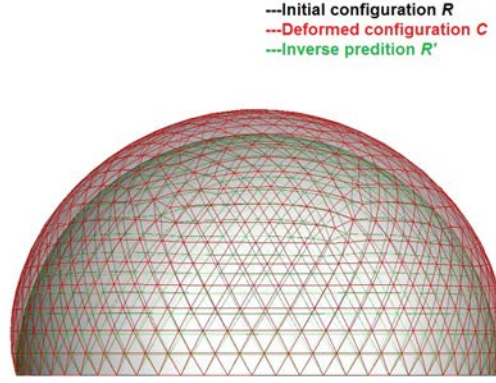


Figure 4.2: Prediction of inverse method.

is assumed to be parallel to the local basal plane. By using this material model, we will use two examples to validate the inverse method.

4.3.1.1 Example: pressurized hemisphere

A hemisphere shell is used in the analysis. The radius of this hemisphere is $1mm$, the thickness is set as $0.05mm$. The edge is fixed on both displacement and rotation. The 100 mmHg pressure is used as load.

Figure 4.2 shows the geometry of three configurations. The black mesh shows the initial configuration \mathcal{R} , the red mesh shows the configurations after the forward computation \mathcal{C} , and the green mesh shows the stress-free configuration \mathcal{R}' the inverse calculation predicted. At some places, we can only see green or black mesh, because the inverse prediction coincides with the the initial coordinate, so meshes overlap with each other.

To quantify the accuracy of inverse prediction, in Table 4.1 random nodes in hemisphere mesh are selected to compare the initial nodal coordinate with the same node's nodal coordinates inversely predicted from the deformed configuration. The coordinates comparison also shows that the inverse method can predict the stress-free configuration very well. The material model used here is 8-fiber anisotropic material model. In the inverse analysis step, the first principal fiber direction in the deformed configuration is also assumed to be parallel to the local basal plane. The fiber direction in the deformed configuration may be changed in the forward analysis step, and will not be parallel to the local basal plane. Since we are not using the actual deformed fiber direction in the inverse computation, the inverse model strictly speaking is different from the forward model, and that explains the small discrepancies in the position vectors.

Table 4.1: Nodal coordinate in initial configuration \mathcal{R} and stress-free configuration \mathcal{R}' predicted by inverse method.

Initial nodal coordinate	Inverse predicted coordinates
(0.9436E+00, 0.3194E+00, 0.8642E-01)	(0.9434E+00, 0.3203E+00, 0.8627E-01)
(0.9616E-01, -0.9917E+00, 0.8534E-01)	(0.9641E-01, -0.9933E+00, 0.8514E-01)
(0.5652E+00, 0.4240E-01, 0.8237E+00)	(0.5654E+00, 0.4245E-01, 0.8219E+00)
(-0.1278E-01, 0.3134E+00, 0.9495E+00)	(-0.1280E-01,0.3135E+00, 0.9473E+00)

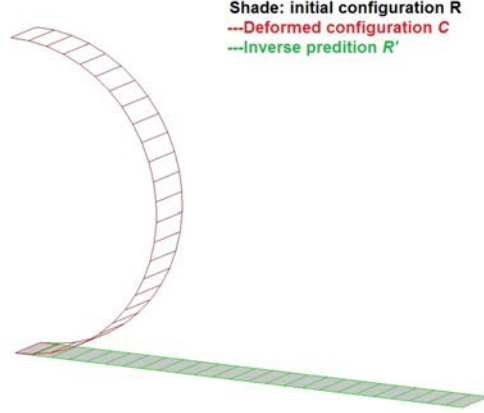


Figure 4.3: Prediction of inverse method.

4.3.1.2 Example: bending plate

In this example, we use a plate model as an example. We fix the position and rotation of one edge on the plate, and apply a bending moment on the other edge making the plate to roll-up.

Figure 4.3 shows the geometry of three configurations. To make it clearly to compare, the shade shows the initial configuration \mathcal{R} , the red mesh shows the configurations after the forward computation \mathcal{C} , and the green mesh shows the stress-free configuration \mathcal{R}' the inverse calculation predicted. We can find that the stress-free configuration \mathcal{R}' predicted by inverse method fits the initial configuration \mathcal{R} very well.

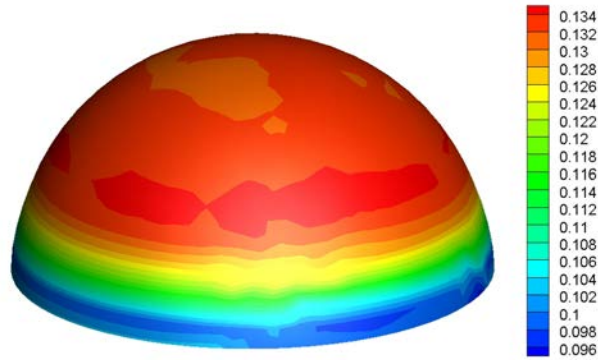


Figure 4.4: Stress distribution.

4.3.2 Stress solution

Taking the hemisphere as input to the inverse analysis, assuming the pressure $p = 100$ mmHg, the stress distribution in configuration \mathcal{R} is computed and is shown in Figure 4.4. If bending is not considered, the stress in the wall should follow the Laplace equation. If bending is considered, there is a boundary layer where the stress deviates from the Laplace solution but in the far field the stress should be asymptotic to the Laplace solution, $\sigma = \frac{pr}{2t}$, where p is internal pressure, t is wall thickness, r is mean radius [83]. The analytical result should be $\sigma = \frac{0.01332 \times 1}{2 \times 0.05} = 0.1332 N/mm^2$. In Figure 4.4, except the boundary effects, the membrane stress in most regions matches well the Laplace solution.

CHAPTER 5

POINTWISE IDENTIFICATION METHOD FOR SHELL STRUCTURES

This chapter introduce the pointwise identification method for shell structures and conduct a numerical verification for the method.

5.1 Pointwise identification method for shell structure

The general procedure of PWIM is shown in Figure 5.1.

Different with membrane structure, shell structures include bending. We have already shown that, larger bending stress will compromise the inverse stress insensitivity to material. So the first thing before applying the pointwise identification method is to evaluate the bending effects. If the bending stress is much smaller than the membrane stress, the membrane stress dominate the balance equations, and the membrane stress static-determinacy is also kept. In this case, constitutive regression in pointwise identification in shell structure can be operated on membrane strain-stress only.

In the deformed configurations, using $^{(i)}\sigma$ to represent the model stress in the i - th configuration, $^{(i)}\sigma$ can be expressed as a function of the following variables,

$$^{(i)}\sigma = \sigma(\mu_1, \dots, \mu_x, \epsilon). \quad (5.1)$$

$^{(i)}\hat{\sigma}$ represents the “experimental” stress obtained from the inverse shell computation. If we use μ_1, \dots, μ_x to represent the elastic parameter in the assumed con-

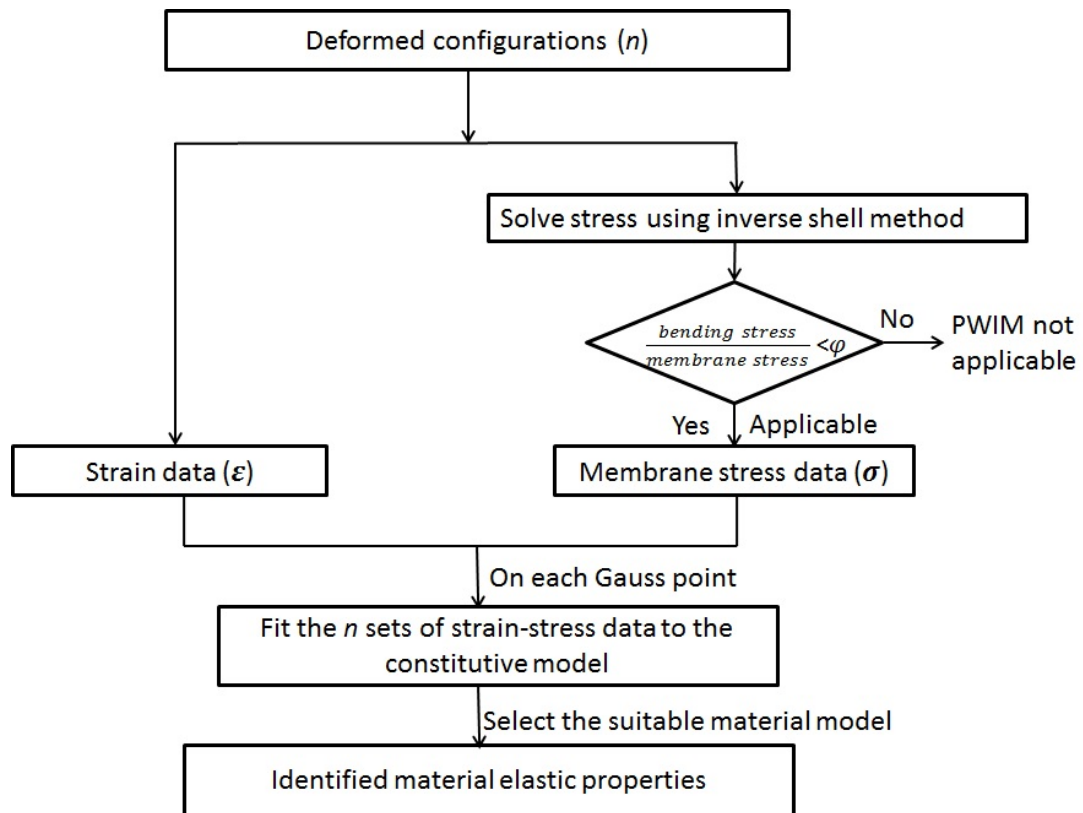


Figure 5.1: Flowchart of the pointwise identification procedure for shell structure.

stitutive equation, the objective function can be described as

$$\Phi = \sum_{i=1}^N \left\| {}^{(i)}\boldsymbol{\sigma} - {}^{(i)}\widehat{\boldsymbol{\sigma}} \right\|_w^2 = \sum_{i=1}^N [\mathbf{w} {}^{(i)}\boldsymbol{\sigma} - {}^{(i)}\widehat{\boldsymbol{\sigma}}] \cdot ({}^{(i)}\boldsymbol{\sigma} - {}^{(i)}\widehat{\boldsymbol{\sigma}}), \quad (5.2)$$

where \mathbf{w} is the matrix of weights, defined in § 2.4.3. $\Phi = \Phi(\mu_1, \dots, \mu_x)$ here is a function of elastic parameters only.

The regression problem can be described as

$$\begin{aligned} & \text{minimize} && \Phi(\mu_1, \dots, \mu_x), \\ & \text{subject to} && [\mu_1, \dots, \mu_x]^T \in [\mathbf{L.B.}, \mathbf{U.B.}] \end{aligned} \quad (5.3)$$

L.B. and **U.B.** are the lower and upper boundaries of the variables $[\mu_1, \dots, \mu_x]^T$.

5.2 Demonstration of the method using an aneurysm model

In this example (*CASEI*), the specific procedure for shell pointwise identification method is described in Figure 5.2. Due to the lack of knowledge about the wall thickness, We set the cerebral aneurysm has an uniformed thickness as 0.2 mm, and clamp the edge of arteries. The simulation of this inflation motion is conducted using the 8-fiber Holzapfel shell finite element in FEAP, introduced in last chapter.

In this section, the application of theory discussed in Chapter § (2.4) will be described. The cerebral aneurysm discussed in this chapter is constructed from CT images and treated as initial configuration. In this calculation, we set eleven pressurized states from 50 to 100 mmHg with the 5 mmHg increasement. Each deformed configuration have a set of strain and inverse stress correspondingly.

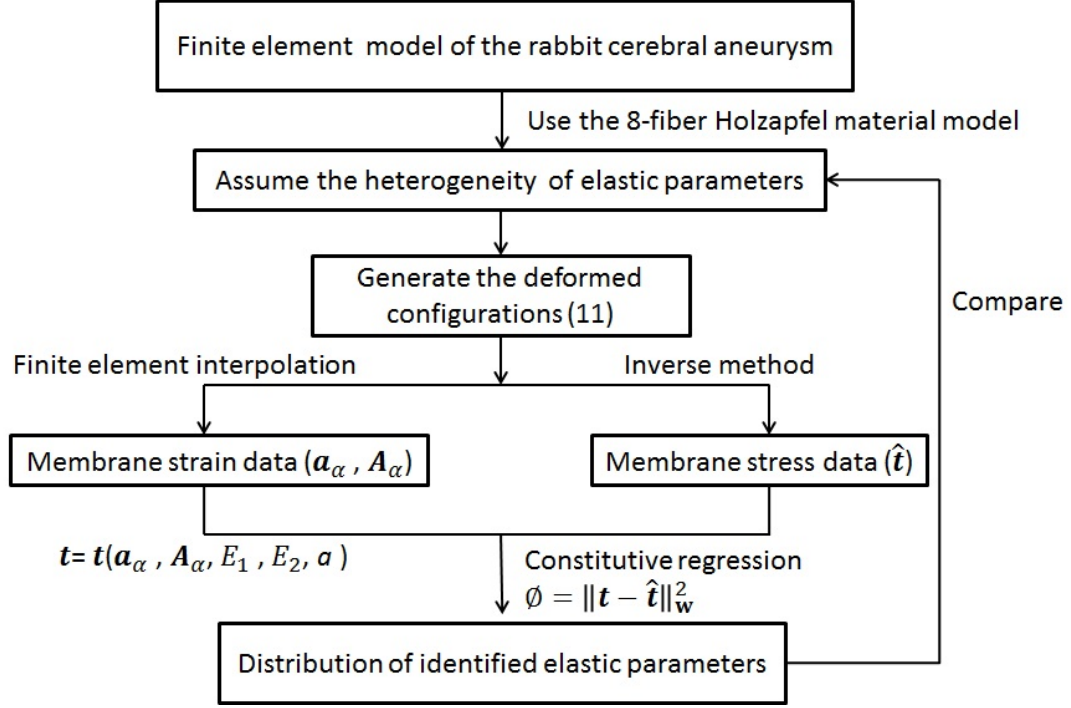


Figure 5.2: Flowchart of the numerical verification.

5.2.1 Material heterogeneity

To simulate the heterogeneity in realistic cerebral aneurysm, the stiffness parameters are assumed to decrease linearly with respect to the height of the sac region, while keeping the partial artery's property as same. We set a height value Z_{set} , if the heights from artery fundus are over Z_{set} , the stiffness parameter will decrease linearly, the areas below Z_{set} will have the same artery stiffness. so the stiffness parameters can be get by

$$E_i = \begin{cases} E_i^{artery} - \frac{E_i^{artery} - E_i^{dome}}{Z^{dome} - Z^{artery}} \times (Z - Z^{artery}), & Z > Z_{set}, i = 1, 2. \\ E_i^{artery}, & Z \leq Z_{set} \end{cases} \quad (5.4)$$

In this equation, Z is the “ Z ” coordinate of any Gauss point on the sac, Z^{artery} and Z^{dome} are the coordinates at the artery and dome regions, respectively. E_i^{artery}

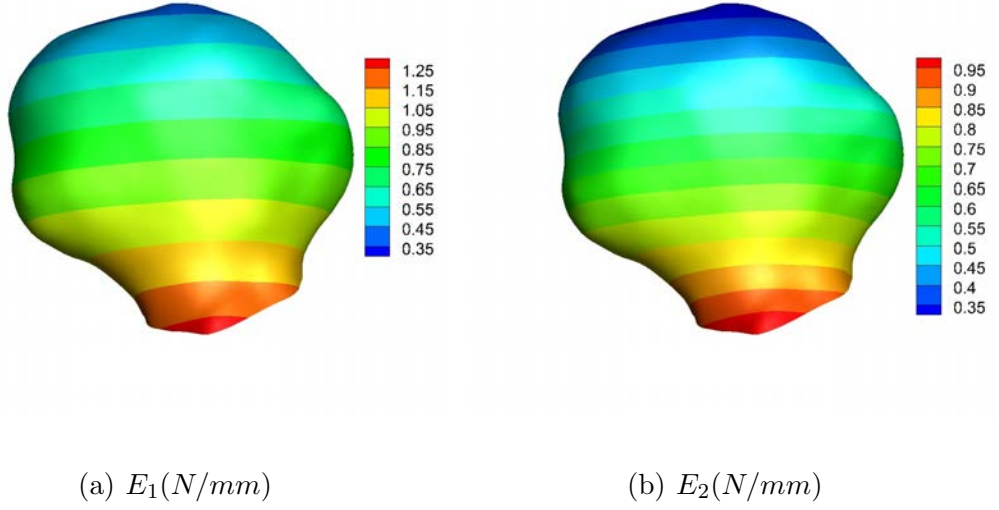


Figure 5.3: Assumed stiffness parameter distribution: (a) E_1 ; (b) E_2 .

and E_i^{dome} are the stiffness parameters at the artery and dome regions, respectively.

In this model we set,

$$\begin{aligned}
 E_1^{artery} &= 1.3N/mm, & E_1^{dome} &= 0.4N/mm, \\
 E_2^{artery} &= 1N/mm, & E_2^{dome} &= 0.3N/mm,
 \end{aligned}
 \tag{5.5}$$

The value of the parameter a is uniformly set to be 20. The distribution of the realistic parameters E_1 and E_1 showed in Figure 5.3. Forward deformations used to drive the inverse analyses are generated from this heterogeneous model.

5.2.2 Strain field

For each state, the strain can be computed through finite element interpolation as described in § 2.4. The surface inside an element is parameterized by the finite element natural coordinates. The base vector in the deformed and reference

configuration can be obtained through the following equations

$$\mathbf{a}_\alpha = \frac{\partial \mathbf{x}}{\partial \xi^\alpha} = \sum_{I=1}^{Nel} \frac{\partial \Phi_I}{\partial \xi^\alpha} \mathbf{x}^I, \quad \mathbf{A}_\alpha = \frac{\partial \mathbf{X}}{\partial \xi^\alpha} = \sum_{I=1}^{Nel} \frac{\partial \Phi_I}{\partial \xi^\alpha} \mathbf{X}^I, (\alpha, \beta = 1, 2), \quad (5.6)$$

where Nel is the total nodes on each element, Φ_I are the element interpolation functions.

The square of the stretch of an line element is

$$\lambda_I^2 = \frac{\mathbf{n}_I \cdot \mathbf{n}_I}{\mathbf{N}_I \cdot \mathbf{N}_I}. \quad (5.7)$$

In convected coordinate system, the $i - th$ fiber stretch can be written as

$$\lambda_I = \sqrt{\frac{N_I^\alpha a_{\alpha\beta} N_I^\beta}{N_I^\delta A_{\delta\gamma} N_I^\gamma}}, \quad (5.8)$$

where $a_{\alpha\beta} = \mathbf{a}_\alpha \cdot \mathbf{a}_\beta$ and $A_{\alpha\beta} = \mathbf{A}_\alpha \cdot \mathbf{A}_\beta$. The reference fiber directions \mathbf{N}_I is known and can presented as $\mathbf{N}_I = N_I^\alpha \mathbf{A}_\alpha$, where N_I are the components relative to the local surface bases. Because the fiber direction in the current configuration is defined as $\mathbf{n}_I = \mathbf{F} \mathbf{N}_I$, in the convected coordinate system, \mathbf{n}_I can be written as

$$\mathbf{n}_I = N_I^\alpha \mathbf{a}_\alpha, \quad (5.9)$$

where N_I^α is same. So fiber direction in all configurations can be determined, as soon as components relative to the local surface basis is known.

Figure 5.4(a) and Figure 5.4(b) show the distribution of the first and second principal stretches, respectively, at the deformed configuration under the highest pressure 100 mmHg. The largest principal surface stretch is $\lambda = 1.06$. In fact, the stretch of the wall in cerebral aneurysm is around $2\% \sim 5\%$. From the distribution of

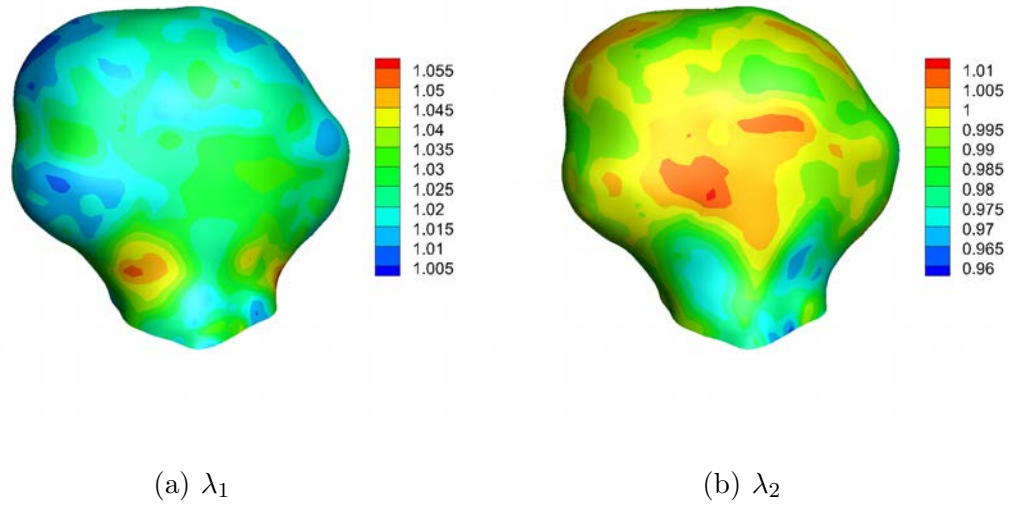


Figure 5.4: Distribution of the first and second principal stretches at $p = 100$ mmHg pressure: (a) λ_2 ; (b) λ_1 .

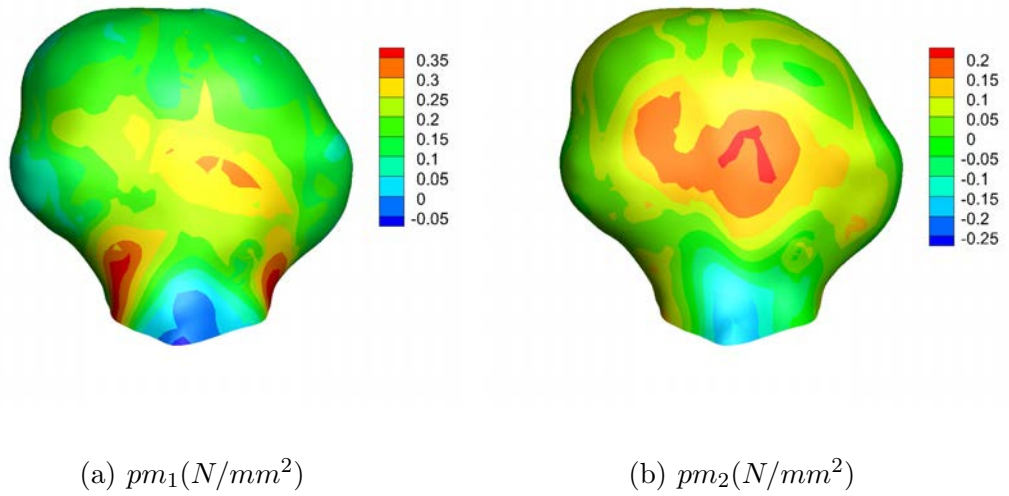


Figure 5.5: Distribution of the first and second principal stresses at $p = 100$ mmHg pressure: (a) $pm_1(N/mm^2)$; (b) $pm_2(N/mm^2)$.

principal stretches, we can find that the principal stretches in most regions are also in that range.

For comparison, correspondingly, we also show the first and second principal stress distribution, respectively, in Figure 5.5(a) and Figure 5.5(b). The regions have the higher principal stretches, also present the higher principal stresses.

5.2.3 Stress field

Each inflated state is followed by an inverse stress computation, which takes the deformed configuration as input to calculate the wall stress distribution. This generates the Cauchy stress history at each Gauss point in the structure. This stress will be used in the constitutive regression as the “experimental” stress.

In inverse stress computation, we also use the 8-fiber Holzapfel model with the assumed stiffness parameters. The strain energy function also takes the same form as forward 8-fiber Holzapfel shell model, written as

$$\psi_m = \sum_{I=1}^8 \frac{k_I}{8a} (\exp[a(\lambda_I^2 - 1)^2] - 1), \quad (5.10)$$

$$\lambda_I^2 = \mathbf{C} \cdot \mathbf{N}_I \otimes \mathbf{N}_I, \quad (I = 1, 2, \dots, 8).$$

The basic formulation of inverse 8-fiber Holzapfel shell model is discussed in §4.2.2.

In the inverse stress analysis, we set the effective stiffness parameters E_1 , E_2 and a as follows

$$E_1 = 8.2N/mm, \quad E_2 = 5.2N/mm, \quad a = 20. \quad (5.11)$$

The stress distribution will be showed in verification section, which also includes the stress insensitivity to material models.

Here one thing should be pointed out. In the inverse method, the stress resultant \mathbf{t} on each Gauss point is computed in a local orthonormal coordinate system $\bar{\mathbf{g}}_\alpha$, so the covariant metric tensor is $\bar{g}_{\alpha\beta} = \bar{\mathbf{g}}_\alpha \cdot \bar{\mathbf{g}}_\beta = \delta_{\alpha\beta}$, and the contravariant metric tensor is $\bar{g}^{\alpha\beta} = \delta^{\alpha\beta}$. Three types of base vectors will be used in PWIM, shown in Table 5.1.

Table 5.1: Convected and non-convected base vectors in three configurations.

	Referential	Convected	Non-convected
Configuration	Undeformed	Deformed(Forward)	Deformed(Inverse)
Base vectors	\mathbf{G}_α	\mathbf{g}_α	$\bar{\mathbf{g}}_\alpha$
Metric Tensor	$\mathbf{G}_{\alpha\beta} = \delta_{\alpha\beta}$	$\mathbf{g}_{\alpha\beta}$	$\bar{g}_{\alpha\beta} = \delta_{\alpha\beta}$

	Referential	Convected	Non-convected
Configuration	Undeformed	Deformed(Forward)	Deformed(Inverse)
Base vectors	\mathbf{A}_α	\mathbf{a}_α	$\bar{\mathbf{a}}_\alpha$
Metric Tensor	$\mathbf{A}_{\alpha\beta} = \delta_{\alpha\beta}$	$\mathbf{a}_{\alpha\beta}$	$\bar{a}_{\alpha\beta} = \delta_{\alpha\beta}$

The stress resultant tensor \mathbf{t} remains the same whether the bases are convected

or non-convected, so we get

$$\mathbf{t} = t^{\alpha\beta} \mathbf{g}_\alpha \otimes \mathbf{g}_\beta = \bar{t}^{\alpha\beta} \bar{\mathbf{g}}_\alpha \otimes \bar{\mathbf{g}}_\beta, \quad (5.12)$$

where $t^{\alpha\beta}$ and $\bar{t}^{\alpha\beta}$ are the stress tensor components under the convected base vectors \mathbf{g}^α and the non-convected base vectors $\bar{\mathbf{g}}^\alpha$, respectively. Contracting with $\mathbf{g}^\alpha \otimes \mathbf{g}^\beta$ on both sides of (5.13), we can get

$$t^{\alpha\beta} = (\mathbf{g}^\alpha \cdot \bar{\mathbf{g}}_\delta) \bar{t}^{\delta\gamma} (\mathbf{g}^\beta \cdot \bar{\mathbf{g}}_\gamma). \quad (5.13)$$

This is the transformation between the physical and the convected stress components.

5.2.4 Constitutive regression

In this numerical verification example, using $^{(i)}\mathbf{t}$ to represent the model stress resultant in the i -th configuration, $^{(i)}\mathbf{t}$ can be expressed as a function of the following variables,

$$^{(i)}\mathbf{t} = \mathbf{t}(E_1, E_2, a, \mathbf{a}, \mathbf{A}). \quad (5.14)$$

$^{(i)}\hat{\mathbf{t}}$ represents the “experimental” stress resultant obtained from the inverse shell computation. In this work, the object function is written as [99],

$$\Phi = \sum_{i=1}^N w_1 (^{(i)}t^{11} - ^{(i)}\hat{t}^{11})^2 + w_2 (^{(i)}t^{22} - ^{(i)}\hat{t}^{22})^2 + w_3 (^{(i)}t^{12} - ^{(i)}\hat{t}^{12})^2 \quad (5.15)$$

In this object function, w_1, w_2, w_3 are weight parameters, and are chosen according to the ratios among the inverse (experimental) stress components (i.e. $\frac{\hat{t}^{11}}{\hat{t}^{22}}$), to consider the influence of all the stress component on the objective function value and scale them to a similar order [99].

The regression problem can be described as

$$\begin{aligned} & \text{minimize} && \Phi(E_1, E_2, a), \\ & \text{subject to} && [E_1, E_2, a]^T \in [\mathbf{L.B.}, \mathbf{U.B.}] \end{aligned} \quad (5.16)$$

$\mathbf{L.B.}$ and $\mathbf{U.B.}$ are the lower and upper boundaries of the variables $[E_1, E_2, a]^T$.

In this optimization algorithm, the analytical gradients of the objective function with respect to the regression variables are required. The convected components of the stress tensor are already derived as

$$\tilde{t}^{\alpha\beta} = J^{-1} \sum_{I=1}^8 \frac{k_I}{2} (\exp[a(\lambda_I^2 - 1)^2] - 1)(\lambda_I^2 - 1)(N_I^p A_{pq} N_I^q)^{-1} N_I^\alpha N_I^\beta, \quad (5.17)$$

where $J^{-1} = 1/\det \mathbf{F}$. The gradient for SNOPT in this work is defined as $gobj(p_i) = \frac{\partial t^{\alpha\beta}}{\partial p_i}$, ($p_i = E_1, E_2, a$). The stress gradients can be presented as

$$\begin{aligned} gobj(E_1) &= \frac{\partial t^{\alpha\beta}}{\partial E_1} = \frac{\partial t^{\alpha\beta}}{\partial k_I} \frac{\partial k_I}{\partial E_1} = \\ &= \frac{J^{-1}}{24} \left(\sum_{I=1}^4 (\exp[a(\lambda_I^2 - 1)^2] - 1)(\lambda_I^2 - 1) N_I^\alpha N_I^\beta (20 - 9\sqrt{2} + 3(-2 + \sqrt{2})I) \right. \\ &\quad \left. + \sum_{I=5}^9 (\exp[a(\lambda_I^2 - 1)^2] - 1)(\lambda_I^2 - 1) N_I^\alpha N_I^\beta (-40 + 21\sqrt{2} - 3(-2 + \sqrt{2})I) \right). \end{aligned} \quad (5.18)$$

$gobj(E_2)$ can be computed using same way

$$\begin{aligned} gobj(E_2) &= \frac{\partial t^{\alpha\beta}}{\partial E_2} = \frac{\partial t^{\alpha\beta}}{\partial k_I} \frac{\partial k_I}{\partial E_2} = \\ &= \frac{J^{-1}}{24} \left(\sum_{I=1}^4 (\exp[a(\lambda_I^2 - 1)^2] - 1)(\lambda_I^2 - 1) N_I^\alpha N_I^\beta (-16 + 9\sqrt{2} - 3(-2 + \sqrt{2})I) \right. \\ &\quad \left. + \sum_{I=5}^9 (\exp[a(\lambda_I^2 - 1)^2] - 1)(\lambda_I^2 - 1) N_I^\alpha N_I^\beta (44 - 21\sqrt{2} + 3(-2 + \sqrt{2})I) \right). \end{aligned} \quad (5.19)$$

$gobj(a)$ is given as follow

$$gobj(a) = \frac{\partial t^{\alpha\beta}}{\partial a} = J^{-1} \sum_{I=1}^8 \frac{k_I}{2} (\exp[a(\lambda_I^2 - 1)^2]) (\lambda_I^2 - 1)^3 N_I^\alpha N_I^\beta, \quad (5.20)$$

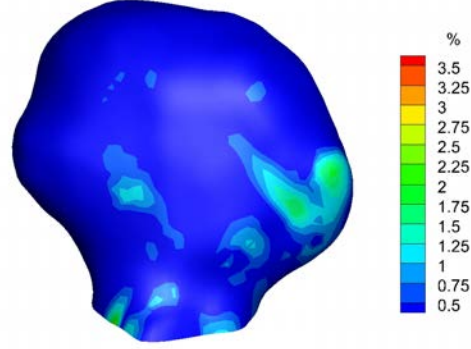


Figure 5.6: Percentage difference in von Mises stress between baseline and stiffer 8-fiber Holzapfel material models.

5.2.5 Stress insensitivity of inverse stress

Since the fundamental premise in the method design is that the inversely computed stress is insensitive to material model or parameters used to perform the analysis, it is important to verify the stress sensitivity before moving further in the analysis. In order to verify the stress insensitivity to material model, we also choose two sets of material parameters for 8-fiber Holzapfel material model: the baseline and the stiffer material models.

For the 8-fiber Holzapfel material model, we set baseline parameters and elevated stiffness parameters, respectively,

$$\begin{aligned}
 \text{Baseline parameters :} \quad & E_1 = 8.2N/mm, \quad E_2 = 5.2N/mm, \quad a = 20; \\
 \text{Elevated stiffness parameters :} \quad & E_1 = 82N/mm, \quad E_2 = 52N/mm, \quad a = 36.
 \end{aligned}
 \tag{5.21}$$

We compare the stress differences $diff = \frac{|\sigma_{baseline} - \sigma_{stiffer}|}{|\sigma_{baseline}|} \times 100\%$. Figure 5.6

shows the stress differences between the baseline and stiffer 8-fiber Holzapfel material models. From Figure 5.6, we can find that the von Mises stresses differences computed by using baseline and stiffer 8-fiber Holzapfel material model are less than 5% for the whole model; and except the artery boundaries, the stress differences in the aneurysm regions are less than 3%, most part even lower than 1%. From this comparison, we can conclude that, the inverse stress depends insensitively on the material models. This is important for pointwise identification method. Because of lack of information, it's unavoidable to use assumed model or parameters to compute the "experimental" stress. Results here indicates that, although different kinds of material models we use in the inverse stress computation, the predicted stress distributions stay close.

From the stress comparison figure, we can find that the largest differences happen near the artery boundary, and in the sac the stress differences are quite small. This can be understood as the boundary effects. So in the identification step, we only computed the sac areas and avoid the boundary region.

The bending factor α (defined as $\alpha = \frac{\text{bending stress}}{\text{membrane stress} \times \text{thickness}}$) in inverse method with baseline model. From Figure 5.7, we can find that the maximum bending factor is less than 0.05; in most regions, the bending factors are less than 0.01. In this case, in which the membrane stress is much larger than bending, we can omit the bending effects and use the membrane results to carry out the constitutive regression.

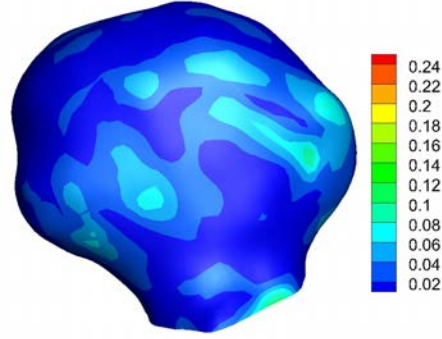


Figure 5.7: Distribution of bending factor α .

5.2.6 Distribution of the identified parameters

Parameters regression is conducted at each Gauss point. The figures here are the results we further project to corresponding nodes. Figure 5.8 shows the distribution of identified stiffness parameters E_1 , E_2 and a . To evaluate the the accurate of the identified stiffness parameters, the relative error between the identified and assumed stiffness parameters are also calculated. We define $error = \frac{|p - \hat{p}|}{|\hat{p}|} \times 100\%$, ($p = E_1, E_2, a$), and p and \hat{p} indicate the identified and assumed values, respectively. In Figure 5.8, we show the distribution of the identification error for E_1, E_2, a .

To quantify the identification error, the maximums, minimum and mean relative errors are calculated in Table 5.2.

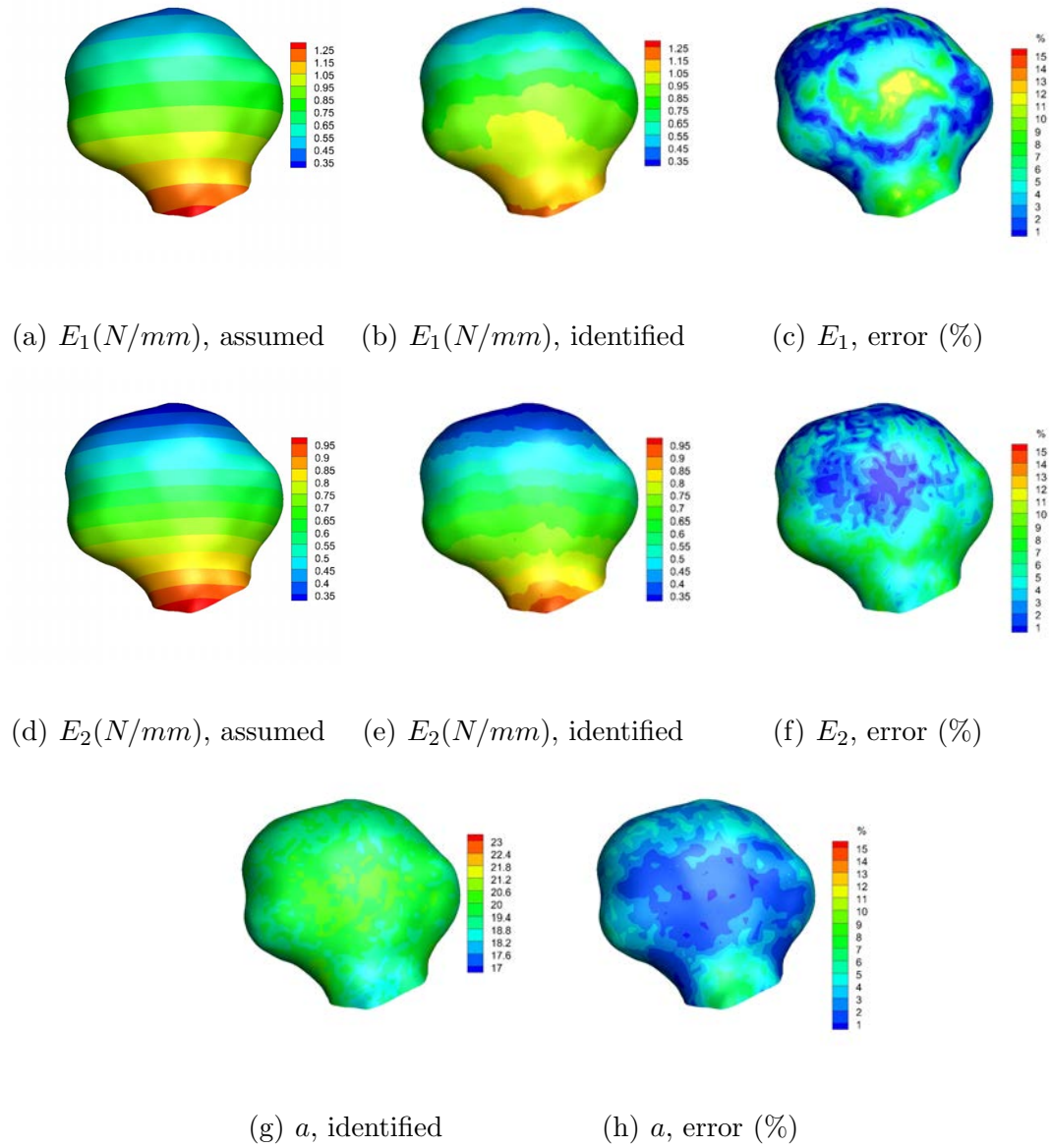
Figure 5.8: PWIM result for *CASE I*.

Table 5.2: Maximum, minimum and mean errors of the identified parameters in the identification region.

Error %	E_1	E_2	a
Maximum (%)	10.11	8.56	8.68
Minimum (%)	0.001	0.003	0.001
Mean (%)	4.16	3.85	2.85

5.2.7 Forward predictability validation

We further assess the accuracy of the predictability of the identified parameters using a forward analysis. We choose a new pressure state (120 mmHg), which is not used in the regression, to conduct the forward analysis with both identified and assumed material parameters. For the artery boundary regions, which are excluded in the identification, we just use the assumed material parameters. Identified parameters are applied to the rest of the aneurysm wall. Figure 5.9 presents the distribution of mid-surface displacement differences between two sets of material parameters' analysis. The displacement difference here is defined as $\frac{\|\mathbf{u}-\hat{\mathbf{u}}\|}{\|\hat{\mathbf{u}}\|} \times 100\%$, where \mathbf{u} and $\hat{\mathbf{u}}$ are vectors and represent the displacement computed by using identified and assumed parameters, respectively. From Figure 5.9 we can find that, the maximum differences is 0.8%, and in most regions, 0.2%–0.4%.

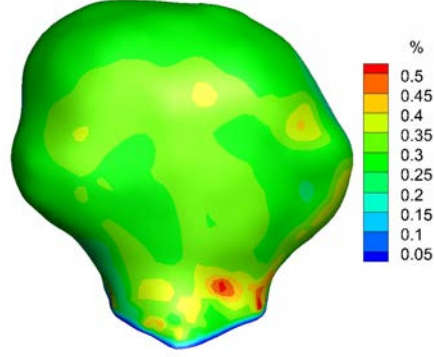


Figure 5.9: Distribution of displacement differences between two sets of material parameters' analysis (%).

5.3 Discussion

In this chapter, we used the cerebral aneurysm as an numerical experiments to conduct the pointwise identification method. The aneurysm wall is described as elastic shell and thus, concave surfaces are permitted. This eliminates the limitation of membrane structure and allows for realistic aneurysms to be considered.

In this chapter we first show that inverse stresses stay close between isotropic and anisotropic material models. We testify that the inverse stress is material insensitive, which can ensure that the inversely computed stress distribution be a good approximation to the actual stress. By using PWIM, we obtain the identified material stiffness parameters, whose errors compared to the assumed parameters are less than 7%. The assumed heterogeneous parameters distribution are also recovered. In the optimization procedure, sometimes, different combination of material parameters

can give equally satisfactory fit. Therefore , it's possible that we obtain a set of parameters that are not the true minimizer. To evaluate the effective of the identified parameters, one of the possible way is to test the predictability of the identified parameters. In our analysis, the displacement computed by forward analysis with both sets of material parameter stay close; the errors are less than 0.4%.

CHAPTER 6

APPLICABILITY OF PWIM IN CEREBRAL ANEURYSMS

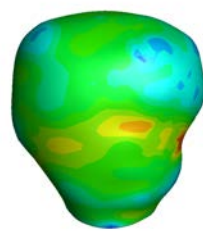
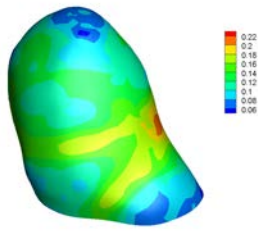
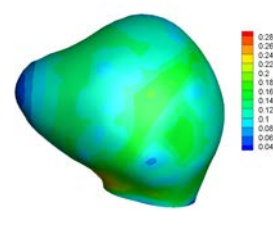
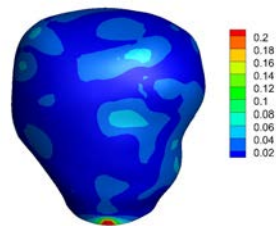
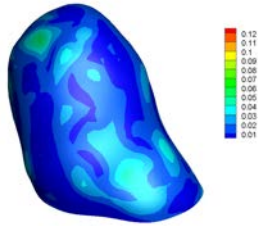
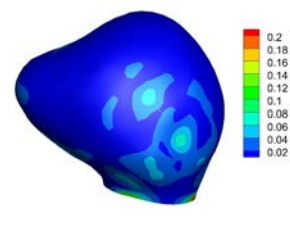
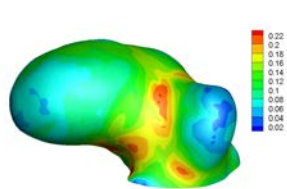
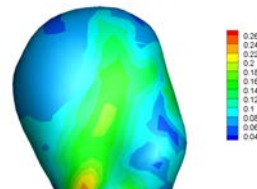
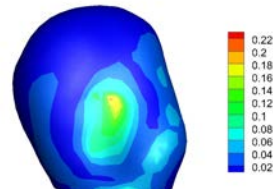
6.1 The applicability study

6.1.1 Method

The shell PWIM is applied to a group of selected typical realistic cerebral aneurysms. There are many kinds of geometrical structures in realistic cerebral aneurysms, and PWIM may not apply to some types and thus it is important to evaluate the method against a wide range of geometric features. Five other representative aneurysms are selected in the study. They include a saddle-like aneurysm, saccular geometries with small blebs, large concavity, saccular with daughter aneurysms. The same shell PWIM method is applied on these cerebral aneurysm models, including the boundary condition, fiber orientation, deformed states, pressure, etc.

Figure 6.1 shows the von Mises stresses and bending factor (defined as $\alpha = \frac{\text{bending stress}}{\text{membrane stress} \times \text{shell thickness}}$) in five cerebral aneurysms. For all cases, the bending stress is much smaller than the membrane stress, in most regions the bending factors are smaller than 0.02. The smaller bending factors means the membrane stress plays the domination role, and thus PWIM can be applied.

The analysis follows the same procedure described in the Chapter §5. The stiffness parameters E_1 and E_2 are also assumed as to decrease with respect to the height from the basal plane. Four different types of heterogeneities are assumed, and the property distributions. The assumed heterogeneities can be found in Figure

(a) *Case II, stress*(b) *Case III, stress*(c) *Case IV, stress*(d) *Case II, α* (e) *Case III, α* (f) *Case IV, α* (g) *Case V, stress*(h) *Case VI, stress*(i) *Case V, α* (j) *Case VI, α* Figure 6.1: Von Mises stress (N/mm^2) and bending factors.

5.8-Figure 6.6. The material constant a is kept homogeneous and is set to 20.

6.1.2 Pointwise identification results

Figure 5.8-Figure 6.6 show the distributions of identification results, including the identification errors, for five cerebral aneurysms. Errors are defined as $error = \frac{|p - \hat{p}|}{|\hat{p}|} \times 100\%$, and p and \hat{p} indicate the identified and assumed values, respectively. For *II*, *III*, (Figure 6.2-Figure 6.3), the continuously linear distributions are recovered, and the relative identification error is in an acceptable range. Take *CASE II* as example, the maximum identification error is less than 12%, 13%, 11% for E_1 , E_2 and a , respectively; the mean identification error is 3.76%, 3.96%, 3.27% for E_1 , E_2 and a , respectively.

Other types of distributions are considered in *CASE IV*, *V* and *VI*. The distribution of identified material stiffness in all cases also recover the assigned distributions.

The maximum, minimum and mean identification errors for five cases are shown in Table 6.1. In Table 6.1, we can find that in whole five cerebral aneurysm cases, the mean identification errors are less than 5%, most of them are around 3%; the maximum identification errors are less than 13.5%.

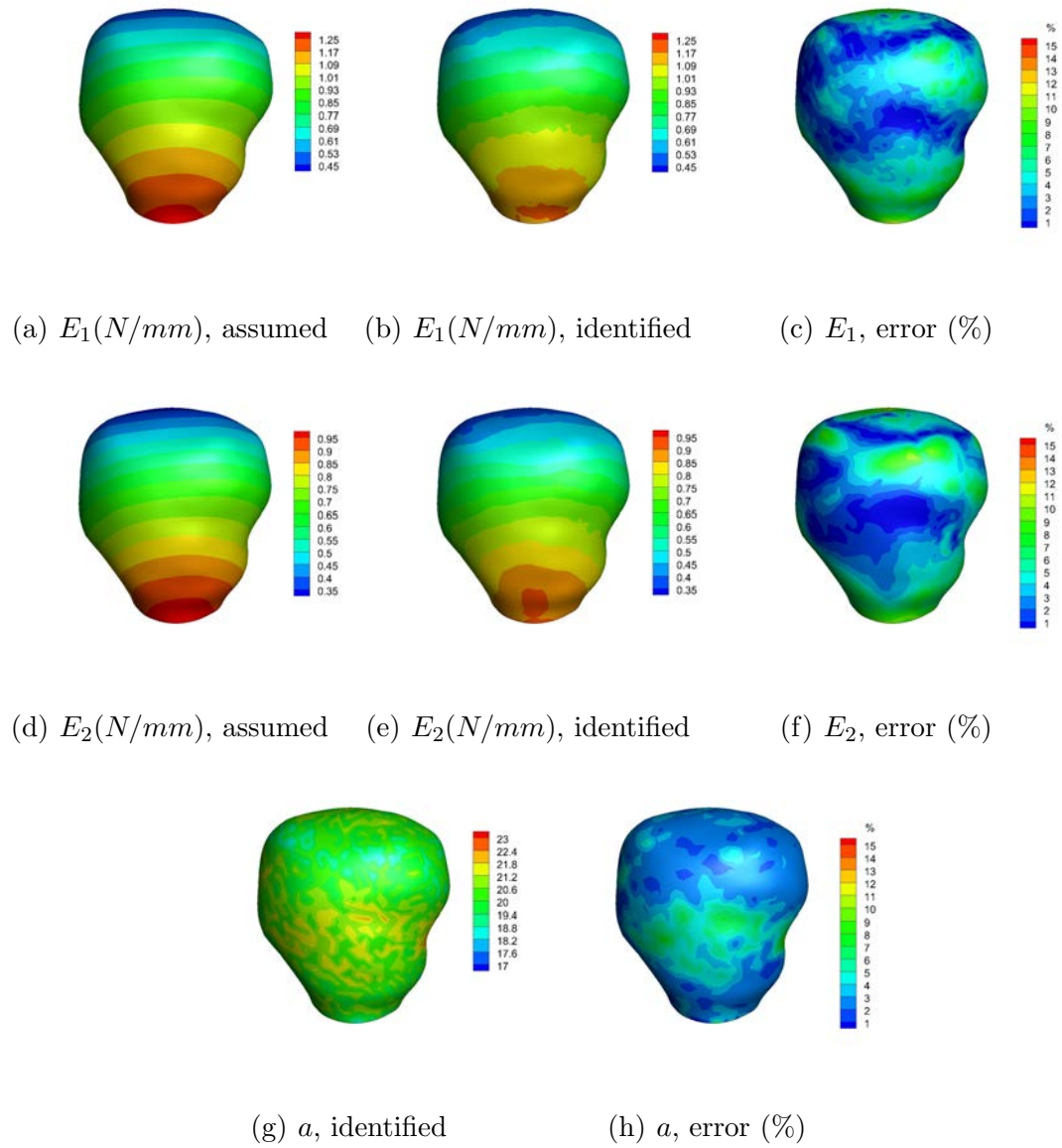


Figure 6.2: PWIM result for *CASE II*. (The maximum strain is 0.06).

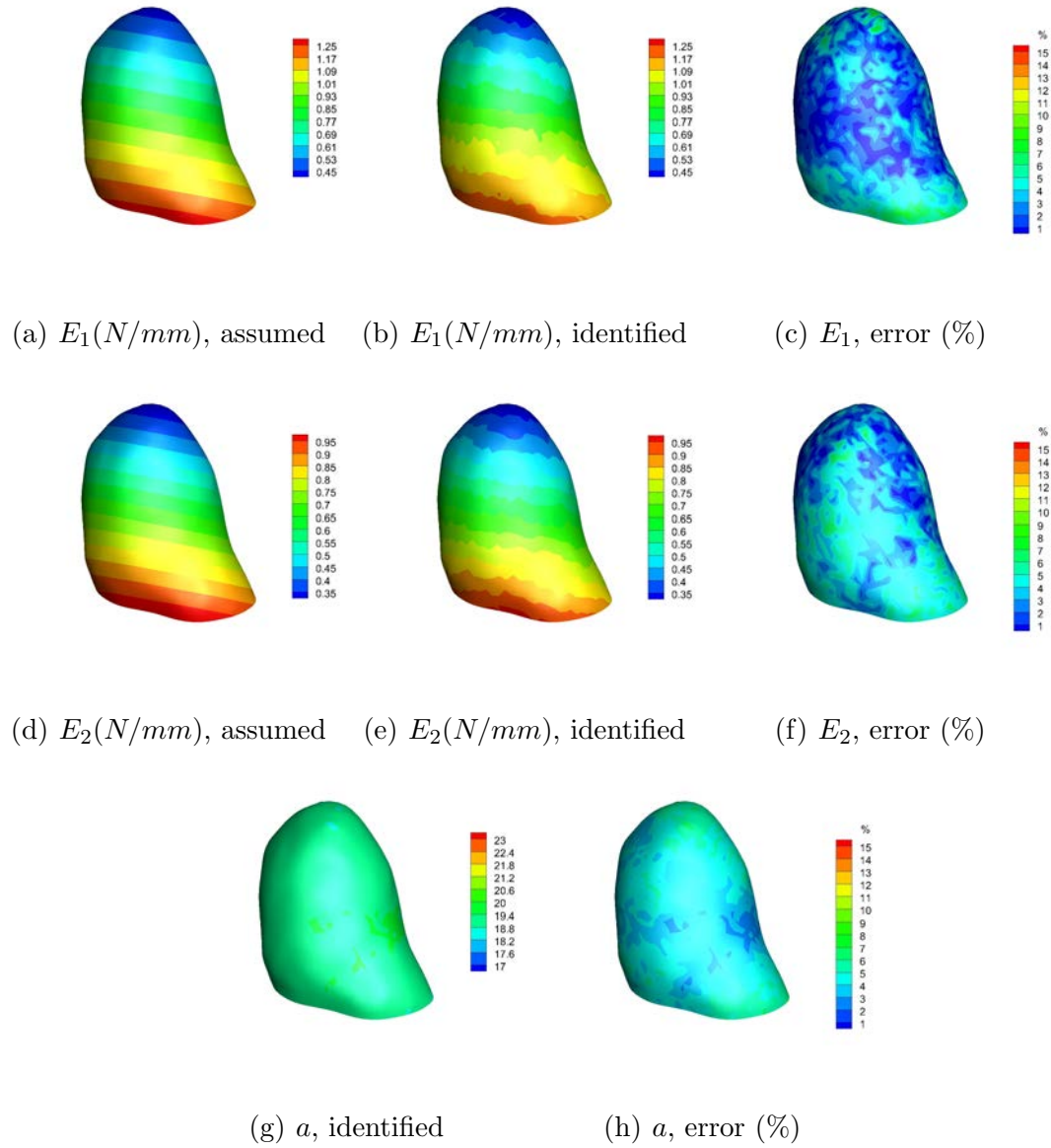


Figure 6.3: PWIM result for *CASE III*. (The maximum strain is 0.06).

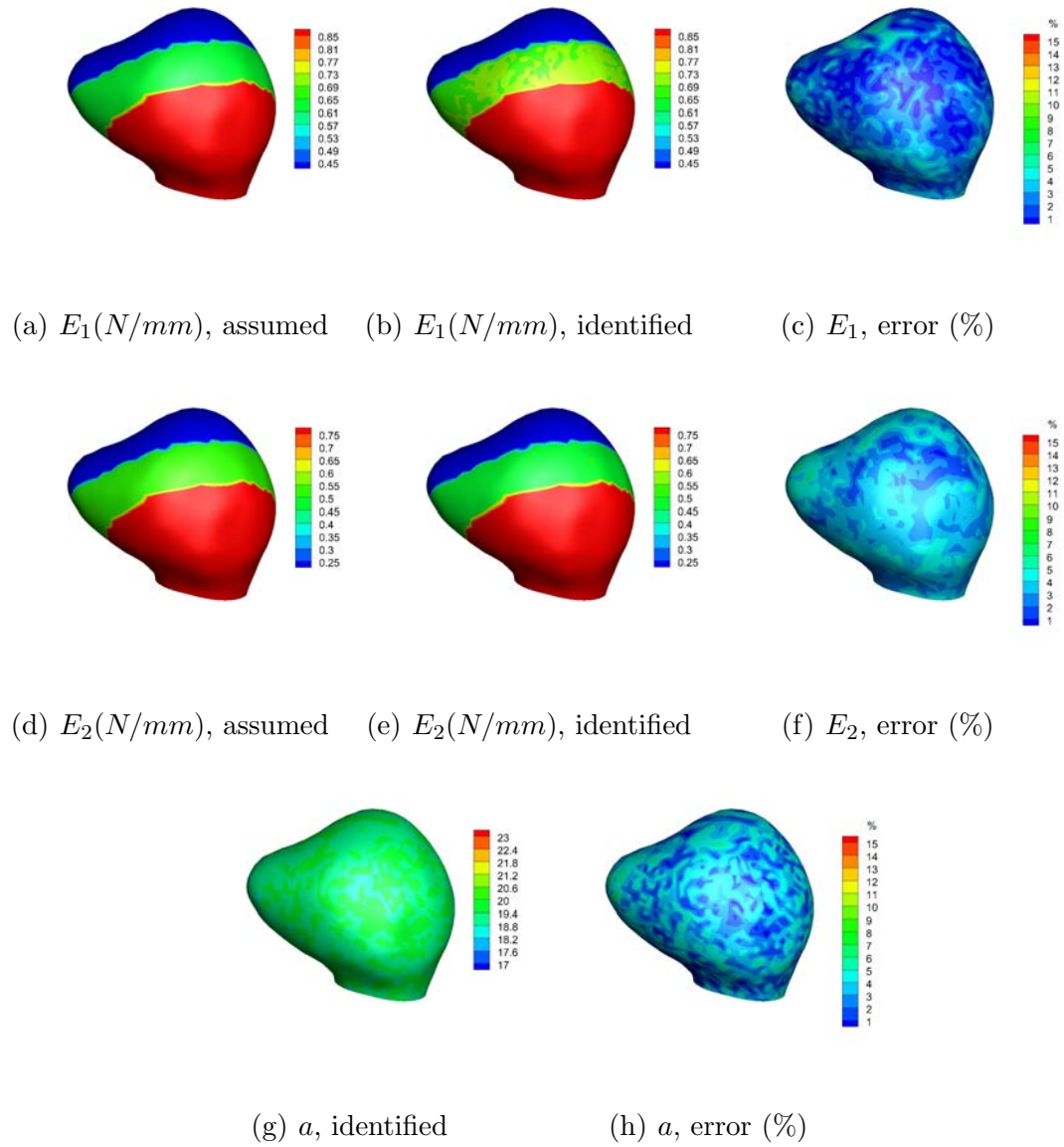


Figure 6.4: PWIM result for *CASE IV*. (The maximum strain is 0.09).

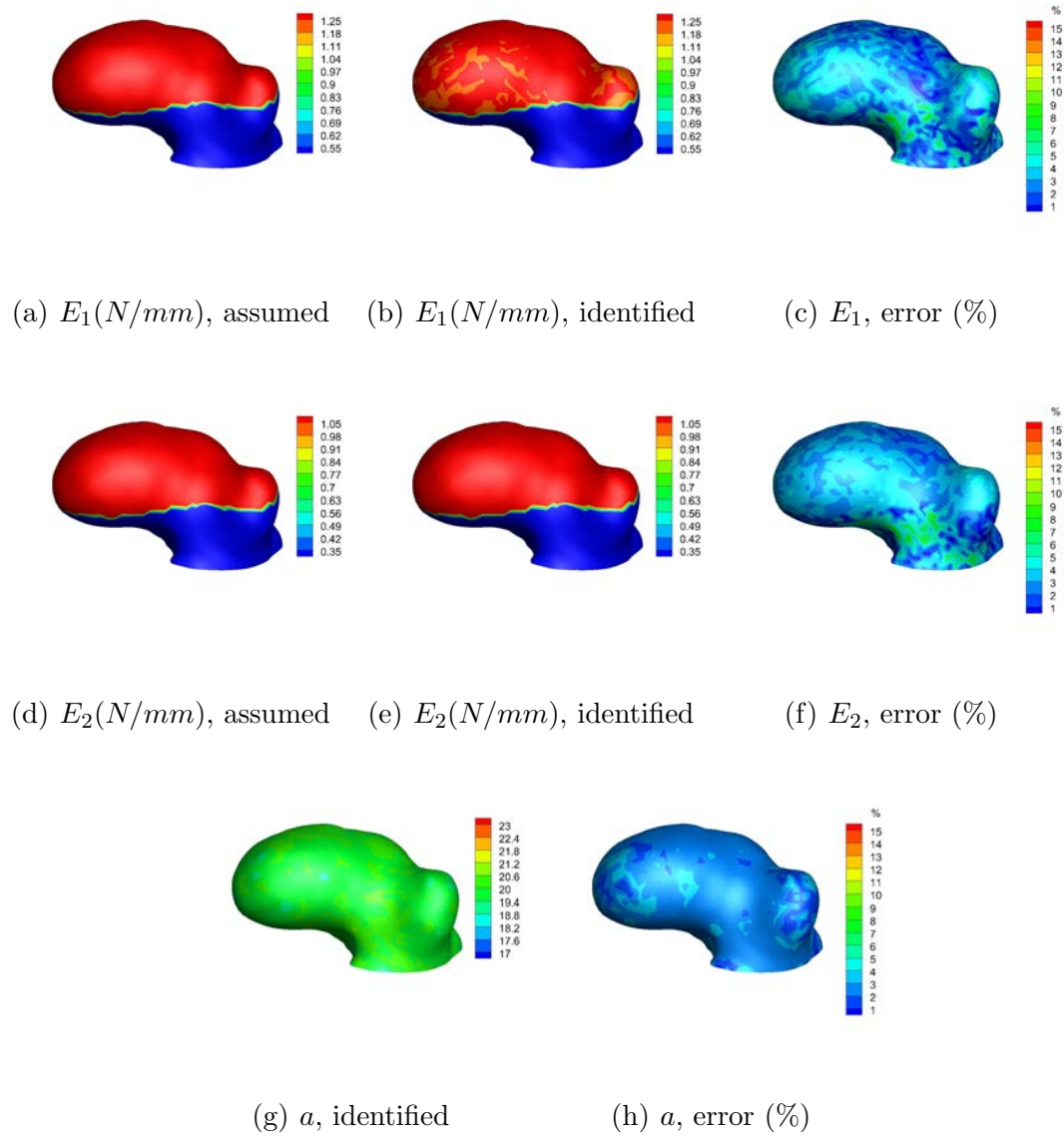


Figure 6.5: PWIM result for CASE V. (The maximum strain is 0.05).

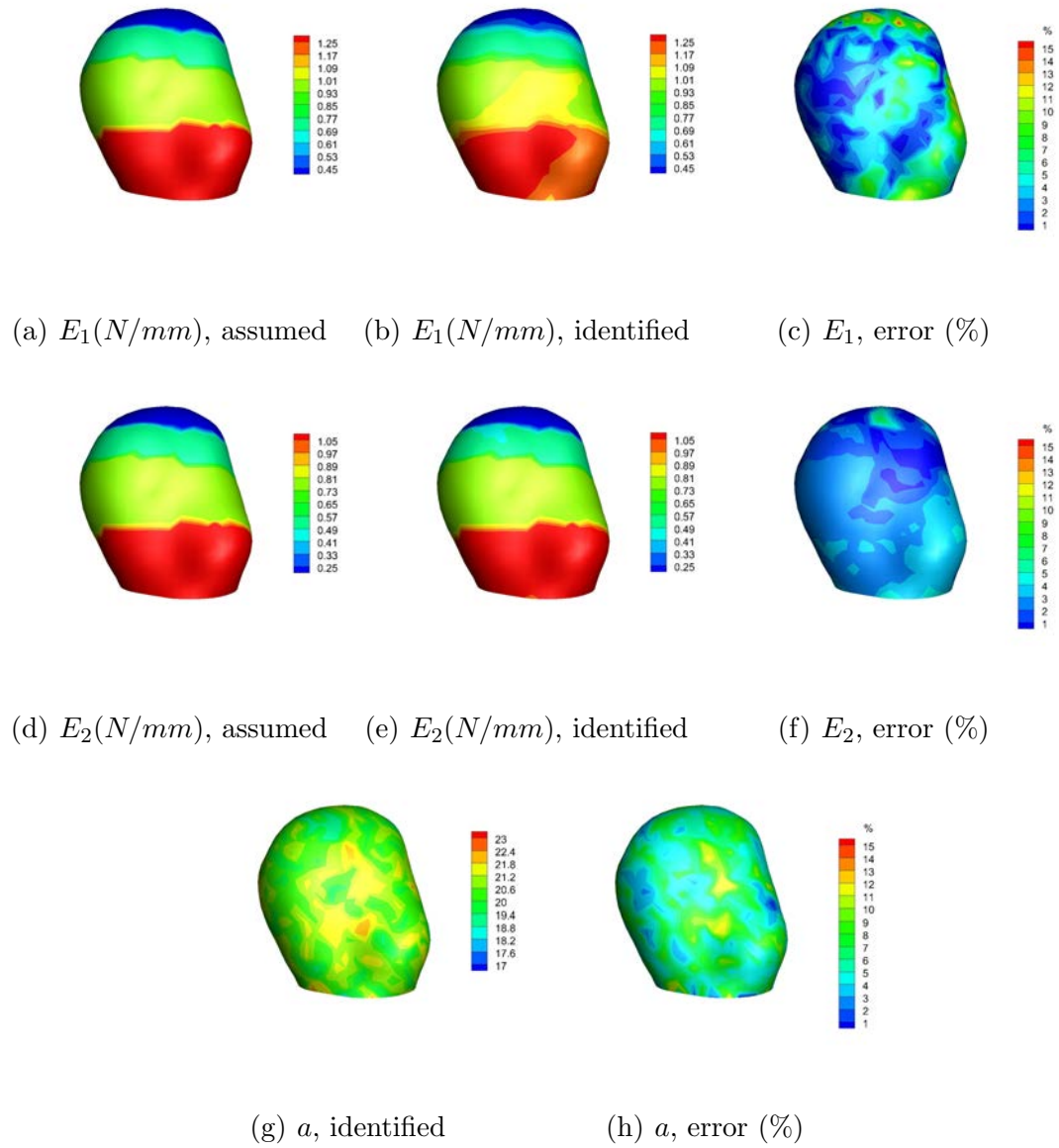


Figure 6.6: PWIM result for *CASE VI*. (The maximum strain is 0.07).

Table 6.1: Statistics of the identification errors (%) of five cases.

<i>CASE</i>	Minimum			Maximum			Mean		
	E_1	E_2	a	E_1	E_2	a	E_1	E_2	a
II	0.004	0.003	0.001	12.09	13.40	11.39	3.76	3.96	3.27
III	0.005	0.001	0.43	10.73	9.50	6.56	2.7	3.23	3.26
IV	0.001	0.004	0.01	9.71	10.19	7.44	2.13	3.23	3.17
V	0.002	0.001	0.02	9.51	11.69	6.01	2.96	3.10	2.36
VI	0.003	0.002	0.01	9.01	7.95	6.81	2.35	2.21	3.30

6.2 Unknown fiber direction

6.2.1 Identification results

The material model used in the study, presented in Section 6.1.2, is an orthotropic material for which the symmetric axes are specified by two vectors \mathbf{N}_1 and \mathbf{N}_5 called the principal fiber directions. In the previous section, we assume that the fiber directions, are known during parameter identification. Given that in reality the fiber directions (in fact, the symmetry type as well) are not known, we include the fiber orientation as a regression variable in this section.

In the forward analyses, the fiber directions are set up as follows. The first principal fiber (k_1) direction \mathbf{N}_1 in the reference configuration is assumed to be parallel to the basal (x-y) plane, and tangent to the aneurysm surface at each point. The second principal fiber (k_5) direction \mathbf{N}_5 is perpendicular to \mathbf{N}_1 and also tangent to the surface. Thus, the fiber directions are uniquely determined at every Gauss point. The fiber \mathbf{N}_1 (η'_1 in Figure 6.7) is parameterized by the angle θ that it makes to a local basis η_1 which is tangent to the surface. The local basis is generated from the

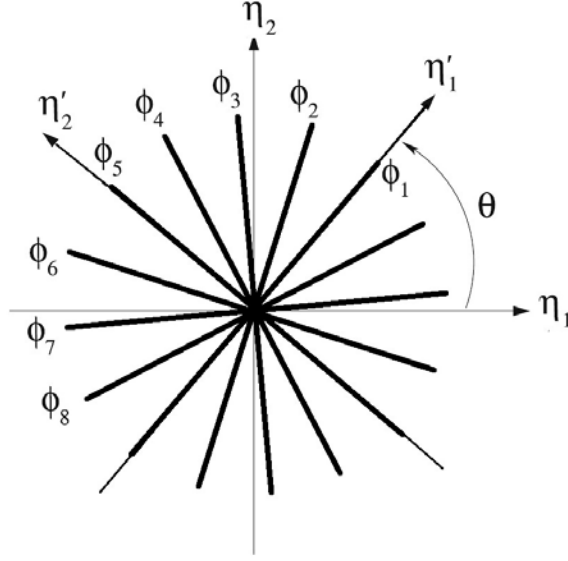


Figure 6.7: Schematic illustration of uniformly distributed collagen fibers (Reproduced from [42]).

finite element natural coordinates and every Gauss point, and is recorded. The angle is defined by

$$\theta = \arccos \frac{N_1^1}{\|\mathbf{N}_1\|}. \quad (6.1)$$

The angles of other fibers can be calculated from $\theta_I = \theta + \frac{I-1}{8}\pi$, $I = 1, 2, \dots, 8$.

In the inverse stress computation, we use the assigned fiber direction. It would be more realistic if a different fiber assumption were employed; however, given the premise that the inverse stress solution is insensitive to the material model, the assignment of symmetry does not matter much in this step.

In the regression, the angle θ is assumed unknown and is estimated from the strain-stress data regression, along with other parameters. In this case, the objective

function in Eq. (5.2) can be written as $\Phi = \Phi(\mu_1, \dots, \mu_x, \theta)$, which not only includes the material stiffness parameters and also the angle that defines the first principal fiber direction.

We carry out the identification for *CASE III* and *CASE V*. The identified stiffness parameter and identification errors of *CASE III* are shown in Figure 6.8. From the distributions of identified stiffness parameters, we can find that the prescribed linear distribution is recovered. The the mean identification error is 9.5%, 6.4%, 5.9% for E_1, E_2 and a , respectively; the maximum identification error is less than 30.5%, 26.3%, 11.5% for E_1, E_2 and a , respectively. The maximum identification occurs only on boundary and some scatter spots, and in most regions the identification errors are relative small. Comparing the case of known fiber direction (Figure 6.3), the maximum and mean errors are elevated. For *CASE V*, the identification results are shown in Figure 6.9, the mean identification error is 6.4%, 5.1%, 3.9% for E_1, E_2 and a , respectively; the maximum identification error is 18.8%, 13.6%, 10% for E_1, E_2 and a , respectively. Again, the identification errors are elevated by introducing fiber direction into constitutive regression for both cases. It is anticipated because with more parameters in regression, the accuracy of identification is compromised.

Figure 6.10 and Figure 6.10 show the fiber directions on Gaussian points for *CASE III* and *CASE V*, respectively. The red dots represent the Gaussian points; the blue line and red line represent the assumed fiber directions and identified fiber directions, respectively. In most regions of both comparison figures, the identified fiber directions agree very well the assume ones (e.g. the regions of blue line and red

lines overlap).

6.2.2 Predictability of the identified parameters

The predictability of the identified parameters are assessed using forward analysis under 120 mmHg pressure. We run a forward analysis using the identified parameters and fiber angle, and compare the nodal displacement from another analysis using the assumed parameter and fiber orientation. Figure 6.12 and Figure 6.13 show percentage differences in nodal displacements for *CASE III* and *CASE V*, respectively. The percentage difference is defined as $\frac{\|\mathbf{u}-\hat{\mathbf{u}}\|}{\|\hat{\mathbf{u}}\|} \times 100\%$, where \mathbf{u} and $\hat{\mathbf{u}}$ are vectors and represent the displacement computed by using identified and assumed parameters, respectively. The difference is computed at every nodes, and interpolated to generate the contour plots. In *CASE III*, the maximum and mean displacement errors are 1.75% and 0.52%, respectively. In overall, the difference is very small. The “high” error only occurs in an isolated spot; the displacement error in most surface regions are less than 1%. In *CASE V*, the maximum and mean displacement errors are 1.96% and 0.36%, respectively. The maximum displacement error occurs on two scattered spots near the boundary, the displacement error in most regions are less than 0.6%. The identified parameters, despite a maximum of 30% of local difference to the assigned parameters, appears to yield to good predictability.

6.3 Influence of noise in motion data

In the application of PWIM in the living tissues, the deformed configurations are usually segmented from the medical images. It is unavoidable that the deformed

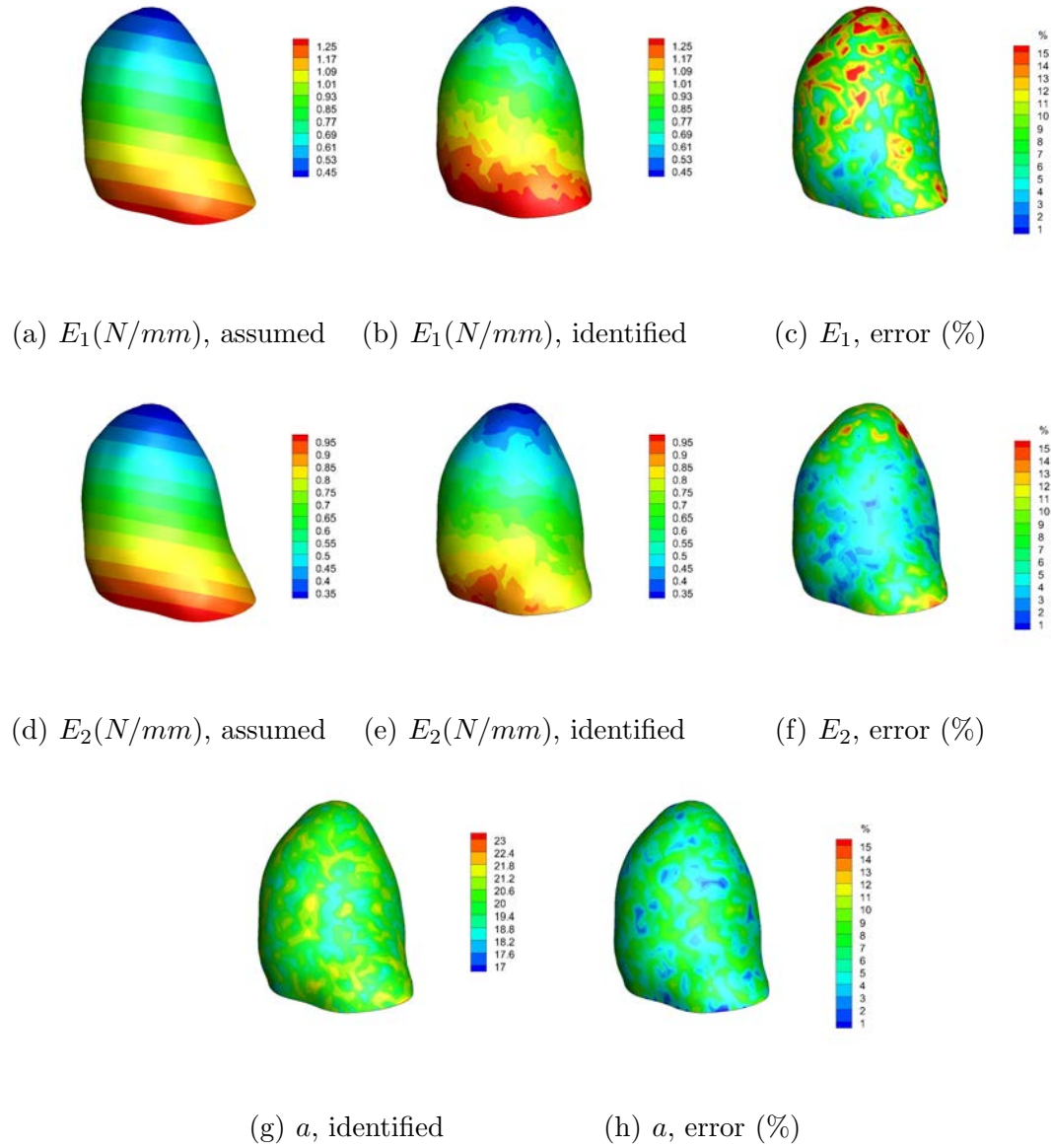


Figure 6.8: PWIM result for *CASE III* without knowing the first fiber direction.

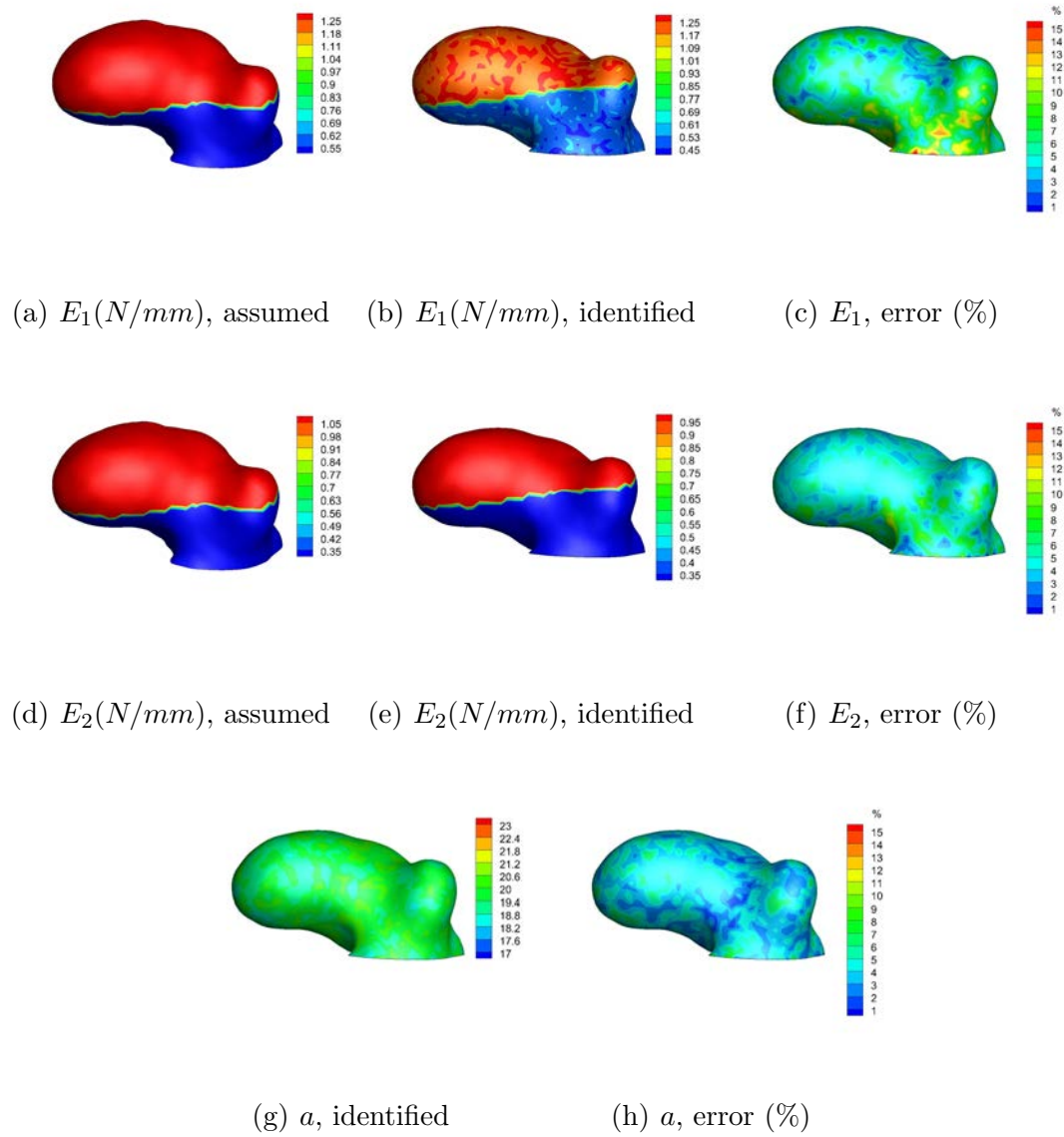


Figure 6.9: PWIM result for *CASE V* without knowing the first fiber direction.

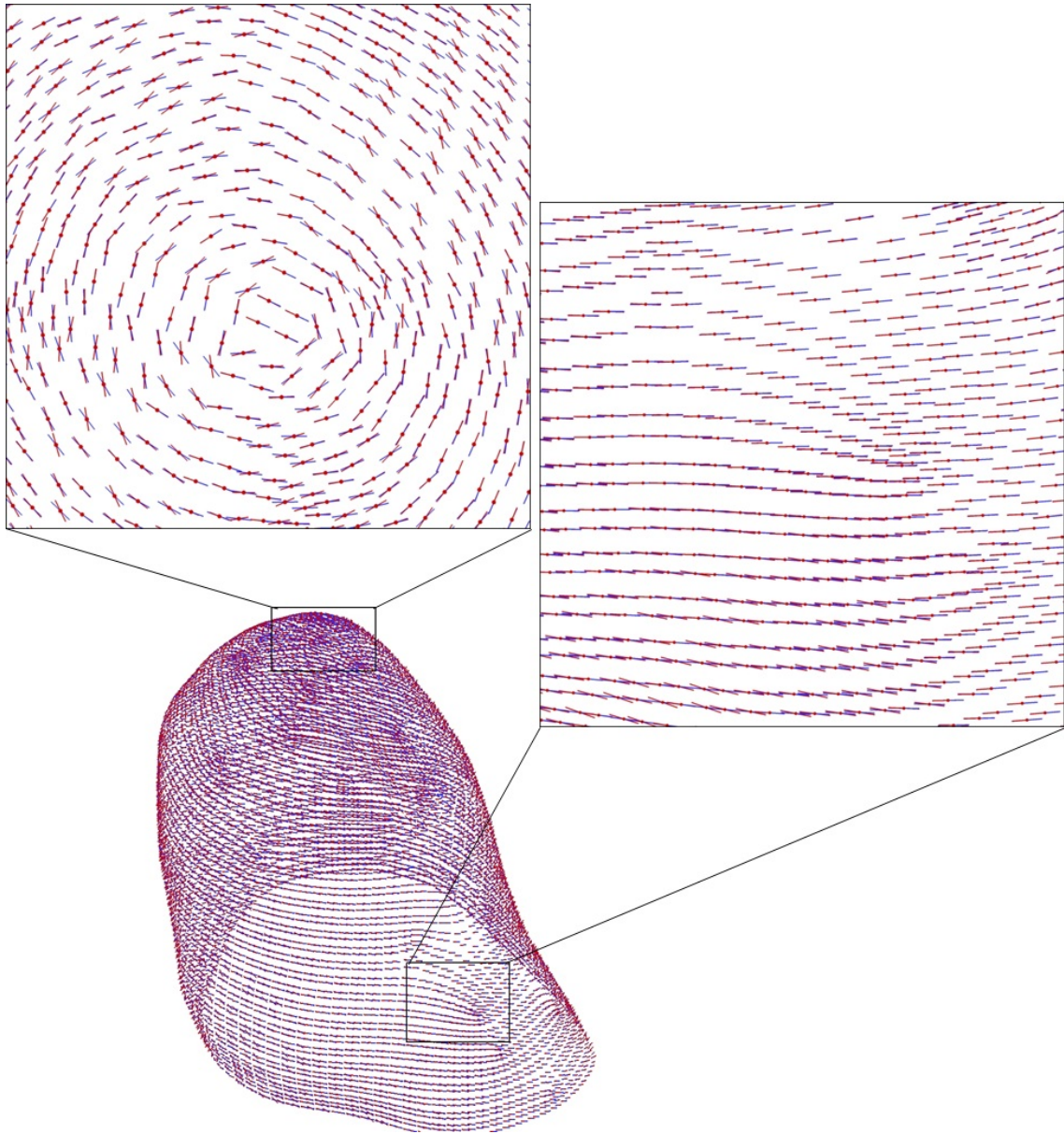


Figure 6.10: Fiber direction (\mathbf{N}_1) on Gauss points (red dots), *CASE III*. Red line: identified fiber direction; Blue line: assumed fiber direction.

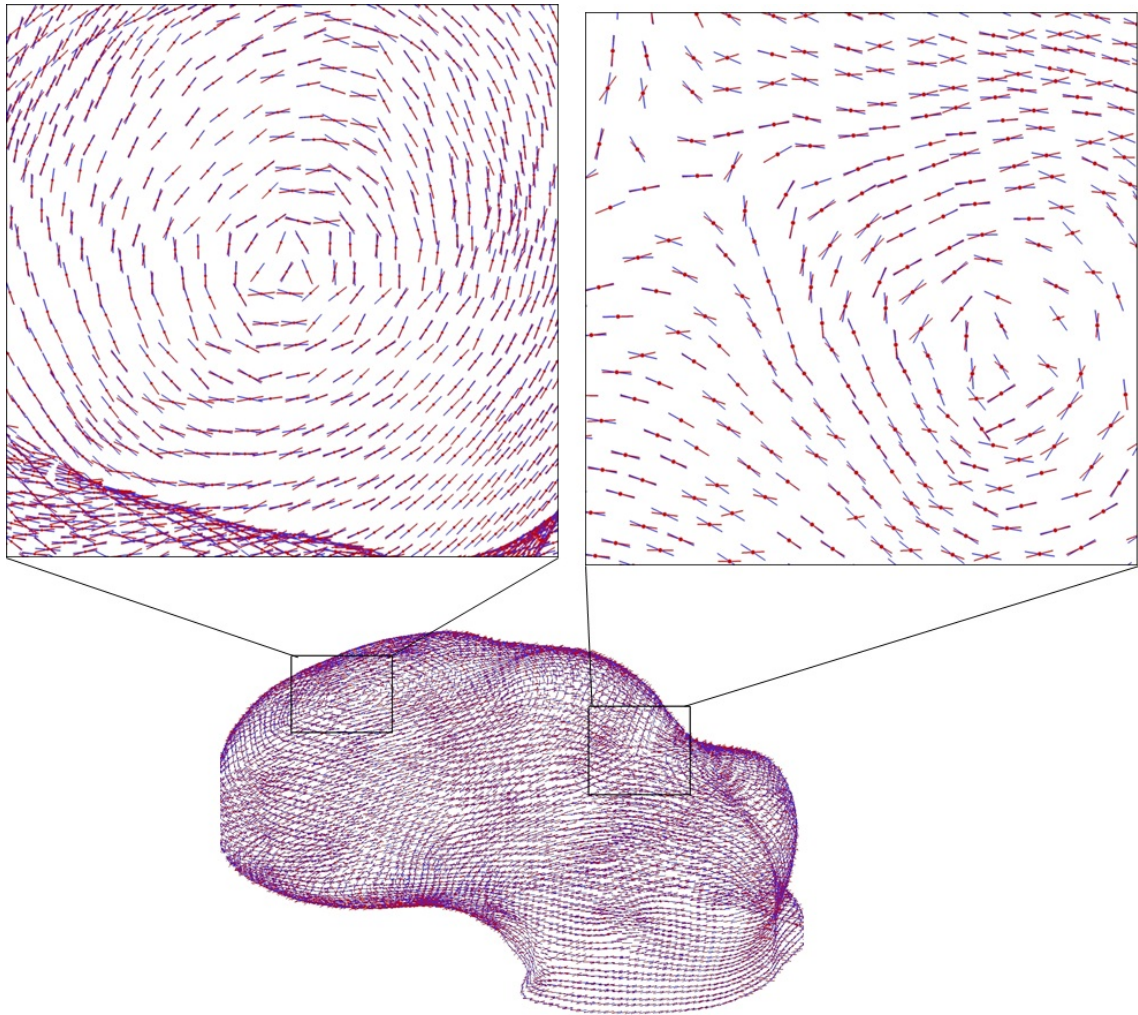


Figure 6.11: Fiber direction (\mathbf{N}_1) on Gauss points (red dots), *CASE V*. Red line: identified fiber direction; Blue line: assumed fiber direction.

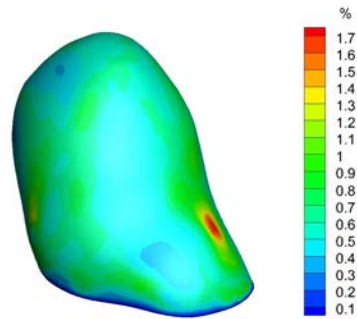


Figure 6.12: Percentage difference in nodal displacement, *CASE III*.

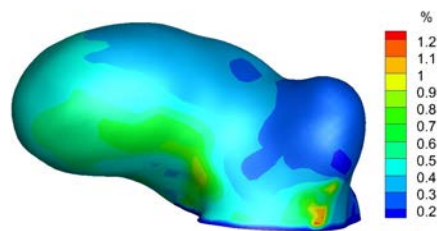


Figure 6.13: Percentage difference in nodal displacement, *CASE V*.

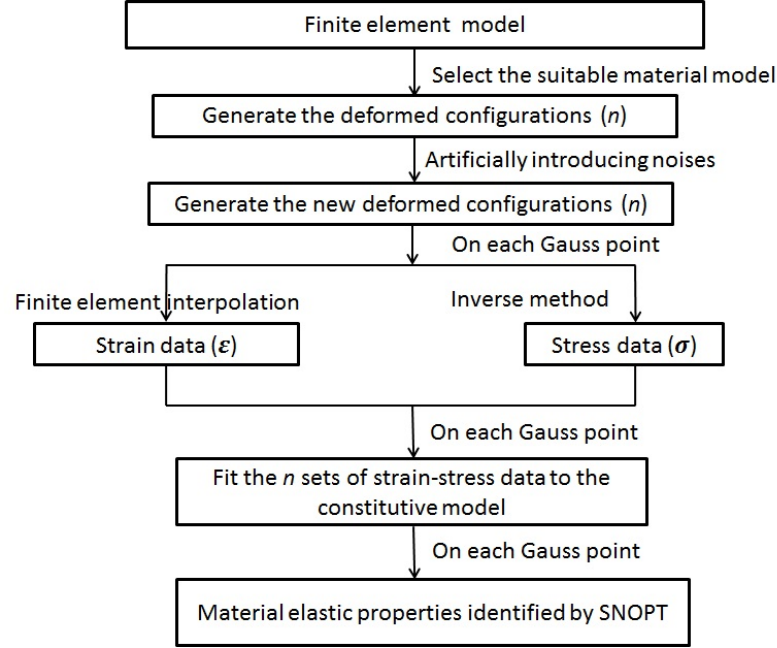


Figure 6.14: Method to evaluate the stability of PWIM.

configurations contain geometric errors resulting from both the image and segmentation/reconstruction. To further evaluate the method, it is imperative to investigate the robustness of the method under noise. In this section, numerical noise will be added to the nodal positions prior to the inverse analysis.

6.3.1 Method

Random perturbations to the nodal positions in deformed configurations will be added to simulate the errors generated during medical image reconstruction. The perturbed configurations are used in the inverse phase of analysis (both stress/strain analysis and regression). The accuracy of identified parameters are examined under different noise levels.

The procedure is showed in Figure 6.14. Random vectors $\boldsymbol{\vartheta} = (\delta x, \delta y, \delta z)$ will be generate through MATLAB, and the norm of vectors, Δ (defined as $\Delta = \|\boldsymbol{\vartheta}\|$) will be scaled down to a small magnitude (e.g. 1% or 2%). On each deformed configuration, the nodal displacements \mathbf{u} are perturbed to $\mathbf{u}' = \mathbf{u} + \boldsymbol{\vartheta} \cdot \|\mathbf{u}\|$, The perturbed displacements are used in the inverse stress analysis and strain computation. Material parameters are identified from these perturbed stress and strain data.

6.3.2 Identification results

We use the *CASE II*, discussed in last section, as a test case to investigate the capability of shell PWIM when the noises exist in displacement data. We keep all the information (e.g. assumed material heterogeneity, boundary condition, fiber orientation and deformed states number) the same as we used in Chapter §6.1.2, except that the geometry of each deformed configuration is polluted with noise.

Figure 6.15 and Figure 6.16 show the identification result when Δ is 1% and 2%, respectively. From Figure 6.15 and Figure 6.16, we can find that the material heterogeneity are recovered in most regions. With 1% perturbation error, the mean identification error is 6.38%, 4.37%, 7.15% for E_1, E_2 and a , respectively; the maximum identification error is less than 15.27%, 17.9%, 15.66% for E_1, E_2 and a , respectively. In Figure 6.16, when the perturbation error is 2%, the mean identification error is 13.9%, 14.1%, 8.6% for E_1, E_2 and a , respectively; the maximum identification error is less than 37.8%, 71%, 66.1% for E_1, E_2 and a , respectively. It is evident the higher the noise level, the lower the accuracy.

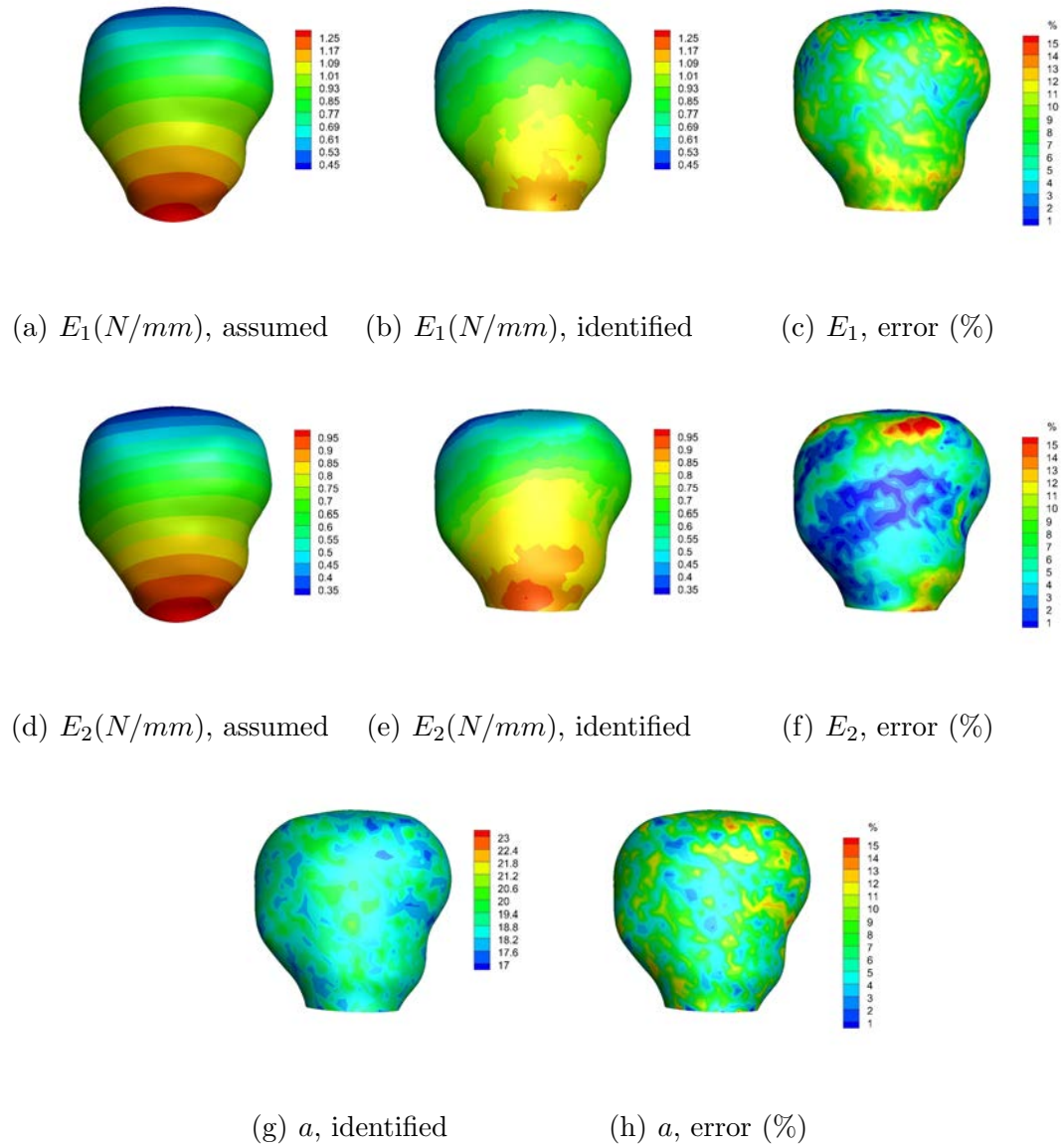


Figure 6.15: Identification result for *CASE II* under 1% of perturbation.

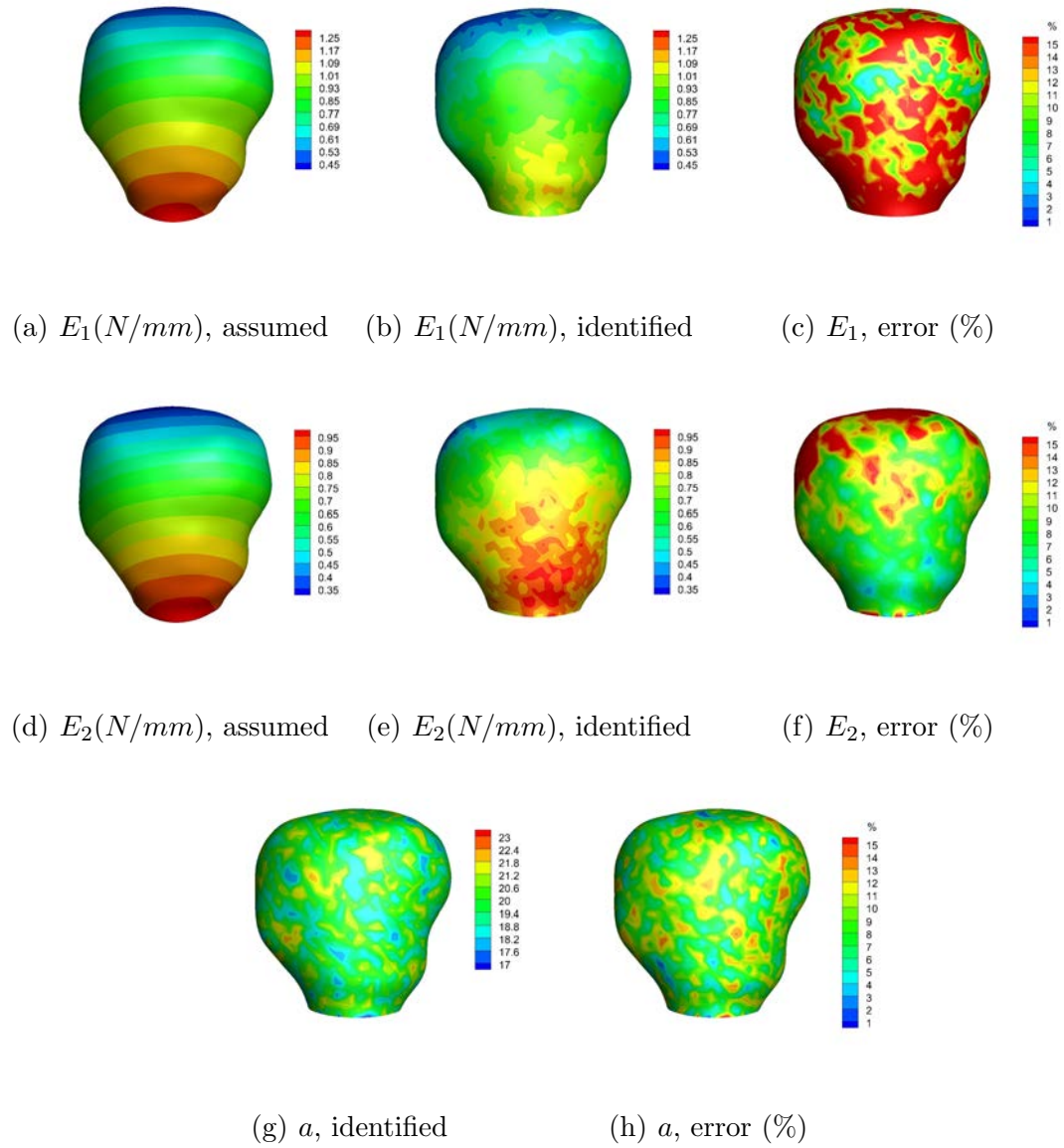


Figure 6.16: Identification result for *CASE II* under 2% of perturbation.

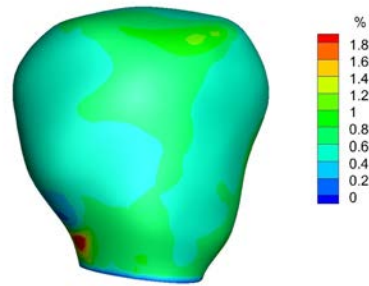


Figure 6.17: Percentage difference in displacement under 1% perturbation.

6.3.3 Predictability of the identified parameters

Since there is a moderately large error in the identified parameters, it is of interest to investigate how the predictability of the parameters is affected. We conduct the forward analysis at 120 mm Hg pressure (not used in regression) with both identified and assumed material parameters. Figure 6.17 and Figure 6.18 show the percentage displacement differences when the perturbation errors are 1% and 2%, respectively. In Figure 6.17, the displacement differences are less than 1% in most regions; the maximum and mean displacement errors are 2.3% and 0.62%, respectively. Clearly, the displacement results are accurate. For 2% perturbation, shown in Figure 6.18, in most regions, the displacement differences are significantly elevated. The maximum and mean displacement errors are 11.29% and 2.09%, respectively. Although the mean error remains reasonably small, the maximum error of more than 10% (in displacement) clearly indicates a significant loss of accuracy in the identification results.

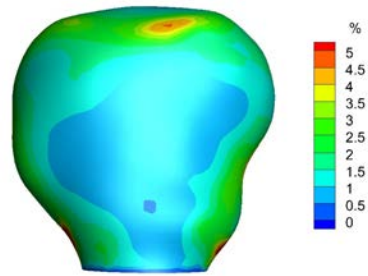


Figure 6.18: Percentage difference in displacement under 2% perturbation.

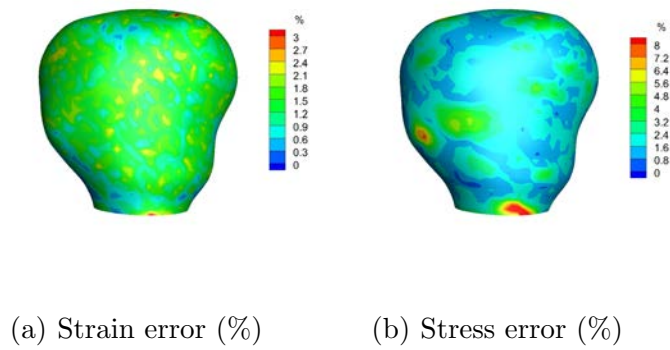


Figure 6.19: Errors in strain and stress data.

To further understand the identification accuracy, for 1% perturbation example, the strain and stress error caused by the noise in displacement data are shown in Figure 6.19. In strain data, the maximum error and mean error is 5.1% and 1.3% respectively. In stress data, the maximum error and mean error is 18.1% and 2.1% respectively.

6.4 Discussion

In this chapter, we use five more representative realistic cerebral aneurysms to study the applicability of PWIM in cerebral aneurysms of realistic geometries. By modeling aneurysms as thin shell structures, the PWIM can now be applied to realistic cerebral aneurysms, without the limitation of convex geometry. For all five cases, the shell PWIM provides good identification results. The four types of material heterogeneities we assumed are all successfully recovered.

Although, there have been researchers studied the characterization of the heterogeneous anisotropic material in the cerebral aneurysm geometries (Kroon et al. [41]). Their method is used on an idealized sphere, not realistic cerebral aneurysm. Balocco et al. [4] present the identification of heterogeneous material properties in realistic cerebral aneurysm. Their studies still focus on the isotropic material, and the material heterogeneity only contains two sets of material parameters. This work is arguably the most complicated of studies of this type. We considered heterogeneous distribution of anisotropic material properties in realistic cerebral aneurysm. The strain/pressure range used in this work is close to physiological values. In addition, there's only 11 states in the regression.

We investigate the predictability of shell PWIM when the fiber direction is unknown. By introducing the fiber direction into constitutive regression, the errors of identification result are elevated. However, even at the elevated error the identified parameters can still predict the forward motion with a high accuracy (less than 1.8%). This indicates the fiber direction can be identified using shell PWIM and

the identification results have the robustness to provide the stable forward analysis results.

Numerical noise is shown to have a significant influence on the identification method. From the identification results under 1% perturbation and 2% perturbation, we can find that the higher the noise level, the lower the accuracy. Nevertheless, the identified parameters at least at 1% perturbation can still yield a reasonable forward analysis results. This is understandable, the displacement calculated through all the material parameters; and different combinations of material parameters can provide the similar stress response, leading to similar displacement results.

Some limitations of the study remain. The first limitation in this study is the assumption on thickness. The uniform thickness we use in this work is an assumption base on the reported values. Although the wall stress resultant is primarily determined by the deformed configuration and corresponding pressure. The wall thickness still affect the computation of the stress couple. If the bending factors in a shell structure are too large, the PWIM may can not be applied. So far, there is no available measurement which can provide the accurate information of the wall thickness. Hopefully with the improvement of imaging technology, we can obtain the real wall thickness and accurately assess the bending stress. Another limitation of this work is the assumption of fiber direction. The material orthotropic and first principal fiber direction are all assumed base on the report [40, 42]. The actual fiber orientation could be more complicated. It should be worth to mention that the assumption of fiber direction does not affect the method. In this work, we have demonstrated that

the identification accuracy will decrease if the fiber direction is assumed as unknown parameter in the constitutive regression. If the fiber structure features can be measured, e.g. [22, 60], the accuracy of the identification results will be improved.

The limitation of this method is that the shell PWIM can only be applied to thin shell structures. So far, we use the broadly cases to evaluate the “thinness”, yet we didn’t provide a criteria for “thinness”.

The ultimate extension of this work is to apply the shell PWIM in the living tissue (e.g. cerebral aneurysms described in this work). The deformed configuration usually will be extracted from medical images during the wall motion. In order to capture the accurate inflated configurations, the advanced medical resolution and registration strategy are higher required.

CHAPTER 7 CONCLUSIONS

7.1 Summary

This thesis is motivated by (1) the demand of identifying the material properties in realistic soft-tissues and (2) the need to extend PWIM to realistic geometries. The shell PWIM developed in this work is shown to be a viable method for at least a family of thin membranes structures, the ones that are sac-like but not necessary convex. We investigate the applicability of shell PWIM with different types of cerebral aneurysms and showed that the method can effectively back out nonlinear heterogeneous properties. The major contributions of this work are as follows.

- Investigated the stress insensitivity to material models in thin shell structures. We have shown that the inverse stress in thin shell structure is, to a large extent, insensitive to material properties (constitutive model and material parameters). This is important for our development, as static determinacy is the premise of PWIM. Surface topologies (open versus closed, number of orifices) and wall thickness have a strong influence on the stress property. It is found that the cerebral aneurysms, which are of saccular geometries, are more suitable to PWIM.
- Developed the finite element formulation of forward and inverse shell methods for 8-fiber Holzapfel material model which is specifically proposed for cerebral aneurysms tissues. This material model is used in aneurysms studies.

- Extended the pointwise identification method to thin shell structures. The shell PWIM resolves the limitation on convex geometry of the original PWIM. The shell PWIM can be utilized to identify the anisotropic material properties in a much broader family of thin soft tissue structures (in this work, the major applications are on cerebral aneurysms). Because of the constitutive regression is conducted pointwisely, the shell PWIM can identify the arbitrary heterogeneous property distributions. In this work, we utilize four types of material heterogeneities, and all of them are accurately recovered. The identification can also include fiber directions and thus, anisotropic properties can be handled without modification to the method.
- Evaluated the applicability of the shell PWIM in six cerebral aneurysm of different surface geometries. The identification errors for the material parameters of all cases stay in an acceptable range (the means of identification errors are less than 6%). The selected aneurysms models all have saddle or concave surface features, and some with relative large daughter aneurysms, forming a good representative group for non-convex aneurysms. This population study indicates that the method can be applied to cerebral aneurysms (assuming, of course, the availability of segmented dynamic image data).
- Investigated numerically the influence of noise. Two ways are used to evaluate the accuracy of identification. One is the identification error; the other one is the predictability of the identified parameters. Although the identification results are sensitive to the noise, the predictability of the model remains to be

resilient.

7.2 Outlook

Although the shell PWIM developed in this work presents significant improvement in characterizing the material properties in the living organs, there are a number of limitations that call for future improvement and development.

- The requirement for high resolution dynamic image data. The method requires high resolution images which could provide accurate information of the dynamic geometry. In fact, for cerebral aneurysms, the required precision exceeds the resolution of current image modalities. There are active image registration studies in tracking the deformation for e.g. lung and heart from medical images [94, 95, 93, 55, 1]. However, the deformation tracking in cerebral aneurysms still faces challenges due to the aneurysms size and the range of deformation. Also, the method by design can predict only lumped stiffness parameters (elasticity parameters times the wall thickness). If the 3D properties are to be determined, the wall thickness is required. Current CT and MRI imaging can not accurately resolve the wall thickness for cerebral aneurysms. Nevertheless, if the wall thickness can be measured from point to point, the intrinsic 3-D stiffness parameters can be easily backed out.
- Another challenge relates to the anisotropic material information in cerebral aneurysm, e.g. the fibers' orientations and fibers' stiffness. In this work, type of the symmetry is assumed, and therefore we need only to characterize the

symmetry axis which requires only one parameter. In reality, the symmetry type needs to be identified from the stress-strain characteristics. Due to the local nature of the regression problem, if we can obtain symmetry information (e.g., fiber orientation) through other means, we can easily incorporate the information into the regression problem to improve the method.

- The last but not the least we need to improve the optimization algorithm. The identification results are influenced by the objective function, initial value and upper/lower boundary. We believe that there are rooms we can work to improve the identification accuracy. For example, we can use more powerful optimization program, or do more improvements on SNOPT to refine the formulation, such as adjusting the objective function, etc. It needs lots practices to set up and run the regression problem.

REFERENCES

- [1] A. A. Amini, Y. Chen, M. Elayyadi, and P. Radeva. Tag surface reconstruction and tracking of myocardial beads from spamm-mri with parametric b-spline surfaces. *IEEE Transactions on Medical Imaging*, 20(2):94–103, 2001.
- [2] Kevin F. Augenstein, Brett R. Cowan, Ian J. LeGrice, Poul M. F. Nielsen, and Alistair A. Young. Method and apparatus for soft tissue material parameter estimation using tissue tagged magnetic resonance imaging. *J. Biomech. Eng*, 127:148, 2005.
- [3] Simone Balocco, Oscar Camara, and Alejandro F. Frangi. Towards regional elastography of intracranial aneurysms. *Medical Image Computing and Computer-Assisted Intervention (2008)*, 11:131–138, 2010.
- [4] Simone Balocco, Oscar Camara, Jose Maria Pozo, Elio Vivas, Teresa Sola, Leopoldo Guimaraens, Hugo A. F. Gratama van Andel, Charles B. Majoje, Bart H. Bijmens, and Alejandro F. Frangi. Feasibility of estimating regional mechanical properties of cerebral aneurysms in vivo. *Medical Physics*, 37(4):1689, 2010.
- [5] P. B. Canham and G. G. Ferguson. A mathematical model for the mechanics of saccular aneurysms. *Neurosurgery*, 17(2):291–5, 1985.
- [6] P. B. Canham, H. M. Finlay, and S. Y. Tong. Stereological analysis of the layered collagen of human intracranial aneurysms. *Journal of Microscopy*, 183:170–180, 1996.
- [7] Penny J. Davies, Fiona J. Carter, and Alfred Cuschieri. Mathematical modelling for keyhole surgery simulations: a biomechanical model for spleen tissue. *IMA J Appl Math*, 67, 2002.
- [8] B J. Doyle, A. Callanan, and T. M. McGloughlin. A comparison of modelling techniques for computing wall stress in abdominal aortic aneurysms. *Biomed Eng Online*, 6:38, 2007.
- [9] Ahmet Erdemir, Meredith L. Viveiros, Jan S. Ulbrecht, and Peter R. Cavanagh. An inversefinite-element model of heel-pad indentation.
- [10] J. L. Ericksen and C. Truesdell. Exact theory of stress and strain in rods and shells. *Archive for Rational Mechanics and Analysis*, 1:295–323, 1958.

- [11] Mehdi Farshada, Michel Barbezata, Peter Floelera, Franz Schmidlinb, Pierre Graberb, and Peter Niederer. Material characterization of the pig kidney in relation with the biomechanical analysis of renal trauma. *Journal of Biomechanics*, 32:417425, 1999.
- [12] M. F. Fillinger, S. P. Marra, M. L. Raghavan, and F. E. Kennedy. Prediction of rupture risk in abdominal aortic aneurysm during observation: Wall stress versus diameter. *Journal of Vascular Surgery*, 37:724–732, 2003.
- [13] M. F. Fillinger, M. L. Raghavan, S. P. Marra, J. L. Cronenwett, and F. E. Kennedy. *in vivo* analysis of mechanical wall stress and abdominal aortic aneurysm rupture risk. *Journal of Vascular Surgery*, 36:589–597, 2002.
- [14] H. O. Foster. Very large deformations of axially symmetrical membranes made of neo-Hookean materials. *International Journal of Engineering Science*, 5:95–117, 1967.
- [15] Y. C. Fung. *Biomechanics: Motion, Flow, Stress and Growth*. Springer-Verlag, New York, 1990.
- [16] Y. C. Fung. *Biomechanics: Mechanical Properties of living Tissues*. Springer, Berlin, 1993.
- [17] P. E. Gill, W. Murray, and M. A. Saunders. SNOPT: An SQP algorithm for large-scale constrained optimization. *SIAM Review*, 47:99–131, 2005.
- [18] S. Govindjee and P. A. Mihalic. Computational methods for inverse finite elastostatics. *Computer Methods in Applied Mechanics and Engineering*, 136:47–57, 1996.
- [19] S. Govindjee and P. A. Mihalic. Computational methods for inverse deformations in quasi-incompressible finite elasticity. *International Journal for Numerical Methods in Engineering*, 43:821–838, 1998.
- [20] A. E. Green and J. E. Adkins. *Large Elastic Deformations*. Clarendon Press, Oxford, 2nd edition, 1970.
- [21] G. J. Hademenos, T. Massoud, D. J. Valentino, G. Duckwiler, and F. Viuela. A nonlinear mathematical model for the development and rupture of intracranial saccular aneurysms. *Neurol Res.*, 16(5):376–84, 1994.
- [22] M. C. Jimenez Hamann, M. S. Sacks, and T. I. Malinin. Quantification of the collagen fibre architecture of human cranial dura mater. *Journal of Anatomy*, 192:99–106, 1998.

- [23] G. A. Holzapfel, T. C. Gasser, and R. W. Ogden. Comparison of a multi-layer structural model for arterial walls with a fung-type model, and issues of material stability. *Journal of Biomechanical Engineering-Transactions of the ASME*, 126:264–275, 2004.
- [24] G. A. Holzapfel and T. G. Gasser. A viscoelastic model for fiber-reinforced composites at finite strains: Continuum basis, computational aspects and applications. *Computer Methods in Applied Mechanics and Engineering*, 190(34):4379–4403, 2001.
- [25] G. A. Holzapfel, T. G. Gasser, and R. W. Ogden. A new constitutive framework for arterial wall mechanics and a comparative study of material models. *Journal of Elasticity*, 61:1–48, 2000.
- [26] F. P. K. Hsu, A. C. M. Liu, J. Downs, D. Rigamonti, and J. D. Humphrey. A triplane video-based experimental system for studying axisymmetrically inflated biomembranes.
- [27] F. P. K. Hsu, A. C. M. Liu, J. Downs, D. Rigamonti, and J. D. Humphrey. A triplane video-based experimental system for studying axisymmetrically inflated biomembranes. *IEEE Transactions on Biomedical Engineering*, 42:442–450, 1995.
- [28] F. P. K. Hsu, C. Schwab, D. Rigamonti, and J. D. Humphrey. Identification of response functions from axisymmetrical membrane inflation tests - implications for biomechanics. *International Journal of Solids and Structures*, 31:3375–3386, 1994.
- [29] Tie Hu and Jaydev P. Desai. A biomechanical model of the liver for reality-based haptic feedback. In *MICCAI (1)*, pages 75–82, 2003.
- [30] Tie Hu and Jaydev P. Desai. Characterization of soft-tissue material properties: Large deformation analysis. In *ISMS*, pages 28–37, 2004.
- [31] Tie Hu and Jaydev P. Desai. Soft-tissue material properties under large deformation: Strain rate effect. *Proceedings of the 26th Annual International Conference of the IEEE EMBS, San Francisco, CA, USA*, pages 2758–2761, 2004.
- [32] J. D. Humphrey. Intracranial saccular aneurysms. In *Biomechanics of Soft Tissue in Cardiovascular Systems*, CISM Courses and Lectures No. 441 (Udine, Italy), pages 185–220. Springer, New York, 2003.

- [33] J. D. Humphrey and P. B. Canham. Structure, mechanical properties, and mechanics of intracranial saccular aneurysms. *Journal of Elasticity*, 61:49–81, 2000.
- [34] R. H. Iding, K. S. Pister, and R. L. Taylor. Identification of nonlinear elastic solids by a finite element method. *Computer Methods in Applied Mechanics and Engineering*, 4:121–142, 1974.
- [35] F. G. Hoppin Jr, G. C. Lee, and S. V. Dawson. Properties of lung parenchyma in distortion. *Journal of Applied Physiology*, 39:742–751, 1975.
- [36] M. Kauer, V. Vuskovic, J. Dual, G. Szekelyc, and M. Bajka. Inversefiniteelementcharacterization of softtissues. *Medical Image Analysis*, 6(3):275287, 2002.
- [37] K. T. Kavanagh and R. W. Clough. Finite element applications in the characterization of elastic solids. *International Journal of Solids and Structures*, 7:11–23, 1971.
- [38] Jung Kim and Mandayam A. Srinivasan. Characterization of viscoelastic soft tissue properties from in vivo animal experiments and inverse fe parameter estimation. *Medical Image Computing and Computer-Assisted Intervention MICCAI 2005*, 3750/2005:599–606, 2005.
- [39] M. Koishi and S. Govindjee. Inverse design methodology of a tire. *Tire Science and Technology*, 29:155–170, 2001.
- [40] M. Kroon and G. A. Holzapfel. A model for saccular cerebral aneurysm growth by collagen fibre remodelling. *Journal of Theoretical Biology*, 247:775–787, 2007.
- [41] M. Kroon and G. A. Holzapfel. Estimation of the distribution of anisotropic, elastic properties and wall stresses of saccular cerebral aneurysms by inverse analysis. *Proceedings of the Royal Society of London, Series A*, 464:807–825, 2008.
- [42] M. Kroon and G. A. Holzapfel. A new constitutive model for multi-layered collagenous tissues. *Journal of Biomechanics*, 41:2766–2771, 2008.
- [43] S. K. Kyriacou, A. D. Shah, and J. D. Humphrey. Inverse finite element characterization of nonlinear hyperelastic membranes. *Journal of Applied Mechanics-Transactions of the ASME*, 64:257–262, 1997.
- [44] Y. Lanir and Y. C. Fung. Two-dimensional mechanical properties of rabbit skin. I. experimental system. *Journal of Biomechanics*, 7:29–34, 1974.

- [45] Y. Lanir and Y. C. Fung. Two-dimensional mechanical properties of rabbit skin. II. experimental results. *Journal of Biomechanics*, 7:171–182, 1974.
- [46] Yi Liu, Amy E. Kerdok, and Robert D. Howe. A nonlinear finite element model of soft tissue indentation. *Medical Simulation*, 20(3078/2004):67–76, 2004.
- [47] J. Lu and X. Zhao. Pointwise identification of elastic properties in nonlinear hyperelastic membranes. part i: Theoretical and computational developments. *Journal of Applied Mechanics*, 76:061013/1–061013/10, 2009.
- [48] J. Lu, X. Zhou, and M. L. Raghavan. Computational method of inverse elastostatics for anisotropic hyperelastic solids. *International Journal for Numerical Methods in Engineering*, 69:1239–1261, 2007.
- [49] J. Lu, X. Zhou, and M. L. Raghavan. Inverse method of stress analysis for cerebral aneurysms. *Biomechanics and Modeling in Mechanobiology*, 7:477–486, 2008.
- [50] J. Lu, X.L. Zhou, and M.L. Raghavan. Inverse elastostatic stress analysis in pre-deformed biological structures: Demonstration using abdominal aortic aneurysms. *Journal of Biomechanics*, 40(3):693–696, 2007.
- [51] B. Ma, J. Lu, R. E. Harbaugh, and M. L. Raghavan. Nonlinear anisotropic stress analysis of anatomically realistic cerebral aneurysms. *ASME Journal of Biomedical Engineering*, 129:88–99, 2007.
- [52] Raghavan ML and Vorp DA. Toward a biomechanical tool to evaluate rupture potential of abdominal aortic aneurysm: identification of a finite strain constitutive model and evaluation of its applicability. *J Biomech*, 33(4):475–82, 2000.
- [53] P. M. Naghdi. The theory of plates and shells. In C. Truesdell, editor, *Handbuch der Physik*, volume VIa/2, pages 425–640. Springer-Verlag, Berlin, New York, 1972.
- [54] M. A. Nicosia, J. S. Kasalko, R. P. Cochran, D. R. Einstein, and K. S. Kunzelman. Biaxial mechanical properties of porcine ascending aortic wall tissue. *Journal of Heart Valve Disease*, 11(5):680–686, 2002.
- [55] N. F. Osman, E. R. McVeigh, and J. L. Prince. Imaging heart motion using harmonic phase mri. *Transactions on Medical Imaging*, 19.

- [56] M. L. Raghavan, D. A. Vorp, M. P. Federle, M. S. Makaroun, and M. W. Webster. Wall stress distribution on three-dimensionally reconstructed models of human abdominal aortic aneurysm. *Journal of Vascular Surgery*, 31:760–769, 2000.
- [57] J. F. Rodriguez, Giampaolo Martufi, Manuel Doblare, and Ender A. Finol. The effect of material model formulation in the stress analysis of abdominal aortic aneurysms. *Ann Biomed Eng*, 37(11):2218, 2009.
- [58] J. F. Rodriguez, C. Ruiz, and M. Doblare and G. A. Holzapfel. Mechanical stresses in abdominal aortic aneurysms: influence of diameter, asymmetry, and material anisotropy. *J Biomech Eng*, 130(2):021023, 2008.
- [59] M. S. Sacks. Biaxial mechanical evaluation of planar biological materials. *Journal of Elasticity*, 61:199–246, 2000.
- [60] M. S. Sacks, D. B. Simith, and E. E. Hiester. A small angle light scattering device for planar connective tissue microstructural analysis. *Ann Biomed Eng.*, 25(4):678–89, 1997.
- [61] N. Sakalihasan, R. Limet, and O. D. Defawe. Abdominal aortic aneurysm. *Lancet*, 365(9470):1577–89, 2005.
- [62] Evren Samur, Mert Sedef, Cagatay Basdogan, Levent Avtan, and Oktay Duzgunc. A robotic indenter for minimally invasive measurement and characterization of soft tissue response. *Medical Image Analysis*, 11(4):361373, 2007.
- [63] L. R. Schmidt and J. F. Carley. Biaxial stretching of heat-softened plastic sheets using an inflation technique. *International Journal of Engineering Science*, 13:563–578, 1975.
- [64] A. Scott, G. G. Ferguson, and M. R. Roach. Comparison of the elastic properties of human intracranial arteries and aneurysms. *Canadian Journal of Physiology and Pharmacology*, 50:328–332, 1972.
- [65] P. Seshaiyer, F. P. K. Hsu, A. D. Shah, S. K. Kyriacou, and J. D. Humphrey. Multiaxial mechanical behavior of human saccular aneurysms. *Computer methods in biomedical engineering*, 4:281–289, 2001.
- [66] P. Seshaiyer and J. D. Humphrey. A sub-domain inverse finite element characterization of hyperelastic membranes including soft tissues. *Journal of Biomechanical Engineering-Transactions of the ASME*, 125:363–371, 2003.

- [67] F. A. Lederle and D. L. Simel. Does this patient have abdominal aortic aneurysm? *Jama-Journal of the American Medical Association*, 281(1):77–82, 1999.
- [68] J. C. Simo. On a stress resultant geometrically exact shell-model .7. shell intersections with 5/6-dof finite-element formulations. *Computer Methods in Applied Mechanics and Engineering*, 108(3-4):319–339, 1993.
- [69] J. C. Simo and D. D. Fox. On a stress resultant geometrically exact shell-model .1. formulation and optimal parametrization. *Computer Methods in Applied Mechanics and Engineering*, 72(3):267–304, 1989.
- [70] J. C. Simo, D. D. Fox, and M. S. Rifai. On a stress resultant geometrically exact shell-model .3. computational aspects of the nonlinear-theory. *Computer Methods in Applied Mechanics and Engineering*, 79(1):21–70, 1990.
- [71] J. C. Simo, D. D. Fox, and M. S. Rifai. On a stress resultant geometrically exact shell-model .4. variable thickness shells with through-the-thickness stretching. *Computer Methods in Applied Mechanics and Engineering*, 81(1):91–126, 1990.
- [72] J. C. Simo and J. G. Kennedy. On a stress resultant geometrically exact shell-model .5. nonlinear plasticity - formulation and integration algorithms. *Computer Methods in Applied Mechanics and Engineering*, 96(2):133–171, 1992.
- [73] J. C. Simo, M. S. Rifai, and D. D. Fox. On a stress resultant geometrically exact shell-model .6. conserving algorithms for nonlinear dynamics. *International Journal for Numerical Methods in Engineering*, 34(1):117–164, 1992.
- [74] H. J. Steiger, R. Aaslid, S. Keller, and H. J. Reulen. Strength, elasticity and viscoelastic properties of cerebral aneurysms. *Heart Vessels*, 5:41–46, 1989.
- [75] W. Sun, M. S. Sacks, and M. J. Scott. Effects of boundary conditions on the estimation of the planar biaxial mechanical properties of soft tissues. *ASME Journal of Biomechanical Engineering*, 127:709–715, 2005.
- [76] Boon K. Tay, Jung Kim, and Mandayam A. Srinivasan. In vivo mechanical behavior of intra-abdominal organs. *IEEE TRANSACTIONS ON BIOMEDICAL ENGINEERING*, 53:321–329, 2006.
- [77] Mano J. Thubrikar, Jihad Al-Soudi, and Francis Robicsek. Wall stress studies of abdominal aortic aneurysm in a clinical model. *Journal of Vascular Surgery*, 15:355–366, 2001.

- [78] M. Tóth, G. L. Nádasy, I. Nyáry, T. Kerényi, M. Orosz, G. Molnárka, and E. Monos. Sterically inhomogeneous viscoelastic behavior of human saccular cerebral aneurysms. *Journal Vascular Research*, 35:345–355, 1998.
- [79] L. R. G. Treloar. Strains in an inflated rubber sheet, and the mechanism of bursting. *Institution of the Rubber Industry Transactions*, 19:201–212, 1944.
- [80] L. R. G. Treloar. Stress-strain data for vulcanized rubber under various types of deformation. *Transactions of the Faraday Society*, 40:59–70, 1944.
- [81] L. R. G. Treloar. *The Physics of Rubber Elasticity*. Oxford University Press, New York, 2nd edition, 1958.
- [82] M. Truijers, J. A. Pol, L. J. Schultzekool, S. M. van Sterkenburg, M. F. Fillingier, and J. D. Blankensteijn. Wall stress analysis in small asymptomatic, symptomatic and ruptured abdominal aortic aneurysms. *Eur J Vasc Endovasc Surg*, 33(4):401–7, 2007.
- [83] A. C. Ugural and Saul K. Fenster. *Advanced strength and applied elasticity*. Prentice Hall, New Jersey, 2003.
- [84] G. R. Upchurch and T. A. Schaub. Abdominal aortic aneurysm. *American Family Physician*, 73(7):1198–1204, 2006.
- [85] J. P. Vande Geest, D. E. Schmidt, M. S. Sacks, and D. A. Vorp. The effects of anisotropy on the stress analyses of patient-specific abdominal aortic aneurysms. *Annals of Biomedical Engineering*, 36(6):921–932, 2008.
- [86] H. Vaughan. Pressurizing a prestretched membrane to form a paraboloid. *International Journal of Engineering Science*, 18:99–107, 1980.
- [87] D. A. Vorp. Biomechanics of abdominal aortic aneurysm. *Journal of Biomechanics*, 40(9):1887–1902, 2007.
- [88] D. A. Vorp and J. P. Vande Geest. Biomechanical determinants of abdominal aortic aneurysm rupture. *Arteriosclerosis Thrombosis and Vascular Biology*, 25(8):1558–1566, 2005.
- [89] A. Wineman, D. Wilson, and J. W. Melvin. Material identification of soft tissue using membrane inflation. *Journal of Biomechanics*, 12:841–850, 1979.
- [90] T. Yamada. Finite element procedure of initial shape determination for rubber-like materials. Technical Report No. 20, Res. Lab. Eng. Mat. Tokyo Inst. Tech., 1995.

- [91] T. Yamada. Finite element procedure of initial shape determination for hyperelasticity. *Structural Engineering and Mechanics*, 6(2):173–183, 1998.
- [92] W. H. Yang and W. W. Feng. On axisymmetrical deformations of nonlinear membranes. *ASME Journal of Applied Mechanics*, 37:1002–1011, 1970.
- [93] Youbin Yin. *MDCT-BASED DYNAMIC, SUBJECT-SPECIFIC LUNG MODELS VIA IMAGE REGISTRATION FOR CFD-BASED INTERROGATION OF REGIONAL LUNG FUNCTION*. PhD thesis, University of Iowa, Iowa City, IA 52242, 2011.
- [94] Youbing Yin, Eric A Hoffman, Kai Ding, Joseph M Reinhardt, and Ching-Long Lin. Lung lobar slippage assessed with the aid of image registration. *Medical Image Computing and Computer-Assisted Intervention MICCAI 2010. Vol. 6362 of Lecture Notes in Computer Science*, pages 578–585. Springer Berlin / Heidelberg, Beijing, China, 2010.
- [95] Youbing Yin, Eric A Hoffman, Kai Ding, Joseph M Reinhardt, and Ching-Long Lin. A cubic b-spline-based hybrid registration of lung ct images for a dynamic airway geometric model with large deformation. *PHYSICS IN MEDICINE AND BIOLOGY*, 56:2032–18, 2011.
- [96] X. Zhao, X. Chen, and J. Lu. Pointwise identification of elastic properties in nonlinear hyperelastic membranes. part ii: Experimental validation. *Journal of Applied Mechanics*, 76:061014/1–061014/8, 2009.
- [97] X. Zhao, M. L. Raghavan, and J. Lu. Characterizing heterogeneous properties of cerebral aneurysms with unknown stress-free geometry: a precursor to in vivo identification. *Journal of Biomechanical Engineering*, 133 (5):051008, 2011.
- [98] X. Zhao, M. L. Raghavan, and J. Lu. Identifying the distributive heterogeneous anisotropic elastic properties in cerebral aneurysms: A pointwise approach. 10:177–189, 2011.
- [99] Xuefeng Zhao. *Pointwise identification of elastic properties in nonlinear heterogeneous membranes, and application to soft tissues*. PhD thesis, University of Iowa, Iowa City, IA 52242, 2009.
- [100] X. Zhou. *Inverse elastostatic stress analysis for biological structures*. PhD thesis, University of Iowa, Iowa City, IA 52242, 2007.
- [101] X. Zhou and J. Lu. Inverse formulation for geometrically exact stress resultant shells. *International Journal for Numerical Methods in Engineering*, 74:1278–1302, 2008.

- [102] Xianlian Zhou, Madhavan L. Raghavan, Robert E. Harbaugh, and Jia Lu. Patient-specific wall stress analysis in cerebral aneurysms using inverse shell model. *Annals of Biomedical Engineering*, 38:478–489, 2010.